People's Democratic Republic of Algeria

Ministry of Higher Education and Scientific Research

FERHAT ABBAS UNIVERSITY - SETIF1

FACULTY OF SCIENCES

DEPARTEMENT OF PHYSICS

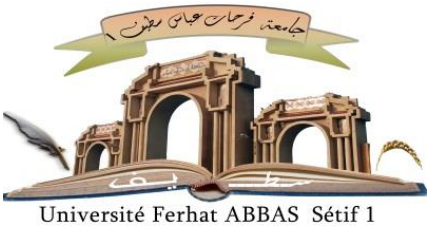

THESIS

For the degree of Doctor 3rd cycle LMD

Field: Physics and Subatomic Physics Engineering

BY

BOUSSAHOUL Fares

TOPIC

Optimization of Irradiation and Measurement Parameters for Analyzing Depth Profiles of Trace Heavy Elements in Silicon Using RBS Technique

Defended on 17 /10/2024 in front of the Jury:

Naima Amrani	**Professor**	**Univ. Ferhat Abbas Setif 1**	**President**
Djamel Maouche	**Professor**	**Univ. Ferhat Abbas Setif 1**	**Thesis director**
Wassila Boukhenfouf	**Associate Professor**	**Univ. Ferhat Abbas Setif 1**	**Examiner**
Nabil Ounoughi	**Professor**	**University of Jijel**	**Examiner**
Salah-Eddine Bentridi	**Associate Professor**	**University of Khemis Miliana**	**Examiner**

Abstract

The thesis work presents a new concept that integrates heavy ion Rutherford Backscattering Spectrometry with microbeam technology combined with high detection solid angle for the measurement of the depth profile and areal distribution of heavy elements in silicon using a Si microbeam. The concept revolves around using a probing beam equal or heavier than the major substrate's elements, aiming not only to increase the backscattering cross-section, similar to well established heavy element Rutherford Backscattering Spectrometry, but also to eliminate pile-up due to backscattering from substrate, which is essential for sensitive analysis. This allows a significant increase in microbeam currents without increasing the count rate in large area detectors. The choice and characteristics of the probing beam are important for ensuring precise and reliable measurements. Various aspects of the probing beam, such as brightness, spatial resolution, and beam halo, were thoroughly investigated to enhance result accuracy and precision.

A detection system with a total detection solid angle of approximately 1 sr was utilized in an unconventional geometry, where backscattering ions enter the detector at different angles resulting in longer distances in the passivation layer of the detectors. An examination into the effect of entrance angle on detector resolution was conducted, and a spectral analysis model was developed to address kinematic spread issues resulting from large detection solid angles based on Au reference thin films.

Focussed 2.4 MeV Si^{2+} ions were scanned over the frontal or lateral surface of silicon wafers to measure both the areal concentrations and depth profiles of all elements heavier than silicon. Tests were done on samples with Platinum concentration range of $4 \times 10\ 12^{-2} \times 10^{14}$ at/cm^3 that was diffused via the Platinum Silicide surface layer process from one lateral surface into the 400 µm thick Si wafers. An appropriate microbeam collimator was used to shield the detectors from events caused by forward scattering and scattering of the Si ion beam halo from different components in the reaction chamber. Lateral scans of the silicon wafer were performed by focussed Si ions, with ~10 µm spot size and of the nA range beam currents. The Rutherford Backscattering Spectrometry intensity maps containing the platinum depth profile were obtained with a sensitivity of 6.7×10^9 at/cm^2.

Résumé

Ce travail de thèse présente un nouveau concept qui intègre la spectrométrie de rétrodiffusion de Rutherford des ions lourds avec la technologie du microfaisceau, combinée avec un grand angle solide de détection pour la mesure du profil de profondeur et de la distribution surfacique des éléments lourds dans le silicium en utilisant un microfaisceau de silicium. Le concept repose sur l'utilisation d'un faisceau de sondage plus lourd que les principaux éléments du substrat, visant non seulement à augmenter la section efficace de rétrodiffusion, similaire à la spectrométrie de rétrodiffusion de Rutherford bien établie pour les éléments lourds, mais aussi à éliminer l'accumulation due à la rétrodiffusion du substrat, ce qui est essentiel pour une analyse sensible. Cela permet une augmentation significative des courants de microfaisceau sans augmenter le taux de comptage dans les détecteurs de grande surface. Le choix et les caractéristiques du faisceau de sondage sont importants pour garantir des mesures précises et fiables. Divers aspects du faisceau de sondage, tels que la luminosité, la résolution spatiale et le halo du faisceau, ont été minutieusement étudiés pour améliorer la précision et la fiabilité des résultats.

Un système de détection avec un angle solide de détection total d'environ 1 sr a été utilisé dans une géométrie non conventionnelle, où les ions rétrodiffusés entrent dans le détecteur à différents angles, résultant en des distances plus longues dans la couche de passivation des détecteurs. Un examen de l'effet de l'angle d'entrée sur la résolution du détecteur a été effectué, et un modèle d'analyse spectrale a été développé pour traiter les problèmes de répartition cinématique résultant de grands angles de détection.

Des ions de silicium Si^{2+} focalisés d'une énergie de 2,4 MeV ont été balayés sur la surface frontale ou latérale des tranches de silicium pour mesurer à la fois les concentrations surfaciques et les profils de profondeur de tous les éléments plus lourds que le silicium. Des tests ont été effectués sur des échantillons avec une concentration de platine allant de 4×10^{12} à 2×10^{14} at/cm^3. Un collimateur de microfaisceau approprié a été utilisé pour protéger les détecteurs des événements causés par la diffusion avant et la diffusion du halo du faisceau d'ions de silicium provenant de différents composants dans la chambre de réaction. Des balayages latéraux de la tranche de silicium ont été réalisés par des ions de silicium focalisés, avec une taille de spot d'environ 10 μm et des courants de faisceau de l'ordre du nanoampère. Les cartes d'intensité contenant le profil de profondeur du platine ont été obtenues avec une sensibilité de $6,7 \times 10^9$ atomes/cm^2.

الملخص

تقدم هذه الأطروحة مفهومًا جديدًا يدمج بين تقنية طيف تشتت رذرفورد للأيونات الثقيلة وتكنولوجيا الشعاع الميكروي، مع زاوية كشف صلبة كبيرة لقياس توزيع العمق والمساحة للعناصر الثقيلة في السيليكون باستخدام شعاع ميكروي من السيليكون. يتمحور هذا المفهوم حول استخدام شعاع اختبار أثقل من العناصر الأساسية في الركيزة، بهدف زيادة مقطع التشتت الخلفي، كما هو الحال في طيف تشتت رذرفورد للعناصر الثقيلة، وكذلك للقضاء على تراكم التشتت الخلفي من الركيزة، مما يعزز التحليل الحساس. هذا يسمح بزيادة كبيرة في تيارات الشعاع الميكروي دون زيادة معدل العد في كاشفات المساحة الكبيرة. اختيار وخصائص شعاع الاختبار حاسمة لضمان قياسات دقيقة وموثوقة. تم دراسة مختلف جوانب شعاع الاختبار، مثل السطوع والدقة المكانية والهالة الشعاعية، بدقة لتعزيز دقة وموثوقية النتائج.

استخدم نظام كشف بزاوية كشف صلبة إجمالية تقارب 1 ستراديان في هندسة غير تقليدية، حيث تدخل الأيونات المتشتتة إلى الكاشف بزوايا مختلفة مما يؤدي إلى مسافات أطول في طبقة التخميل للكاشفات. تم فحص تأثير زاوية الدخول على دقة الكاشف، وتم تطوير نموذج تحليل طيفي لمعالجة مشاكل انتشار الحركة الناتجة عن الزوايا الكبيرة للكشف.

تم مسح أيونات السيليكون بطاقة 2.4 ميغا إلكترون فولت فوق السطح الأمامي أو الجانبي لرقائق السيليكون لقياس كل من تركيزات المساحة وملامح العمق لجميع العناصر الأثقل من السيليكون. أجريت اختبارات على عينات بتركيز بلاتين يتراوح بين 4×10^{12} إلى 2×10^{14} ذرة/سم^3. تم استخدام محدد شعاع ميكروي مناسب لحماية الكاشفات من الأحداث الناتجة عن التشتت الأمامي وتشتت هالة شعاع السيليكون من مكونات مختلفة في غرفة التفاعل. أجريت مسوحات جانبية لرقاقة السيليكون بواسطة أيونات السيليكون المركزة، بحجم بقعة حوالي 10 ميكرون وتيارات شعاع في نطاق النانو أمبير. تم الحصول على خرائط شدة طيف تشتت رذرفورد التي تحتوي على ملامح عمق البلاتين بحساسية تبلغ 6.7×10^9 ذرة/سم^2.

Acknowledgement

The completion of this thesis would not have been possible without the invaluable support and encouragement I received from so many individuals, to whom I am deeply grateful. It has been a collaborative effort of both personal and professional relationships that have contributed significantly to the success of my research. I would like to express my heartfelt appreciation to everyone who has directly or indirectly played a role in this journey.

First and foremost, I extend my deepest gratitude to God for guiding me and granting me the strength and perseverance to bring this work to fruition.

I would like to sincerely thank Professor **Djamel Maouche**, my thesis supervisor, for his trust in me and his guidance throughout this journey. His unwavering support, insightful advice, and availability were instrumental in shaping this research.

A special thanks to Pr. **Milko Jaksic**, my scientific director at the Experimental Physics Laboratory, Ruder Boskovic Institute, Croatia. His motivation, constant presence, and kindness during the many experiments were key to the success of this work. I am deeply grateful for his mentorship.

I also extend my sincere thanks to Dr. **Georgios Provatas** for his invaluable assistance and keen interest in solving the technical challenges of the experimental phase. His dedication and the many hours spent working through these issues were truly appreciated.

My profound gratitude goes to Dr. **Gouasmia Sabrina**, my wife and colleague, for her endless support, encouragement, and belief in me. Her shared experience and knowledge made this journey not only manageable but more enriching.

I would also like to express my thanks to Professor **Ettore Vittone** from Università degli Studi di Torino, Italy, for his generosity in providing the samples and related data necessary for this research.

I am immensely grateful to my colleagues **Andro Kovaćić**, **Damir Špania**, **Zvonko Kolar**, **Želko Periča**, and **Donny Cosic** for their collaboration and assistance during the experimental work. Their support and friendship have been invaluable.

I am deeply honored to express my gratitude to the esteemed members of my thesis jury:

- **Naima Amrani**, Professor at Univ. Ferhat Abbas Setif 1, for graciously serving as president of the jury and for the time and effort invested in reviewing my work. I deeply appreciate your interest and valuable feedback.
- **Wassila Boukhenfouf**, Associate Professor at Univ. Ferhat Abbas Setif 1, for accepting the role of examiner and for the honor of participating in the jury. Your insights and critique have greatly enhanced this thesis.
- **Nabil Ounoughi**, Professor at University of Jijel, for your role as an examiner and for your thoughtful engagement with my research.
- **Salah-Eddine Bentridi**, Associate Professor at University of Khemis Miliana, for serving as an examiner and for your time and dedication to reviewing this work.

A special, heartfelt thank you goes to my dear father, **Messoud Boussahoul**, "rabi yarahmou." I wish you were here to witness this milestone. Your memory continues to inspire me. To my wonderful mother, **Hadda Benchaaban**, your love, sacrifices, and unwavering belief in me have been the foundation of my success. I am eternally grateful for everything you've done.

Lastly, I wish to thank my siblings: **Djamel, Karim, Monir, Mourad, Abd el Halim, Souria, Rahima, Souad, Firouz, and Samra**. Your presence, encouragement, and love have been a constant source of strength throughout this journey.

Contents

Part 2: Ion Beam Analysis

Chapter 3: Measurement of Pt Depth Profile with very Low Concentration in Silicon

List of figures

Figure.3.26: Representative map of Pt distribution by lateral scan on Si wafer thickness

Figure.3.27: The depth profile of Pt in Silicon defined by RBS technique for 810 °C and 850°C annealing temperatures compared to simulated profile at 830°C by A. Johnsson et all.

General Introduction

Silicon is a widely used material in the semiconductor industry due to its unique electrical properties. Implanting trace elements (dopants) significantly affects silicon device performance, so accurate measurement of dopant levels is fondamental. Common techniques for this include Secondary Ion Mass Spectrometry (SIMS) and total reflection X-ray fluorescence (TR-XRF). Electrical methods like Deep Level Transient Spectroscopy (DLTS), electrochemical Capacitance-Voltage profiling (eCV), and Spreading Resistance Profiling (SRP) also provide valuable insights but face challenges in calibration and sample preparation, achieving about 30% accuracy. Ion beam analysis techniques such as Particle Induced X-ray Emission (PIXE), Proton Induced Gamma-ray Emission (PIGE), Elastic Recoil Detection Analysis (ERDA), and Rutherford Backscattering Spectrometry (RBS) offer high sensitivity and excellent depth profiling capabilities. However, these methods often struggle with detecting dopant concentrations below 10^{14} at/cm^2.

Voltage-link converters are very important components in modern drive systems for controlling inductive loads like electric motors. These converters use components such as insulated gate bipolar transistors (IGBTs), fast-switching MOS devices, and controlled bipolar power transistors with blocking capacities from 400 V to over 6500 V tailored for specific applications. IGBTs achieve the desired output frequency by synchronously switching on and off in a bridge circuit, often using pulse-width modulation for optimal efficiency. Platinum is used to enhance the electrical characteristics of silicon power devices like silicon power diodes, which are essential for high-power and high-frequency switching of inductive loads.

Rutherford backscattering spectrometry (RBS) is one of the most well-studied techniques for material characterization, as it provides almost 1% absolute uncertainty in the analysis of thin films without the use of sample-matched standards. Furthermore, it is a non-destructive and model-free method. The sensitivity of the technique, although depending on the matrix of the sample under study, can be very good for heavy elements of the order of 10^{14} at/cm^2 in routine analysis. By appropriate selection of ion beam particle and its energy, enhancements in the cross-section can further increase the sensitivity. By combining it with a high detection solid angle, the detection limits that RBS can achieve could be as low as 10^{10} at/cm^2.

Depending on the application, the number of counts in the RBS detector can be increased by extending the acquisition time, increasing the ion beam current, decreasing the primary energy, decreasing the scattering angle, or using a large detection solid angle. However, each of these

approaches has some disadvantages as well. Increasing the acquisition time results in higher analysis costs, while increasing the beam current is constrained by technical limitations of electronics as well as possible radiation damage. On the other hand, decreasing the beam energy and scattering angle can sacrifice energy and depth resolution.

Heavy beam RBS is one of the solutions that utilize enhanced backscattering cross-section. The technique of heavy ion RBS has been the subject of investigation in numerous research papers. However, the full potential of this technique when applied using a microbeam has not yet been adequately explored. To improve the analysis of low concentrations, it may be possible to increase the solid angle, as this results in a corresponding increase in detection absolute efficiency. Pile-up is a major issue in trace element analysis in conventional RBS analysis using He ions. In order to measure a single atom of platinum among one billion atoms of silicon, the spectrum must be devoid of noise. However, lowering the beam current results in a prolonged measurement time.

In this work, we are optimizing the RBS detection system for the analysis of single heavy elements (Pt) in silicon with a strong focus on simplicity and ease of implementation. The depth profile of Pt in Si is influenced by both the way Pt implantation has been performed and the thermal treatment approach applied. The goal of this work is to determine the depth profile of Pt implanted in silicon through Pt diffusion from the Pt-Silicide surface layer. Classical analytical depth profiling RBS alone cannot obtain the depth profile by simply irradiating the front surface due to the low penetration of heavy ions (a few micrometres). Therefore, we employed a new setup using a microbeam to laterally scan the Si wafer of several hundreds of micrometres in thickness. In this approach, the heavy ion microbeam can provide positional resolution at the micrometre scale. While the detection limits of the routine RBS setup in our laboratory based on He ions are about 10^{15} at/cm², the aim of this work is to enhance the detection limit significantly down to approximately 10^{9} at/cm², which would enable the measurement of platinum concentration in low-doped silicon that may have a concentration even below 10^{11} at/cm².

The thesis manuscript is divided into four chapters. The first chapter provides an overview of silicon-based semiconductors, emphasizing the significance and role of platinum in high-power devices. Various methods for introducing platinum are discussed, highlighting the most effective techniques, and sample preparation steps are presented at the chapter's conclusion.

The second chapter consists of two parts. The first part examines the physical processes involved when energetic ions traverse solid matter. It begins with an overview of the interaction between charged particles and matter, reviewing the main concepts of binary collision. Equations for modeling interaction parameters are derived within this framework. The chapter introduces the concept of scattering from target nuclei and explains the energy loss process of ions in matter. It also discusses the effects of ion impact, such as particle ejection from the surface (sputtering), crater formation, and ion implantation, covering both experimental and theoretical aspects for a betterunderstanding. The second part focuses on the main ion beam analysis techniques, with an emphasis on the Rutherford Backscattering Spectrometry (RBS) technique.

The third chapter describes the ion beam interaction laboratory at the Ruđer Bošković Institute, detailing both accelerators and all existing beam lines.

Finally, the fourth chapter discusses the experimental procedures undertaken to achieve the thesis goals and concludes with the presentation of the results.

Chapter 1

Overview of Platinum Implantation in Silicon Power Diodes

Introduction

Voltage-link converters are essential components in modern drive systems, responsible for controlling inductive loads like electric motors. At these converters are insulated gate bipolar transistors (IGBTs), fast-switching metal oxide semiconductor (MOS) devices and controlled bipolar power transistors engineered with blocking capacities ranging from at least 400 V to over 6500 V, customized to suit specific applications. These IGBTs produce the desired output frequency by synchronously switching on and off in a bridge circuit, often employing pulse-width modulation techniques to achieve optimal efficiency.

To ensure highly efficient switching, platinum is employed to customize the electrical characteristics of silicon power devices, such as silicon power diodes, which are utilized in scenarios involving high-power and high frequency switching of inductive loads. Various methods for introducing platinum are discussed in this chapter, focusing on the most effective techniques. Additionally, the chapter explores the role of platinum in enhancing the performance of power devices.

I. Doping of silicon-based semiconductors

The process of doping silicon-based semiconductors involves the introduction of impurities into an intrinsic crystal to adjust its electrical, optical, and structural properties. Even very low amounts of dopant atoms can wield significant influence over the semiconductor's conductivity [1,2]. Doping levels are categorized as low when roughly one dopant atom is integrated per 100 million silicon atoms, whereas high doping entails the addition of approximately one dopant atom per ten thousand atoms. Excessive doping can push the semiconductor into a state where it behaves more like a conductor than a semiconductor [3]. Doping can be either N-type or P-type, each with distinct effects on the semiconductor's behaviour. In P-type doping, impurities are introduced to foster an excess of positively charged holes within the crystal lattice structure, while N-type doping augments the population of mobile charge carriers with negative polarity. An I-type semiconductor arises when doping incorporates equal amounts of P and N-type dopants.

In summary, any intentional impurity added to a semiconductor to tailor its electrical conductivity qualifies as a dopant. This process is fundamental to semiconductor technology, enabling the creation of devices with finely tuned electrical characteristics.

I.1 P-N junction

The P-N junction is the boundary region between two semiconductor crystals, one doped with N-type and the other with P-type impurities. Within this region, the absence of free charge carriers is notable, as electrons from the N-doped and holes from the P-doped crystal near the interface recombine with each other. This charge movement, known as diffusion, occurs due to a concentration gradient: with a sparse presence of electrons in the P-area and holes in the N-region, the majority charge carriers migrate towards the opposite doped semiconductor. It's important to note that simply pressing of a P-type and an N-doped silicon crystal together does not suffice to form a functional P-N junction, the crystal lattice at the interface must remain uninterrupted [4].

The areas adjacent to the interface become laden with charge due to the loss of free charge carriers. As more charge carriers recombine, the depletion zone expands, leading to an increase in the voltage difference between the N- and P-crystals. At a certain threshold of this potential gap, typically around 0.7 V in silicon [5], the recombination of holes and electrons ceases entirely, as the charge carriers are unable to overcome the electric field.

Applying a positive voltage to the N-type crystal and a negative voltage to the P-type crystal aligns the electric field inside the semiconductor with that of the voltage source, reinforcing the electric field at the P-N junction. Consequently, the oppositely charged free carriers are drawn towards the voltage source's poles (**Fig.1.1a**), enhancing the barrier layer, and impeding the flow of current.

Conversely, when the positive voltage is applied to the P-type and negative to the N-type (**Fig.1.1b**), the external and internal electric fields oppose each other, weakening the inner field. As the inner field is overwhelmed by the outer field, a continuous flow of free charge carriers from the power source to the interface becomes possible, facilitating continuous carrier recombination and thus electric current flow.

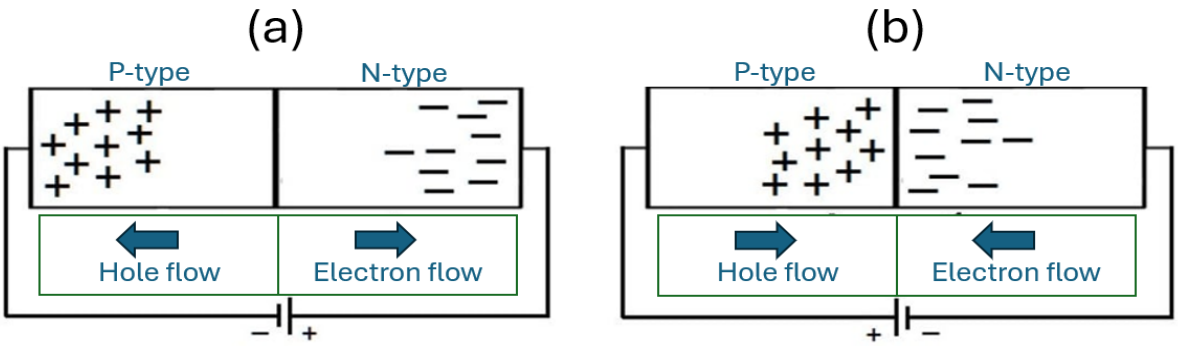

***Figure.1.1**: Applying reverse(a) and direct (b) voltage on P-N junction.*

I.2 Influence of dopant on band structure

Introducing dopants into a Silicon crystal creates energy states within the band gap, positioned very close to the energy band associated with the dopant type. Essentially, impurities acting as electron donors generate states near the conduction band, whereas those functioning as electron acceptors generate states near the valence band. The separation between these energy states and the nearest energy band (illustrated by **Fig.1.2**) is commonly termed as the dopant-site bonding energy (EB), which is typically quite small.

Moreover, dopants play a key role in shifting the energy bands relative to the Fermi level. The energy band corresponding to the dopant with the highest concentration tends to shift closer to the Fermi level. As the Fermi level must remain constant within a system in thermodynamic equilibrium, the stacking of layers comprising materials with varying properties results in numerous beneficial electrical properties induced by band bending, provided that the interfaces are sufficiently clean [1, 4].

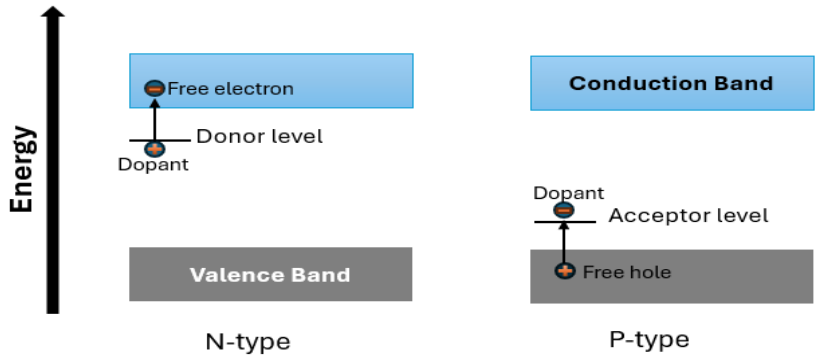

***Figure.1.2:** Dopants on band structure for N- and P-type semiconductors.*

I.3 Silicon dopants elements

In the world of semiconductor technology, the integration of dopant elements into the lattice structure of silicon crystals is important. The distinction between P-type and N-type doping is dictated by the number of outer electrons in the dopant atoms. For instance, elements with 3 valence electrons are used for P-type doping, while those with 5 valence electrons are used for N-type doping.

These dopant elements are further categorized into three main groups: acceptors, donors, and other elements. The acceptors, primarily utilized for P-type doping [6, 7], include aluminium, boron, gallium, and indium. Conversely, the donors are employed for N-type doping [6, 8-10], consisting of phosphorus, arsenic, antimony, bismuth, and lithium. Additionally, there are other elements [6, 11] such as germanium, nitrogen, gold, and platinum, each with its unique role in silicon doping and semiconductor applications.

For instance, aluminium is used for deep P-diffusions but is not widely favored in very large-scale integration (VLSI) and ultra-large-scale integration (ULSI) due to its prevalence as an unintentional impurity. On the other hand, boron, with its controllable diffusion rate, finds common use in complementary metal-oxide-semiconductor (CMOS) technology, and its solubility facilitates efficient emitters in transistors requiring high dopant concentrations.

Similarly, phosphorus, due to its rapid diffusion, is primarily employed for bulk doping or well formation, particularly in solar cells. Arsenic, with its slower diffusion rate, is preferred for diffused junctions and buried layers, finding extensive use in VLSI circuits. Antimony serves as an alternative to arsenic, especially in situations where a pure substitutional diffusion mechanism is desirable, as seen in heavy doping for power devices and epitaxial substrates.

Other elements like germanium and nitrogen play critical roles in band gap engineering, defect suppression, and mechanical strengthening of silicon crystals. Moreover, elements like gold and platinum are instrumental in controlling minority carrier lifetimes, thereby influencing the performance of semiconductor devices, particularly in applications like fast-switching bipolar devices and infrared detection.

In essence, the strategic utilization of dopant elements in silicon crystals is fundamental to the optimization of semiconductor devices for diverse technological applications. The following sections of this chapter will elaborate on how platinum serves as a dopant in the high-power industry.

II. Platinum's influence on power device performance

High-power diodes differ from low-power diodes due to the inclusion of a drift layer situated between the anode (P-doped) and the cathode (n-doped), as shown in **Fig.1.3**. This additional layer equips the diodes with the ability to endure substantial reverse bias before breakdown occurs; the broader the drift layer, the greater the reverse voltage it can stand [12].

During on-state operation, holes are introduced at the anode. With increased injection, these holes attract electrons from the highly n-doped cathode area. Consequently, the drift layer becomes inundated with an excess of charge carriers, resulting in a lower effective resistivity within that region [13].

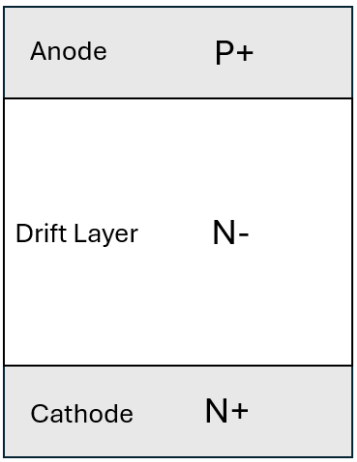

Figure.1.3: *Structure of high-power silicon diode*.

Efforts are focused on achieving high switching speeds to reduce switching losses. However, the presence of inductive loads results in the generation of high induction voltages upon abrupt switch-off, potentially causing harm to the active switch. Therefore, a freewheeling diode in the parallel branch is necessary to facilitate current flow driven by inductance when in the off state. Upon reactivation of the transistor, any remaining current flowing through the diode, called reverse-recovery current, is transferred to the IGBT, significantly contributing to its switch-on losses. In addition to the switching speed and the on-current level of the diode, the storage charge also influences switching losses. Its magnitude is determined by the recombination speed of the electron-hole plasma, which carries the current in the forward direction, during the reverse-recovery process in the diode. The minority carrier lifetime acts as the characteristic time constant for this phenomenon. Therefore, reducing minority carrier lifetime is necessary for minimizing switching losses [14].

II.1 Carrier lifetime reduction via trap introduction

Traditionally, reducing minority carrier lifetime involves introducing noble metals like gold or platinum into the semiconductor device's drift zone. These impurities create energy levels within the forbidden bandgap, acting as traps for charge carriers, thereby shortening their lifetime through trap-assisted recombination, known as Shockley–Read–Hall recombination. Alternatively, irradiation with high-energy particles such as electrons, hydrogen, or helium nuclei can achieve a similar effect. However, this method may lead to undesirable side effects such as gate oxide damage, especially in MOS devices with an integrated reverse diode like a reverse-conducting IGBT (RC-IGBT) [15].

Incorporating recombination centers not only reduces switching losses but also increases forward power loss and reverse power loss in the diode. The precise location of the recombination center in the bandgap is critical for the latter effect. Compared to electron irradiation or gold diffusion, platinum recombination centers exhibit favorable properties. Firstly, both gold and electron irradiation defects result in higher leakage currents compared to platinum [16]. Secondly, devices with gold and platinum diffusion demonstrate superior switching characteristics compared to those subjected to electron irradiation. Consequently, platinum is often preferred, especially in applications requiring higher operating temperatures, which reduces the demands on packaging technology to prevent thermal drift of the overall system.

However, platinum recombination centers have limitations. The temperature dependence of the forward voltage drop becomes problematic with excessively high platinum doping levels due to distinct cold and hot characteristic curves [17]. Without lifetime adjustment, the voltage drop at high temperatures is lower than at room temperature, leading to an increase in forward voltage drop under surge load and associated heating. Increasing Pt concentration leads to a progressively negative temperature coefficient (TC), limiting the extent of lifetime adjustment achievable with Pt. In devices requiring very fast switching speeds, a combination of different lifetime control methods, such as incorporating irradiation techniques alongside Pt diffusion, may be necessary [18]. **Fig.1.4** illustrates the impact of lifetime adjustment with platinum, showing measurements of the reverse-recovery transient current of both a platinum-diffused diode and a diode lacking platinum, where the peak current is notably smaller for the platinum-diffused diode.

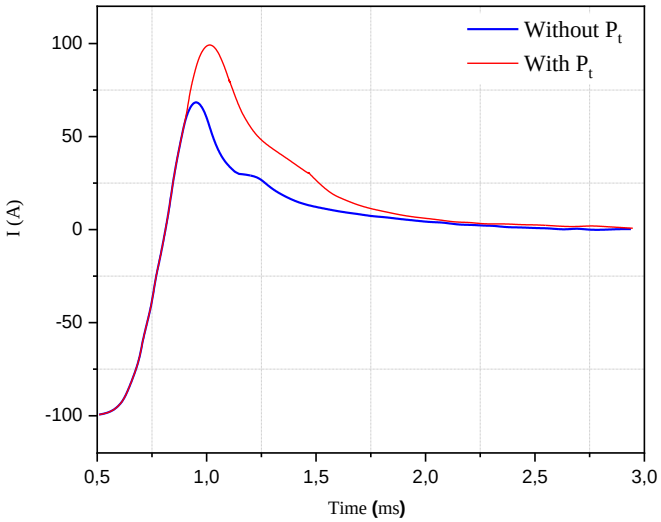

Figure.1.4: *Reverse-recovery transient current measurements of a diode with and without platinum [19].*

II.2 Impact on current snap-off and soft switching

In diodes, especially during rapid switching off, it's important to prevent the sudden cessation of reverse recovery current under fast switching conditions. Abrupt stops could cause high dI/dt values, leading to oscillations and voltage overshoots due to circuit inductances, risking diode damage. Current snap-off presents a significant challenge for diodes employing punch-through design, aimed at reducing switching losses by narrowing the drift zone width. This design dissipates the electric field swiftly through the backside n^+ emitter and a weaker adjacent n-doped field stop zone. Non-punch-through devices dissipate the electric field primarily through the base doping, creating a neutral zone in front of the cathode, facilitating the supply of reverse-recovery current for soft switching.

Besides switching speed, the on-state current significantly affects the diode's reverse-recovery process. A lower on-state current reduces the electron-hole plasma concentration, leading to less available storage charge for reverse-recovery current. Although symmetrical platinum distribution reduces switching losses, it can contribute to a hard switching behavior, especially in punch-through devices, characterized by an early snap-off of reverse-recovery current [19].

III. Modelling of different Pt implantation techniques

For the development of devices, it's imperative to deeply understand the methods used to introduce and customize platinum profiles in silicon. Over the past decades, numerous experiments, varying in annealing time, temperature, wafer thickness, preprocessing, and substrate material, have been documented in the literature [20-25]. Together, these studies have significantly enhanced our understanding of the processes, with underlying mechanisms generally discerned. In a recent comprehensive study by Johnsson [19], all these experiments were thoroughly considered. The resulting models for the three most efficient processes: platinum diffusion from a Pt-silicide layer, post-implantation annealing of platinum, and Platinum diffusion gettering (PDG) of platinum are outlined in this section.

III.1 Pt diffusion from a Pt-silicide layer

For the modulisation of the Pt diffusion from Pt-silicide layer process, four distinct species: platinum on substitutional sites (Pts), platinum on interstitial sites (Pt_i), silicon self-interstitials (I), and vacancies (V) are involved in most of the models found in the literature [26,27]. Among these, the substitutional platinum is presumed to be electrically active, and it is the concentration of electrically active platinum that has been primarily measured in numerous studies. This form of platinum is considered immobile, yet its concentration fluctuates as interstitial platinum atoms transition in and out of substitutional lattice sites through interactions with self-interstitials and vacancies.

The Frank–Turnbull mechanism theorizes that interstitial platinum atoms transform into substitutional positions by occupying vacant lattice sites [28]. This process is typically described through reactions, forming the foundation of many diffusion models found in literature.

$$Pt_i + V \underset{k_{FT\leftarrow}}{\overset{k_{FT\rightarrow}}{\rightleftharpoons}} Pt_s \qquad 1$$

In addition, the kick-out mechanism proposes that interstitial platinum atoms migrate into substitutional sites by displacing silicon lattice atoms into interstitial positions [29]. This process can be described through the following reaction.

$$Pt_i \underset{k_{KO\leftarrow}}{\overset{k_{KO\rightarrow}}{\rightleftharpoons}} Pt_s + I \quad (2)$$

Furthermore, to account for these reactions, bulk generation and recombination of vacancies and self-interstitials must be incorporated. This phenomenon can be described through following reactions.

$$I + V \underset{k_{IV\leftarrow}}{\overset{k_{IV\rightarrow}}{\rightleftharpoons}} \emptyset \quad (3)$$

where ∅ represents an unaffected lattice site, the reaction rate constants in the forward direction designated as k_{FT}, k_{KO}, and k_{IV} can be determined using Waite's theory [30], under the assumption of diffusion-limited reactions. Specifically, within the framework of the Frank–Turnbull mechanism, these constants can be formulated as follow:

$$k_{FT\rightarrow} = 4\pi\alpha_{FT}(D_{Pt_i}+D_V) \quad (4)$$

Here, α_{FT} represents the reaction radius. D_{Pt_i} and D_V signify the diffusion coefficients of Pt_i and V, respectively. The reaction is presumed to occur promptly when the two defects approach each other within a distance of α_{FT}. These reaction radii are anticipated to be roughly equivalent to the spacing between two silicon atoms. The reaction rate constant in the opposite direction, denoted as $k_{FT\leftarrow}$, can be determined based on the concentrations at steady state.

$$k_{FT\leftarrow} = k_{FT\rightarrow}\frac{C_{Pt_i}^{sol}C_V^{eq}}{C_{Pt_s}^{sol}} \quad (5)$$

The solubility concentrations of Pt_i and Pt_s, represented by $C_{Pt_i}^{sol}$ and $C_{Pt_s}^{sol}$ respectively, along with the equilibrium concentration of vacancies denoted as C_V^{eq} are factors in the reaction. Similar expressions are utilized for the reaction rates in other reactions.

The model was expanded by Quast [31] to incorporate the interplay between platinum and immobile vacancy impurity complexes. This entailed introducing VO_2 complexes for CZ-grown silicon and suggesting two variants of vacancy nitrogen complexes for FZ-grown silicon, of which only one interacts with platinum [31]. Similarly, Johnsson [12] identified the necessity of incorporating these interactions to account for variations resulting from substrate material and preprocessing. To describe the interaction between interstitial platinum and these

immobile vacancy impurity complexes, Johnsson [12] introduced the VX species along with a corresponding quasi-chemical reaction.

$$Pt_i + VX^{k_{VX}} \rightarrow Pt_s + X \qquad 6$$

The reaction rate k_{VX} represents the rate at which Pt_i transitions to a substitutional state by interacting with a vacancy impurity complex. This rate is described by Waite's theory [30], assuming diffusion-limited reactions as outlined in Equation 4. Depending on the type of vacancy impurity complex [12], the inclusion of a reaction barrier may be necessary. The reverse reaction is considered improbable, and it is assumed that the impurity product X does not react with any other species. Following the binary reactions methodology, as described by Pichler [32], Equations 1, 2, 3, and 6 lead to a system of linked continuity equations for the involved species, incorporating diffusion terms for the mobile species.

III.2 Platinum implantation

Ion implantation stands as a prominent method for doping silicon wafers. Particularly for platinum, it offers economic competitiveness, granting an extra design facet, enhanced reproducibility, and precise dose control when compared to diffusion from a Pt-silicide layer. Nonetheless, a comprehensive comprehension of platinum diffusion during post-implantation annealing is imperative for maximizing the potential of this technology. Modelling and simulation of devices serve as customary tools in development, aiding in the prediction and optimization of device performance.

The modelling of post-implantation annealing of platinum in silicon involves extending the platinum diffusion model from a Pt-silicide layer where the platinum is sourced from the implanted profile, typically located near the surface. The Giles' model [33] effectively describes implantation damage, assuming rapid recombination of point defects. However, due to the high mass of platinum atoms, multiple self-interstitials may form for each substitutional platinum atom.

Incomplete activation of platinum is another phenomenon to consider, where only a fraction of implanted platinum atoms remains electrically active after annealing. This was initially observed by Badr [34] and confirmed by subsequent experiments. The "missing" platinum likely exists in complexes such as clusters or precipitates. Badr's empirical dynamic cluster

model [34] suggested one cluster type formed from two substitutional platinum atoms and three self-interstitials. Further experiments by Hauf et al [35]. and Johnsson [12] revealed that modifications to Badr's model were necessary to describe experimental results accurately.

Experimental results for various doses and annealing temperatures [36-38], along with simulations using Johnsson's model [12]., were compared to understand post-implantation annealing. Higher temperatures resulted in higher concentrations of Pt_s, with significant platinum found in precipitates or clusters, especially at lower annealing temperatures. The challenge lies in replicating these complex clustering patterns, with models like Johnsson's heuristic model addressing this through a moment-based approach. Johnsson's model can be expressed by the following reactions.

$$Pt_s + Pt_i \rightarrow^{g1} Pt_2 + V \quad (7)$$

$$Pt_2 \rightarrow^{d1} 2Pt_i + V \quad (8)$$

$$Pt_2 + Pt_i \rightarrow^{g2} Pt_{ppt} \quad (9)$$

$$Pt_{ppt} + Pt_i \rightarrow^{g_{ppt}} Pt_{2ppt} \quad (10)$$

$$Pt_{ppt} \rightarrow^{d_{ppt}} Pt_i + Pt_{ppt} \quad (11)$$

Pt_{ppt} represents a platinum precipitate irrespective of its size. Thed_{ppt} and g_{ppt} signify dissolution and generation rates, respectively. The model incorporates a single intermediate cluster, Pt_2, formed from one Pt_s atom and one Pt_i atom, enhancing its probability in the implanted region compared to the bulk. This underpins the formation and growth of precipitates in the implanted region in line with experimental findings. Pt_2 clusters are presumed to dissolve into two platinum interstitials. Equations 9, 10, and 11 delineate the modelling of precipitate formation, growth, and dissolution. Additionally, the evolution of precipitate size is addressed through the subsequent set of differential equations:

$$\frac{\partial n_{ppt}}{\partial t} = 3g_2 C_{Pt_i} C_{Pt_2} + g_{ppt} C_{Pt_i} C_{Pt_{ppt}} - d_{ppt} C_{Pt_{ppt}} \quad (12)$$

$$\frac{\partial C_{Pt_{ppt}}}{\partial t} = g_2 C_{Pt_i} C_{Pt_2} - d_{ppt} \frac{C_{Pt_{ppt}}}{n_{ppt}} C_{Pt_{ppt}} \quad (131)$$

Johnsson's model for post-implantation annealing of platinum in silicon [12] encompasses various processes including self-interstitial agglomeration, platinum precipitation, and

mechanisms like the Frank-Turnbull and kick-out mechanisms. Immobility is assumed for complexes and precipitates of self-interstitials and platinum. Neumann boundary conditions are applied for interstitial platinum at both surfaces, while intrinsic point defects and immobile species follow the same boundary conditions as diffusion from a Pt-silicide layer. Despite earlier findings suggesting substrate material insignificance by Badr et al [34]. Johnsson [12] later revealed its potential impact, especially considering prior processing steps. Calibration of reaction rate constants against experimental data from own studies and Badr's [39] allowed for reproducibility of experiments within a broad range of annealing temperatures and implanted doses (**Fig.1.5** shows an example for 850°C). However, the precipitation model is acknowledged as a simplification and lacks consideration for further cluster sizes and interactions with intrinsic point defects.

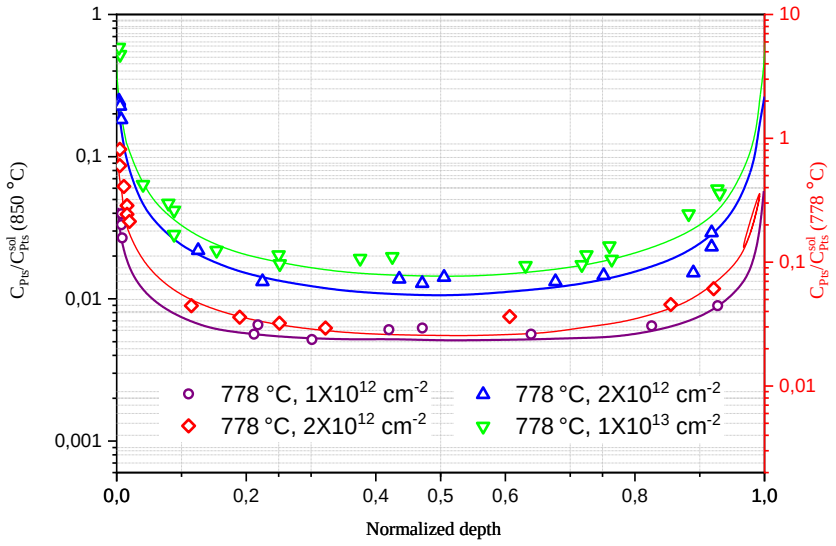

Figure.1.5: *DLTS measurements (symbols) and corresponding simulation results (lines, using the model from Johnsson [12]) of after implantation (150 keV) and annealing at 850°C.*

III.3 Platinum diffusion gettering (PDG) in Silicon

To initiate Platinum diffusion gettering (PDG) in Silicon, a high concentration of phosphorus is introduced at one surface of the silicon wafer. Phosphorus can be deposited as a phosphorus glass or implanted via ion implantation, with subsequent gettering occurring during annealing. Phosphorus primarily diffuses through vacancies at high concentrations and through self-interstitials at lower concentrations. The latter induces self-interstitial supersaturation as interstitial phosphorus atoms displace lattice atoms to become substitutional. In cases of

implanted phosphorus, annealing of the implantation damage further increases self-interstitial concentration, extending beyond the phosphorus profile. Silicon self-interstitials generated thus diffuse towards the bulk, displacing substitutional platinum to interstitial sites via the kick-out mechanism in reverse. Interstitial platinum atoms subsequently migrate towards the phosphorus-rich region, potentially forming complexes with phosphorus atoms [40] or platinum silicide precipitates [41]. Macroscopically, this complex formation acts as a sink for self-interstitials, effectively gettering them from the bulk. This interplay between self-interstitial mobilization and phosphorus atom gettering results in asymmetric concentration profiles of substitutional platinum, as illustrated in **Fig.1.6**.

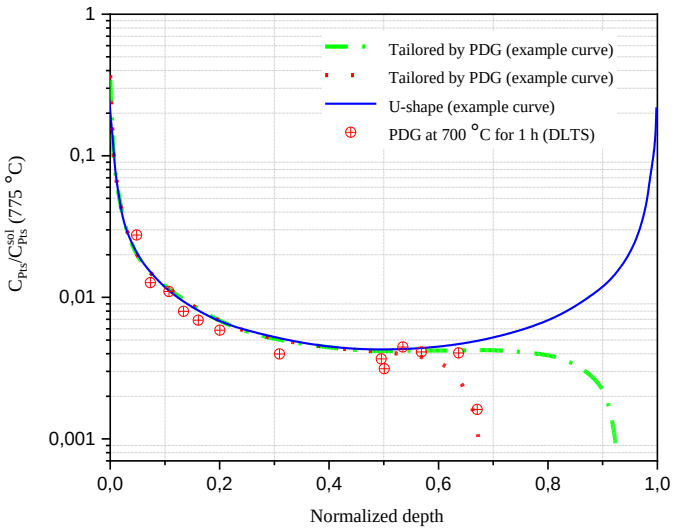

Figure.1.6: *Illustrative example curves of one symmetrical and two asymmetrical profiles of platinum together with one measured profile after PDG* ***[19].***

PDG investigations by Zimmermann [22] focused on gold and platinum gettering using phosphorus deposition. Zimmermann determined the surface's self-interstitial supersaturation and included additional equations to describe gold or platinum capture in the phosphorus-rich region. Similarly, Badr studied PDG of platinum via ion implantation of phosphorus and annealing within a temperature range of 827°C to 852°C [39]. Initial concentration profiles from platinum diffusion from the Pt-silicide layer were used, with Dirichlet boundary [42]. conditions for both self-interstitials and vacancies, where α^{I}_{ss} represented time-dependent self-interstitial supersaturation.

$$C_I^{surface} = \alpha_{ss}^I \times C_I^{eq} \quad (14)$$

$$C_V^{surface} = \frac{1}{\alpha_{ss}^I} \times C_V^{eq} \quad (15)$$

The platinum gettering by phosphorus was simplified in Badr's model as a diffusion-limited sink for interstitial platinum at the phosphorus-implanted surface. Although Badr's model [34] captured the main aspects of platinum PDG in silicon, it required different parameters for C_I^{eq} than those used for platinum diffusion from silicide and post-implantation annealing in the same study. Subsequent work by Johnsson [12] revealed inconsistencies with these parameters, especially at lower temperatures.

IV. Depth profile of Pt in silicon

The phenomenon of U-shaped profiles observed in electrically active platinum diffusion presents a departure from typical impurity diffusion profiles. Illustrated in **Fig.1.7**, taken from Johnsson's work [12], is the evolution of substitutional platinum concentration across wafer depth during annealing at 800°C from a Pt-silicide layer. The simulation utilized homogenous initial conditions, setting the initial concentration of self-interstitials significantly higher than the homogeneous vacancy concentration. Initially, interstitial platinum atoms rapidly diffuse from the silicide into the wafer, decorating existing vacancies in the bulk. Over time, the substitutional platinum concentration extends deeper into the wafer. Notably, the surface serves as both a source of new vacancies for the Frank–Turnbull mechanism and a sink for self-interstitials generated by the kick-out mechanism, facilitating rapid increase in substitutional platinum concentration at the surfaces. This effect is observed first at the surface with the Pt-silicide layer and later at the opposite surface, leading to the formation of the U-shaped profile. The establishment speed of the U-shape depends on wafer thickness, annealing temperature, and initial concentrations of intrinsic point defects. With platinum sources on both surfaces, a symmetric profile would form more rapidly. Ultimately, bulk concentration increases over time as self-interstitials out-diffuse from the bulk or vacancies in-diffuse from the surfaces, enabling the Frank–Turnbull and kick-out mechanisms. To sum up, the U-shaped profile arises from the rapid diffusion of interstitial platinum, along with mechanisms such as the Frank–Turnbull mechanism, the kick-out mechanism, and the transport of intrinsic point defects. Comparable U-shaped profiles are noted in cases where platinum is introduced through ion implantation and subsequent annealing, driven by these identical principles.

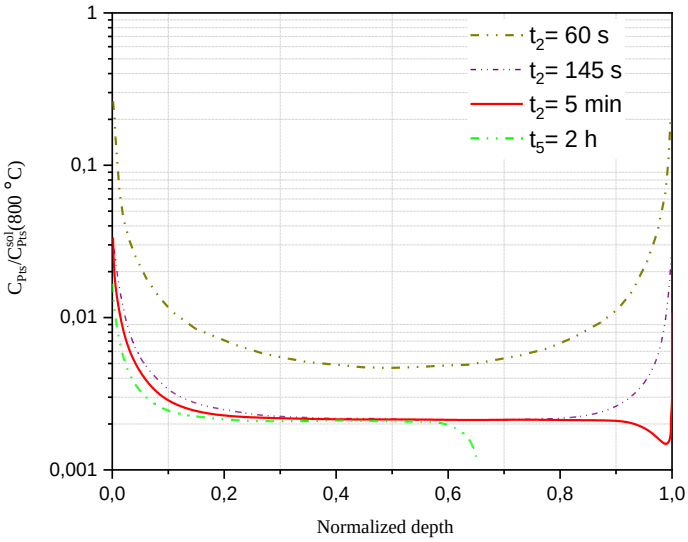

***Figure.1.7**: U-shaped platinum depth profile obtained by one-side diffusion during annealing at 800°C [19].*

V. Sample preparation steps by Platinum diffusion from a Pt-silicide layer

Platinum implantation into silicon can be conducted using various methods, as detailed earlier in this chapter. The process involved for preparing the samples for the thesis work was platinum diffusion from a Pt-silicide layer method presented by **Fig.1.8**.

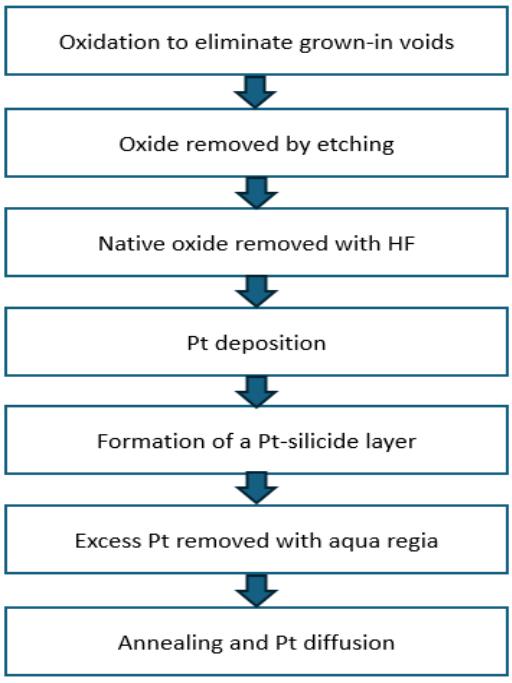

***Figure.1.8:** Overview of the processing steps for Pt diffusion through Pt-silicide layer process.*

V.1 Elimination of grown-in voids by oxidation

Prior to the introduction of platinum in the silicon, a high-temperature oxidation step must be performed. Schulze [44] illustrated that high-temperature oxidation could eliminate inherent voids, a common occurrence post crystal growth. They examined carrier lifetime in FZ-grown wafers and observed an uneven lateral distribution associated with high concentrations of D-defects at the wafer center. These defects, enriched with heavy metals from contamination, reduced carrier lifetime in that specific area. Schulze [44] concluded that high-temperature oxidation effectively eradicated these D-defects. The wafers in this study annealed at 1000°C in oxidizing atmospheres, employing various types of oxidizing agents. The oxidation duration for wafers subsequently implanted with platinum was approximately 90 minutes, while for wafers receiving platinum from a Pt-silicide layer, it extended to around 8.5 hours. Following the oxidation anneals, the temperature was gradually reduced in N2 ambient, and the resulting oxide layer was subsequently removed. This oxidation process remained consistent for both FZ- and CZ-grown wafers.

V.2 One-side deposition of a Pt-silicide layer

The first stage entailed cleansing the wafers with hydrofluoric acid (HF) to remove the native oxide layer. Subsequently, platinum is applied onto the surface through electron-beam evaporation within vacuum conditions. Annealing the wafers at 470°C in a nitrogen atmosphere for 65 minutes promoted the development of the Pt-silicide layer. Any excess platinum present on the surface, not contributing to PtSi formation, has to be removed using aqua regia [12].

V.3 High temperature Annealing

Platinum diffusion in silicon wafers typically involves annealing at temperatures between 700°C and 950°C. The wafers must be placed in a furnace, then gradually heated to the target temperature at 8.3 K/min. Once at the desired temperature, the wafers are annealed for approximately 2 hours, followed by cooling at 4.6 K/min. This controlled heating and cooling process, known as standard ramping [12]., begins in an O_2 atmosphere for the ramp-up and first 30 minutes, then switches to an inert N_2 environment for the remaining time.

Chapter 2

Ion-Solid Interactions and IBA Techniques

Part 1: Theoretical Background

Introduction

Insight into the physical mechanisms of ion solid interactions is of fundamental importance for the understanding of the present work. In this part of the thesis, the physical processes relevant for energetic ions traversing solid matter, are outlined. we start by highlighting the Interaction of charged particle with matter and reviewing the main concepts of the interaction between two particles (binary collision). Within this framework, we derive the various equations that allow modelling the interaction parameters. Additionally, we introduce the concept of scattering from target nuclei, and we present the process of loss of energy from ions in the matter, on one hand, through electronic excitations, which are predominant in the high-energy domain, and on the other hand, through nuclear collisions towards the end of the path (low energies). Furthermore, we delve into the effects induced by the impact of the ions, addressing phenomena such as the ejection of particles from the surface under ions bombardment "sputtering", crater formation and ion implantation. Both experimental and theoretical aspects are presented to provide a comprehensive understanding. Finally, the interactions with target electrons are discussed.

I. Interaction of charged particle with matter

During the interaction of a material by charged particles, the particles gradually transfer their energy to the medium through a series of interactions [49, 50]., which can potentially lead to damage to the target. For a more thorough understanding of these processes, it may be helpful to consider the first interaction model between an ion and surface atom which called Binary Collision Approximation.

I.1 Binary collisions between two charged particles

In the laboratory frame, the single binary collision model relies on two fundamental principles: the conservation of energy and momentum. Let's consider an elastic collision between an incident projectile characterized by mass m_p and velocity v_0 in which its kinetic energy can be expressed as $E_0 = \frac{1}{2} m_p {v_0}^2$[45], and a stationary target atom with mass m_t $(v_0 = 0)$, and therefore possesses no kinetic energy before the collision (see **Fig.2.1**).

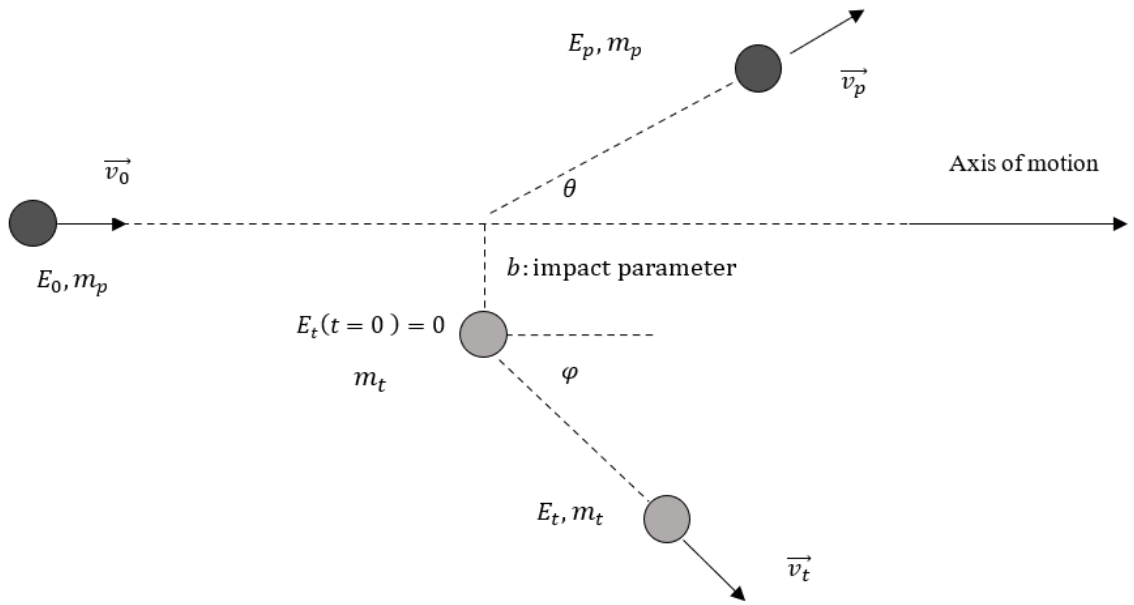

Figure.2.1*: Binary collision illustration between a projectile and a stationary target within the laboratory frame.*

Here, θ denotes the deflection angle of the projectile at which it deviates while φ represent the recoil angle of the target atom after the collision. Following the collision, the projectile has a velocity v_p thus it possesses a momentum $P_0$and P_p . Simultaneously, the target atom acquires a velocity v_t gaining kinetic energy E_t in which it possesses momentum P_t after collision. In the interaction, there might be inelastic energy loss denoted by Q defined as the remained energy between initial and final balance of total energy. This loss can occur during the collision process, resulting in the conservation laws of energy and momentum equations in the laboratory frame [46],

$$E_0 = E_p + E_t + Q$$
$$P_0 = P_p + P_t \quad (26)$$

Which can be expressed as [46].

$$\frac{1}{2}m_p v_0^2 = \frac{1}{2}m_p v_p^2 + \frac{1}{2}m_t v_t^2 + Q$$
$$m_p\overrightarrow{v_0} = m_p\overrightarrow{v_p} + m_t\overrightarrow{v_t} \quad (17)$$

In this part of thesis, we are considering the simplest case when Q = 0. Therefore, the collision is elastic. The energy and the momentum conservation laws in which the velocities are always considered positive are simply given by [47]:

$$E_0 = E_p + E_t$$

$$\frac{1}{2}m_p v_0^2 = \frac{1}{2}m_p v_p^2 + \frac{1}{2}m_t v_t^2 \quad (18)$$

$$m_p v_0 = m_p v_p \cos\theta + m_t v_t \cos\varphi$$

$$0 = m_p v_p \sin\theta - m_t v_t \sin\varphi \quad (19)$$

The angles θ and φ correspond to the projectile's scattering angle and the recoil angle of the target atom respectively. It's important to note that θ is measured in the opposite direction to φ. See **Fig.2.1** for a more intuitive depiction.

I.2 Scattering energy

The kinetic energy of the projectile after the interaction is of interest, it can be deduced from the conservation laws. Specifically, the ratio between the final projectile energy E_p and the initial energy E_0. The objective now is to express this ratio $\left(\frac{E_p}{E_0}\right)$ in terms of the projectile and target properties (masses and scattering angle).

The equations system 18 and 19, serves as a good starting point [48]. After rearranging the equations ($\cos\theta$ is on one side, and then square both sides) and using the trigonometric identity ($\sin^2\theta = 1 - \cos^2\theta$), we defined the ratio of the velocities $\left(\frac{v_p}{v_0}\right)$ as:

$$\left(\frac{v_p}{v_0}\right)^2 = \left(\frac{m_t v_t}{m_p v_0}\right)^2 - 1 + 2\left(\frac{v_p}{v_0}\right)\cos\theta \quad (20)$$

After using Eq16 for energy conservation, we got

$$m_t v_t^2 = m_p v_0^2 - m_p v_p^2 - 2Q \quad (21)$$

By dividing both sides by $m_p v_0^2$, and using $E_0 = \frac{1}{2}m_p v_0^2$, the equation above is written as

$$\left(\frac{m_t v_t}{m_p v_0}\right)^2 = \frac{m_t}{m_p}\left[1 - \left(\frac{v_p}{v_0}\right)^2 - \frac{Q}{E_0}\right] \quad (22)$$

Substituting this into Eq20:

$$\left(\frac{v_p}{v_0}\right)^2 = \frac{m_t}{m_p} - \frac{m_t {v_p}^2}{m_p {v_0}^2} - \frac{m_t Q}{m_p E_0} - 1 + 2\left(\frac{v_p}{v_0}\right)\cos\theta$$

$$0 = \left(\frac{v_p}{v_0}\right)^2 \left[1 + \frac{m_t}{m_p}\right] - \left(\frac{v_p}{v_0}\right) 2\cos\theta + \left[1 - \frac{m_t}{m_p} + \frac{m_t Q}{m_p E_0}\right]$$

With $A = \frac{m_t}{m_p}$, this equation can be solved for $\frac{v_p}{v_0}$, and thus $\frac{E_p}{E_0}$ is obtained.

$$\frac{v_p}{v_0} = \frac{\cos\theta \pm \sqrt{(1 - \sin^2\theta) - 1 + A - A + A^2\left(1 - \frac{Q}{E_0} - \frac{Q}{E_0 A}\right)}}{(1 + A)} \qquad 23$$

The kinetic energy of the projectile in the laboratory frame, known as the scattering energy, is given by:

$$\frac{E_{p\pm}}{E_0} = \left(\frac{\cos\theta \pm \sqrt{(Af)^2 - \sin^2\theta}}{(1 + A)}\right)^2 \qquad 24$$

This relation agrees with the literature, in which $Af^2 = \left(1 - \frac{1+A}{A}\frac{Q}{E_0}\right)$ [46].

Here it is assumed that the collision is instantaneous. This equation leads to two solutions, but they may not always both be valid. When $Af < 1$, both E_{p+} and E_{p-} are valid, whereas only E_{p+} is valid when $Af \geq 1$ [46]. In the context of an elastic collision, this implies that both solutions are valid when $m_p > m_t$, whereas only E_{p+} is valid if $m_p \leq m_t$.

Note that this relationship exhibits symmetry in θ , and the argument of the square root can become negative when $Af < 1$, thus introducing a maximum scattering angle. This maximum angle can be determined from:

$$\theta_{max} = \pm\arcsin(Af) \qquad 25$$

If $Af > 1$, the scattering angle is not bounded, $-180° < \theta < 180°$. In the case of an elastic collision, where $f^2 = 1$, this leads to a familiar equation [45, 47-48] which is plotted in **Fig.2.2**.

$$E_{p\pm} = kE_0 \qquad 26$$

$$k = \left(\frac{\cos\theta \pm \sqrt{\left(m_t/m_p\right)^2 - \sin^2\theta}}{1 + m_t/m_p} \right)^2$$

This formula is used in Rutherford backscattering spectrometry (RBS) to characterize the energy of a particle scattered at a given angle. This energy depends on incident energy, target and projectile masses. When the projectile is much lighter than the target $m_p \ll m_t$, all deflection angles are kinematically possible, and the projectile's energy remains almost unchanged, while the recoil angle of the target atom ranges between 0° and 90°. Conversely, in the case where $m_p > m_t$,which is the most common scenario with Au^+ ions, the projectile's energy also varies little, and only forward angles are allowed (small deflections). In the particular case where $m_p = m_t$, the projectile can be stopped in a collision where it transfers all its energy to the scattering atom, ($T_{max} = E$), for more detail see paragraph I.3.

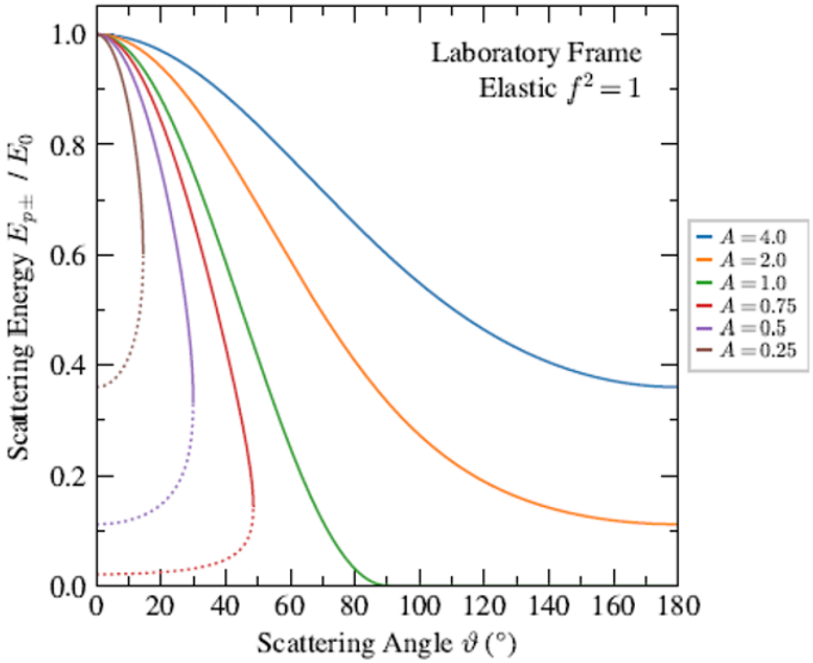

***Figure.2.2**: Kinematics of elastic scattering for the scattered projectile for different mass ratio.*

I.3 Recoil energy

Recoil energy is the energy transferred to the target atoms, in which is defined as E_t and can be found in a very similar way. Therefore, the goal is to express the ration $\frac{E_t}{E_0}$ in terms of projectile and target, and the recoil angle.

Following a similar approach as in Eq22, we found that.

$$\left(\frac{v_t}{v_0}\right)^2\left[1+\frac{m_t}{m_p}\right]-\left(\frac{v_t}{v_0}\right)[2\ \cos\varphi]+\ \frac{m_p Q}{m_t\ E_0}=0 \qquad 27$$

With $A=\frac{m_t}{m_p}$, this equation can be solved for $\frac{v_t}{v_0}$;

$$\frac{v_t}{v_0}=\frac{\cos\varphi\pm\sqrt{1-\left(\frac{1+A}{A}\right)\left(\frac{Q}{E_0}\right)-\sin^2\varphi}}{(1+A)} \qquad 28$$

Consequently, the kinetic energy transferred to the target atom in the laboratory frame, which referred to the recoil energy, is given by:

$$\frac{E_{t\pm}}{E_0}=A\left(\frac{\cos\varphi\pm\sqrt{f^2-\sin^2\varphi}}{1+A}\right)^2 \qquad 29$$

This equation aligns with findings in the literature [46].In the case of an elastic collision, in which $f^2=1\ (\cos\varphi\pm\sqrt{f^2-\sin^2\varphi}$ can take either 0 or $2\cos\varphi)$, the recoil can be expressed as [47,50]:

$$T=E_{t+}=\frac{4m_t m_p}{(m_t+m_p)^2}E_0\cos^2\varphi \qquad 30$$

This relationship is plotted using the code blocks and depicted in **Fig.2.3**. It is noticeable that in the elastic collisions, only one solution exists for the recoil energy, contrasting with the scattering energy, which has two solutions. Unlike the scattering angle θ, the recoil angle φ is bounded within the range -90°≤φ≤90° [47].

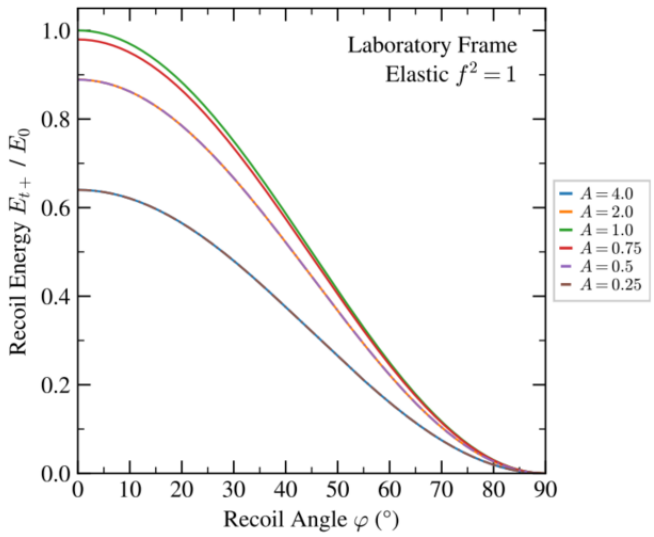

***Figure.2.3**: Kinematics of elastic recoil atom with different mass ratio.*

For a head-on collision, the maximum transferred energy can be expressed as follows.

$$T_{max} = \frac{4m_t m_p}{(m_t + m_p)^2} E_0 \quad (31)$$

In which,

$$\cos(\varphi) = 1 \Leftrightarrow \sin(\varphi) = 0 \Leftrightarrow \sin(\theta) = 0 \Leftrightarrow \theta = 0 \text{ or } \theta = \pi$$

II. Relevant parameters of the ion-material interaction

Throughout this part, we will describe the relevant parameters of the ion-matter interaction, in which the irradiation id defined. In general, the flux (ϕ) representing the number of incident particles sent to the target per unit surface area and per unit time ($cm^{-2}. s^{-1}$) and the fluence (F) corresponding to the total number of particles received by the target per unit surface area (cm^{-2}): $F = \int_0^t \phi \, dt$, where t is the total time of irradiation expressed in seconds are considered as the main parameters during the irradiation. The other relevant parameters of the interaction such as collision cross section and stopping power are also described in this section.

II.1 Collision cross sections

To fully describe a collision, it's also necessary to know the scattering angle of the projectile as a function of the initial conditions and the type of interaction between both projectile and target atoms such as the mass, charge, velocity, impact parameter, and interaction potential. Referring to **Fig.2.4**, we can see that in the center-of-mass frame, if a virtual particle (with reduced mass $\mu = \frac{m_p m_t}{m_p + m_t}$, and center-of-mass energy $E_{CM} = \frac{1}{2}\mu \|v_p - v_t\|^2$) arrives within a ring of radius *b* (impact parameter) and width db, it will be scattered into an elementary solid angle dΩ, at an angle θ, with an opening dθ. The surface area of the entrance ring dσ is given in terms of the collision impact parameter by $d\sigma = 2\pi b db$. This surface area of the entrance ring can be seen as an effective area through which any incident virtual particle will be scattered at an angle between θ and θ + dθ. This dσ surface area is equated to the differential collision cross-section, which defined as a measure of the probability of an ion being deflected at an angle θ [100].

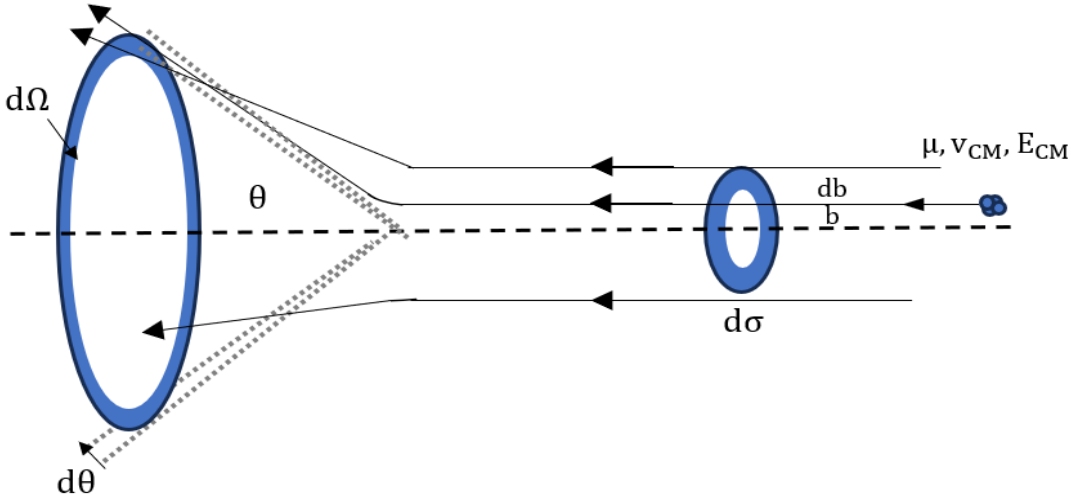

***Figure.2.4**: Incidence within a differential ring at a given impact parameter results in a scattering into a differential solid angle.*

However, using the differential solid angle $d\Omega = 2\pi \sin\theta \, d\theta$, the differential collision cross-section is written as:

$$\frac{d\sigma}{d\Omega} = \frac{b(\theta)}{\sin\theta} \frac{db}{d\theta} \qquad 32$$

Therefore, to calculate it, the interaction potential must be known. The simplest case is Coulomb interaction potential as it does not consider the screening effect of the nucleus charge by the electrons. The potential energy between two charged particles Z_1 and Z_2 separated by a distance r is given by:

$$V(r) = \frac{Z_1 Z_2 e^2}{r} \qquad 33$$

Where e is the elementary charge,

We define the collision diameter r_m as: $\frac{Z_1 Z_2 e^2}{r} = \frac{1}{2} \mu v_{CM}^2$

$$r_m = \frac{Z_1 Z_2 e^2}{E_{CM}} \qquad 34$$

r_m represents the distance of minimum approach during a central collision of particles ($b = 0$). Concerning the scattering angle in the center-of-mass frame is written simply as:

$$\tan\left(\frac{\theta}{2}\right) = \frac{r_m}{2b} = \frac{Z_1 Z_2\, e^2}{2bE_{CM}} \Rightarrow b = \frac{Z_1 Z_2\, e^2}{2E_{CM}} \frac{1}{\tan\left(\frac{\theta}{2}\right)}$$

$$b = \frac{Z_1 Z_2\, e^2}{2E_{CM}} cot\left(\frac{\theta}{2}\right) \quad (35)$$

By combining all these equations, the differential cross-section in function of scattering angle known as the Rutherford formula is written as:

$$\frac{d\sigma}{d\Omega} = \frac{{r_m}^2}{16\sin^4\left(\frac{\theta}{2}\right)} = \left(\frac{Z_1 Z_2\, e^2}{4\, E_{CM}}\right)^2 \frac{1}{\sin^4\left(\frac{\theta}{2}\right)} \quad (36)$$

I.2 Energy loss of the projectile ion

During an ion-matter interaction, the incident ion transfers its energy to the target during the passage through the material. This energy transfer can be described in more detail by examining the different mechanisms that contribute to the energy loss in which we highlight the collision types.

II.2.1 Nuclear collisions (Elastic collisions)

The ion entering the target loses a portion of its energy in collisions with the electrons or nuclei of the target material without any loss of kinetic energy. Instead, the direction and velocity of the ion may change due to the collision. These collisions typically occur when the ion and target particles exchange momentum without any energy exchange in which they are predominant for the low-energy domain (<100 keV). In here, two models are used to represent this phenomenon: collision mechanics (theory of elastic collisions section I.1) and the scattering of a charged particle in a potential (Rutherford scattering).

II.2.2 Electronic stopping (Inelastic collisions)

In inelastic collisions, the ion transfers some of its kinetic energy to the electrons or nuclei of the target material. As a result, the ion loses energy, which can manifest as the excitation of electrons to higher energy levels or even the ejection of electrons from the material. This process leads to a net decrease in the kinetic energy of the ion as it traverses the material.

Inelastic collisions are significant contributors to the overall energy loss experienced by the projectile ion.

II.2.3 Nuclear excitations and reactions

Nuclear excitations and reactions occur only with neutrons (γ-radioactivity), and in exceptional cases with very energetic ions (≥ GeV). Here, the ion can also interact directly with the atomic nuclei of the target material and transfer his energy to the nucleus, often leading to nuclear reactions such as elastic or inelastic scattering, or even nuclear fusion or fission, depending on the energy and nature of the incident particles.

II.2.4 Bremsstrahlung

Bremsstrahlung is an electromagnetic wave emitted by a moving charged particle during its acceleration or deceleration. In practice, the emission of electromagnetic radiation (bremsstrahlung) or the creation of electron-positron pairs in highly energetic collisions is only considered in the case of electrons.

II.2.5 Cherenkov effect

The Cherenkov effect occurs when a charged particle moves through a medium faster than the speed of light in that medium. This effect requires considerable velocities and is significant only for gamma rays or very fast electrons.

II.3 Stopping power

In this context, the particle undergoes a series of interactions with the target medium, leading to the gradual loss of its energy. These interactions vary in nature, encompassing processes such as scattering, ionization, and excitation. As the particle traverses the material, it gradually loses energy until it either comes to a complete stop at a certain depth within the medium or experiences backscattering at the surface. Therefore, the phenomenon, known as stopping power, quantifies the energy loss of the particle per unit distance travelled through the target material. is defined by:

$$P_E = -\frac{dE}{dx} = \lim_{\Delta x \to 0}\left(\frac{\Delta E}{\Delta x}\right) \quad (37)$$

The stopping power can be expressed in keV.nm^{-1} or MeV·g^{-1}·cm^2.

Depending on the considered collisional process, whether inelastic or elastic interactions, electronic stopping power and nuclear stopping power are defined. Electronic stopping power typically dominant at lower energies, refers to the energy loss per unit length in the target material due to interactions between the incident particle and the electrons of the material. In contrast, nuclear stopping power reflects the energy loss resulting from interactions between the incident particle and the atomic nuclei of the target material, often predominant at higher energies. However, according to J. Lindhard and colleagues [51-54], the total energy loss or stopping power per unit length in the target is obtained by summing the contributions from both nuclear and electronic stopping powers:

$$\left.\frac{dE}{dx}\right|_{total} = \left.\frac{dE}{dx}\right|_n + \left.\frac{dE}{dx}\right|_e \quad (38)$$

This combined stopping power provides a comprehensive measure of the energy dissipation experienced by the projectile particle as it traverses the target material. In this case, the total stopping cross-section S_t is defined as:

$$S_t = S_n + S_e$$

In which S_e, S_n present the electronic and nuclear cross sections $\left(S = \frac{1}{N}\left.\frac{dE}{dx}\right|\right)$, and N is the atomic concentration of the target.

Note that the stopping power allows us to assess the actual path of the projectile ion in the material. During the interaction, the velocity of the incident ion decreases, and the ion becomes trapped in the material. It is then possible to determine the range R of the ion along its trajectory in the target, given by the relation:

$$R = \int_0^{E_0}\left(\frac{dE}{dx}\right)^{-1} dE, \quad (39)$$

where E_0 represents the kinetic energy of the ion upon entering the medium.

II.3.1 Stopping power estimation

Depending on the incident ion velocity, the stopping power S(E) is divided into three main regions [55] (see **Fig.2.5**),

- **Zone I** present low energy region, where the velocity is below the Bohr velocity v_0. In which the nuclear contribution is predominate, especially for heavy ions. Here, the ions are called *slow.*
- **Zone II** present intermediate energy region, which is dominated by electronic stopping (up to 1 MeV).
- **Zone III** present "High energy region" known as the *Bethe-Block* zone, in which the stopping power decreases as energy increases. Here, the ions are called *fast* or *swift*.

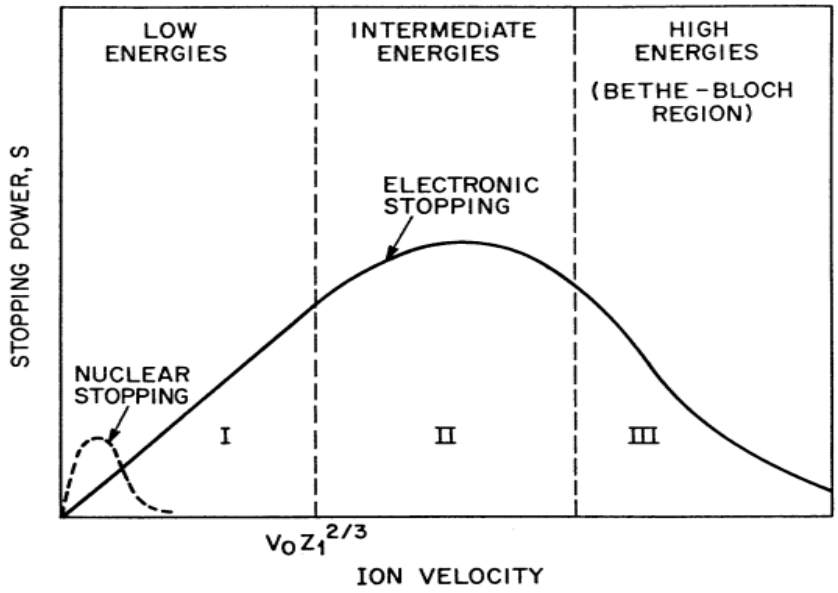

Figure.2.5*: Nuclear and electronic stopping power as a function of incident ion velocity [55].*

v_0 present Bohr velocity $\left(v_0 = \frac{e^2}{\hbar} = 2.2 \times \frac{10^8 \text{cm}}{\text{s}} = 25 \text{ keV/uma}\right)$.

II.3.1.1 Estimation of nuclear stopping power

The interactions between the incident ion and the atoms of the target are treated as elastic collisions between two particles, governed by the laws of classical mechanics. For energy transfers leading to atomic displacements, the interaction is purely Coulombic. In this case, it has been shown in the previous section that the kinematic factor K (Eq 26)) allows defining the energy loss of the projectile as a function of its scattering angle. The energy T transferred to the target atom is then given by*:* $T = E_0 - E_1 = E_0(1 - K)$. Knowing both T and the

differential scattering cross-section dσ/dΩ (Eq.40) for each scattering angle, it is possible to determine the collision cross-section corresponding to the energy transfer *T* [56].

$$\frac{d\sigma}{dT} = \frac{(\pi Z_1 Z_2 e^2)^2 m_p}{T^2\, E_0\, m_t} \qquad 40$$

In a medium containing N scattering particles per unit volume, the average energy transmitted by the projectile over a path Δx is given by:

$$\overline{T} = N\Delta x \int_{T_{min}}^{T_{max}} T\, \frac{d\sigma}{dT}\, dT$$

With $\overline{\Delta E} = -\overline{T}$ the average energy loss over the path Δx, we can define the average energy loss per unit length of path $\overline{\Delta E}/_{\Delta x} = -\overline{T}/_{\Delta x}$, which is commonly written as the stopping power $-dE/_{dx}$. Still within the framework of elastic collisions occurring in a Coulomb potential, the stopping power is given by [57]:

$$-\frac{dE}{dx} = N\, S_n(E) = N \int_{T_{min}}^{T_{max}} T\, \frac{d\sigma}{dT}\, dT$$

$$-\frac{dE}{dx} = 2\pi\, N\, \frac{m_p}{m_t} \frac{{Z_1}^2 {Z_2}^2 e^4}{E_0} \ln\left(\frac{T_{max}}{T_{min}}\right) = 4\pi\, N\, \frac{{Z_1}^2 {Z_2}^2 e^4}{m_t\, {v_0}^2} n\left(\frac{T_{max}}{T_{min}}\right) \qquad 41$$

In this expression, T_{max} corresponds to the maximum amount of transferable energy during a collision (Eq 31), and T_{min} corresponds to the minimum transferable energy which cannot be zero because if it were, then the stopping power defined previously would tend towards infinity. Therefore, the calculated stopping power corresponds to a description of the deceleration of a charged projectile in a medium where only independent elastic collisions with charged particles in a Coulomb interaction field can occur. In the case of an ion-atom interaction, this description does not consider the electron clouds of the target and projectile, which shield the charges of the atomic nuclei, especially at large impact parameters. To consider this the repulsive force attenuation, a screened Coulomb potential can be used.

➢ L. S. S Model

For relatively low incident energies (typically below 25 keV), the nuclear stopping power can be derived from a screened Coulomb potential (Thomas-Fermi potential). It is originally given by Lindhard, Scharff, and Schiott (L.S.S) and is expressed as function of a_{TF} and ε which

represent Lindhard screening radius for Thomas-Fermi interaction (expressed in angstroms Å), and a reduced energy (dimensionless) [57]:

$$a_{TF}(a_{Lindhard}) = \frac{0.8853\ a_0}{\left(Z_1{}^{1/2} + Z_2{}^{1/2}\right)^{2/3}}\ , \varepsilon = \frac{m_t}{m_p + m_t}\frac{a_{TF}}{Z_1 Z_2 e^2} E_0\ (keV) \qquad 42$$

Where a_0 is Bohr radius ($a_0 = 0.528Å$).

Consequently, the nuclear stopping cross-section $S_n(E)$ can be expressed in a reduced form $S_n(\varepsilon)$ by the relation [13]:

$$-\frac{dE}{dx} = 4\pi\ N\ a_{TF}\ \frac{m_p}{m_p + m_t} Z_1 Z_2 e^2\ \frac{\ln(\varepsilon)}{2\varepsilon(1 - \varepsilon^{-1.49})}$$

$$S_n(E) = \frac{Z_1 Z_2 m_p}{m_p + m_t} 4\pi e^2\ a_{TF}\ S_n(\varepsilon) \qquad 43$$

Hence,

$$S_n(E) = 8.462 \times 10^{-15} \frac{Z_1 Z_2 m_p}{\left(m_p + m_t\right)\left(Z_1{}^{1/2} + Z_2{}^{1/2}\right)^{2/3}}\ S_n(\varepsilon) \quad (eV\ cm^2) \qquad 44$$

➢ Z.B.L Model

In Ziegler. Biersack. Littmark model (Z.B.L), the Thomas-Fermi screening function is replaced by the universal screening function Φ(x) [58-60], the results obtained using this universal potential are more accurate (see figure below).

The reduced energy of Z.B.L is [61]:

$$\varepsilon = \frac{m_t}{m_p + m_t}\frac{a_u}{Z_1 Z_2 e^2} E_0\ (keV),\ a_u = \frac{0.8853\ a_0}{Z_1{}^{0.23} + Z_2{}^{0.23}}$$

This equation become: $\varepsilon = 32.53\ \frac{m_t}{(m_p + m_t) Z_1 Z_2 (Z_1{}^{0.23} + Z_2{}^{0.23})} E_0\ (keV)$

The nuclear stopping cross-section $S_n(E)$ of an ion with energy E_0 in the laboratory frame where the target atom is at rest (i.e., no recoil) is given by [62, 63]:

$$S_n(E) = 8.462 \times 10^{-15} \frac{Z_1 Z_2 m_p}{(m_p + m_t) Z_1 Z_2 (Z_1^{0.23} + Z_2^{0.23})} \; S_n(\varepsilon) \qquad (\text{eV cm}^2) \qquad (45)$$

From **Fig.2.6**, we can observe that:

- For $\varepsilon < 10$, the shape of the nuclear stopping cross-section $S_n(\varepsilon)$ varies depending on the model used.
- For $\varepsilon > 10$, the shape is identical for all the proposed models.

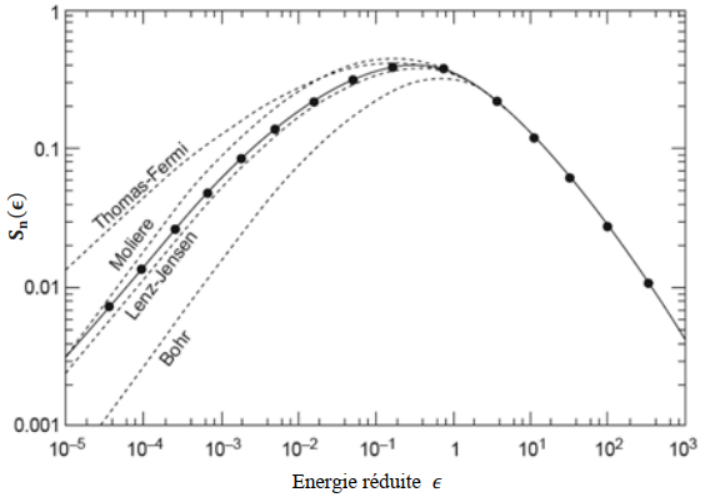

***Figure.2.6**: Nuclear stopping cross-sections calculated by the classical models [62].*

II.3.1.2 Estimation of the electronic stopping power

The process of electronic stopping occurs when a high-energy ion traverses through a material, releasing its energy to the target electrons. The process of transferring the ion's kinetic energy to the target electrons is a complicated one compared to the nuclear stopping discussed in the previous section, because it originates from different processes. These mechanisms involve the direct transfer of kinetic energy to electrons through electron-electron collisions, excitation or ionization of target atoms, excitation of conduction electrons, and ionization or electron-capture by the ion itself [64]. Due to the complexity of these processes, it is challenging to encapsulate electronic energy loss within a singular theoretical framework. Consequently, various models are employed to elucidate this phenomenon across different ion energy regimes. Typically, these energies are partitioned into three segments, delineated by comparing the ion's velocity with the Bohr velocity, expressed as $v_0 = e^2/\hbar$, where e represents the electron charge and ħ signifies Planck's constant respectively. According to this theory, a hydrogen atom at 25 keV moves with the same velocity as its orbital electron, while

helium moves with the same velocity as its orbital electrons at 252 keV. Therefore, the initial energy of the ion with a velocity equal to the orbital velocity can be expressed as a function of the ion's mass and atomic number.

$$E = Z_1^{4/3} A_1 25 \text{ keV}$$

where Z_1 and A_1 are ion' s atomic number and mass number respectively.

➢ Low-velocity electronic stopping

At relatively low incident energies ($E \leq 1$ MeV for He^+), the electronic stopping power varies directly with the particle velocity. This phenomenon, known as the Lindhard-Scharff (LS) regime, applies when considering a projectile velocity v_1 [65, 66].

$$v_1 \leq Z_1^{2/3} v_0$$

In the LS regime, the electronic stopping power and the cross section are written respectively as [13]:

$$\left.\frac{dE}{dx}\right|_e = 231.6\ \rho\ {Z_1}^{1/6} \frac{Z_1 Z_2}{\left({Z_1}^{2/3} + {Z_2}^{2/3}\right)^{3/2} m_t \sqrt{m_p}} \quad \sqrt{E(keV)} = k_e \sqrt{E(keV)}$$

Where k_e is a constant which depend on the collision partners.

$$S_e(E) \approx 3.846 \times 10^{-15} {Z_1}^{1/6} \frac{Z_1 Z_2}{\left({Z_1}^{2/3} + {Z_2}^{2/3}\right)^{3/2}} \sqrt{\frac{E(keV)}{m_p}} \qquad (eV\ cm^2) \quad 46$$

➢ High-velocity electronic stopping

Different concepts of the theoretical description of electronic stopping at high ion velocities $v_1 \leq Z_1^{2/3} v_0$, have been developed by numerous authors. A comprehensive review is given in Sigmund's books [67, 68]. In this region, the ion is completely stripped of its electrons. The degree of energy loss is directly proportional to Z_1^2, as established by Bethe and Bloch. Hence, this area is commonly known as the Bethe-Bloch region (see **Fig.2.5**). The electronic stopping

power in this region is determined by the Bethe-Bloch equation [69-72] (in which the corrections regarding relativistic velocity and electronic structure is absent [62]:

$$S_e(E) = \frac{4\pi e^4 {Z_1}^2 Z_2}{m_e v^2} \ln\left(\frac{2m_2 v^2}{I}\right)$$

And the electronic stopping power is written as [18]:

$$\left.\frac{dE}{dx}\right|_e = NS_e(E) = \frac{4\pi e^4 {Z_1}^2 NZ_2}{m_e v^2} \ln\left(\frac{2m_2 v^2}{I}\right) \quad 47$$

where NZ_2 is the electron density of the target, m_e is the mass of the electron, and I is the mean ionization potential (approximately $\frac{I}{Z_2} = 10eV$).

- **Intermediate velocity electronic stopping**

In this case, the intermediate region is situated between region 1 and region 2 where $v_1 \approx {Z_1}^{2/3} v_0$. In this domain, the projectile ion is no longer fully stripped: it captures electrons from the target, reducing its charge state. Its average charge becomes lower than $Z_1 e$, and thus the electronic stopping power becomes weaker than predicted by the Bethe formula. The validity domain of the latter can then be extended by introducing an effective charge ${Z_1}^*$. Thus, at intermediate velocities, due to the antagonistic effects between the variation of velocity and the effective charge ${Z_1}^*$, the energy deposition reaches a maximum, called the Bragg peak, and eventually the electronic stopping power reaches its maximum and decreases as the ion energy decreases.

II.4 Energy loss in compound

The previously discussed energy loss pertains to targets composed of a single element. However, the energy loss in targets composed of multiple elements, referred to as compounds, has not yet been addressed. If the target is a compound $A_m B_n$ consisting of two distinct elements A and B, then the total stopping power of an ion passing through it can be determined using a straightforward additive rule. This rule is based under the assumption that the interaction between ions and component target are independent of the surrounding target atoms.

Thus, if the stopping cross sections of element A and B are denoted as ε^{A} and ε^{B} respectively, the total stopping cross section can be expressed as:

$$\varepsilon^{A_m B_n} = m\varepsilon^{A_m} + n\varepsilon^{B_n} \quad 48$$

Where m and n represent the relative molar fractions of the compound materials. Equation above, known as Bragg's rule [73], provides a theoretical framework. However, experimental the energy loss findings indicate slight deviations from Bragg's rule due to the chemical and physical states of the material. For instance, experimental results show deviations of approximately 10% - 20% from Bragg's rule for the stopping maximum in light gases and solid compounds containing heavier elements [60, 64]. These deviations led to the development of a corrective model accounting for the chemical state of the compound, known as the core and bonds model (CAB) [64]. The CAB model estimates the stopping power of compounds based on measured values from 114 organic compounds. In this model, each molecule is described as a collection of atomic cores and bonds, corresponding to non-bonding core and bonding valence electrons, respectively. Ziegler et al. [64] also applied this model to calculate stopping cross sections for some inorganic compounds.

II.5 Energy straggling

As an energetic ion traverses a substrate, it dissipates its energy through numerous interactions with the target atoms, resulting in statistically fluctuating interactions. Consequently, ions with identical initial energies do not retain the same energy levels after passing through a thickness **x** of the same medium. Therefore, the energy loss ΔE is subject to fluctuations. The ions, having an energy loss ΔE due to the stopping powers of the material, also spread to $\delta\Delta E$, resulting from statistical fluctuations in nuclear energy loss and electronic energy loss. This discrete behavior of energy loss processes, leading to uncertainty in energy or energy spread, is termed nuclear straggling, as illustrated in **Fig.2.7**.

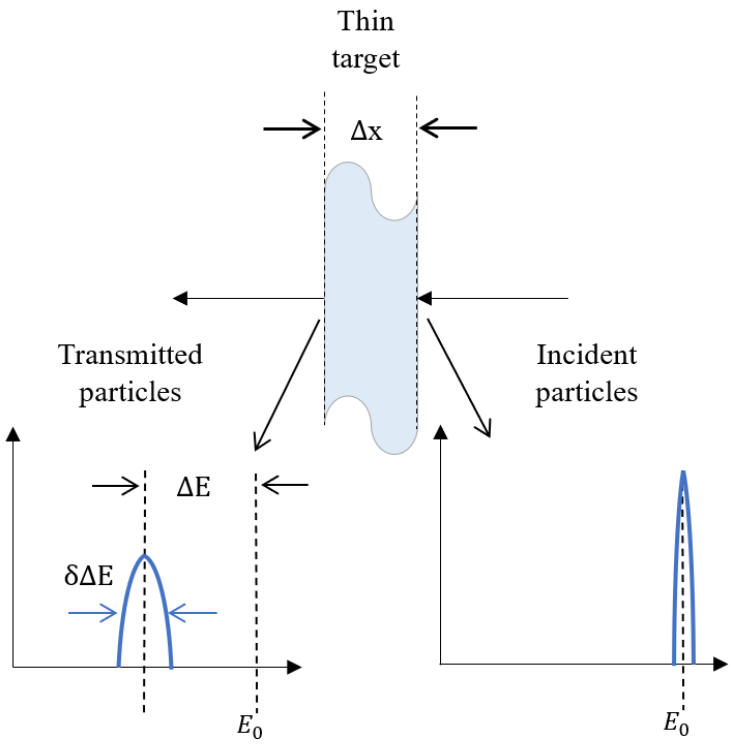

***Figure.2.7**: A monoenergetic beam of energy E_0 loses energy ΔE in penetrating a thin film of Δx.*

The statistical fluctuations of the nuclear energy loss Q_n^2 are calculated in a similar method to that described for nuclear stopping discussed in section II.3.1 as detailed in [60]:

$$Q_n^2 = \int_0^\infty T^2 d\sigma = 16\pi Z_1^2 Z_2^2 e^4 \frac{M_1^2}{(M_1 + M_2)^2} F_n \qquad 49$$

Where,

$$F_n(\varepsilon) = \frac{1}{4 + 0.197\varepsilon^{-1.6991} + 6.584\varepsilon^{-1.0494}}$$

$$\varepsilon = \frac{M_2\, a}{(M_1 + M_2) Z_1 Z_2 e^2} E \qquad 50$$

From the above equations, as E tends to infinity then e tends also to infinity resulting in Fn = 0.25. The maximum of nuclear energy loss tends to:

$$Q_n^2 = 4\pi Z_1^2 Z_2^2 e^4 \frac{M_1^2}{(M_1 + M_2)^2} \qquad 51$$

This outcome indicates that for high-energy projectiles, the significance of Q_n^2 became negligible as it approaches a constant value.

The straggling of electronic energy loss is deduced from the Bethe-Bloch equation [102]. By employing the assumption of a point charge with high velocity, the subsequent equation has been derived [64]:

$$\Omega_B^2 = 4\pi Z_1^2 Z_2 e^4 N\Delta x \qquad 52$$

Where Ω_B^2, is known as Bohr straggling, which quantifies the variance of the average energy loss experienced by a projectile after traversing a medium of thickness Δx, where Ω_B denotes the standard deviation. Consequently, the full width at half maximum of the energy loss distribution is expressed as $FWHM_B = 2\Omega_B\sqrt{2\ln 2}$. Bohr's assumption of a point charge has been extended by Lindhard et al., who introduced a correction term for energies where this assumption may not hold valid [74]. As an example, for light ions such as hydrogen, the nuclear straggling can roughly be neglected, whereas it is dominant for heavy ions such as germanium (see **Fig.2.8).**

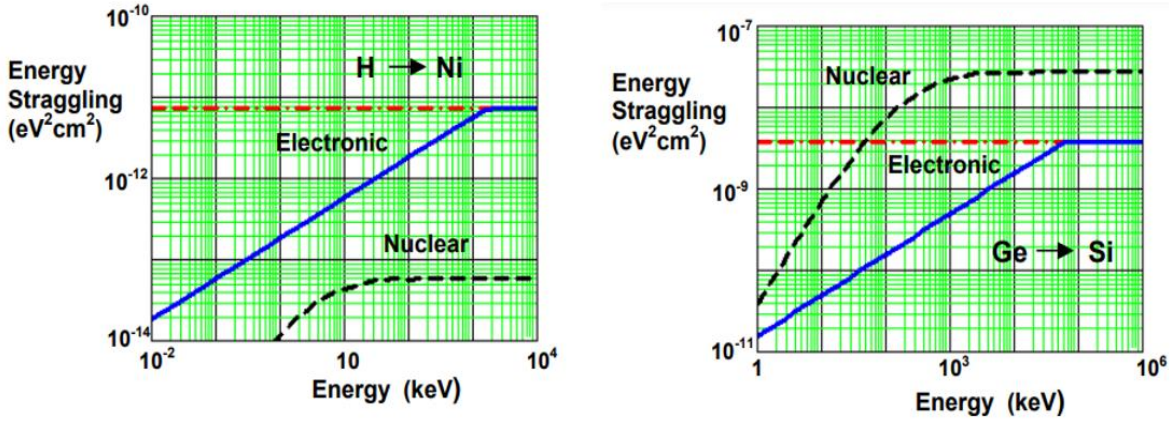

***Figure.2.8**: Energy straggling Ω_B^2 for hydrogen in nickel and for germanium ions in silicon.*

II.6 Range and range straggling

When an energetic ion traverses a material, it undergoes energy loss via both nuclear and electronic processes until it comes to rest. The statistical fluctuations in these energy loss mechanisms, combined with multiple scattering events with target atoms, result in a zigzagging trajectory for the ion. These statistical fluctuations lead ions with identical energies to be implanted at varying depths within the material. The cumulative distance travelled by the ion from the surface to its stopping point is termed the total range or just the range and is calculated by considering the stopping cross sections (Eq39). The variation in range due to energy

fluctuations is termed range straggling. Accounting for all these factors, the total range is expressed as $R_{tot} = \sum l_i$, where l_i represents the different paths taken by ions inside the target (see **Fig.2.9**). This figure illustrates two charged particles penetrate a material: one with low incident energy and the other with high incident energy. The ion with high incident energy initially follows an almost straight path due to electronic stopping, but towards the end, it exhibits a zigzag trajectory due to nuclear stopping. Conversely, the lower incident energy ion follows a zigzag path throughout, as nuclear, and electronic stopping forces are of similar magnitudes. The latter ion takes a shorter path due to its lower energy and frequent deflections. The projected range R_p is defined as the average penetration depth from the target surface to the ion's stopping point (measured parallel to the incident direction), while the perpendicular range $R_\perp$ is measured perpendicular to the incident ion's direction. The total range is always longer than other ranges because it considers all the ion implanted paths taken inside the material.

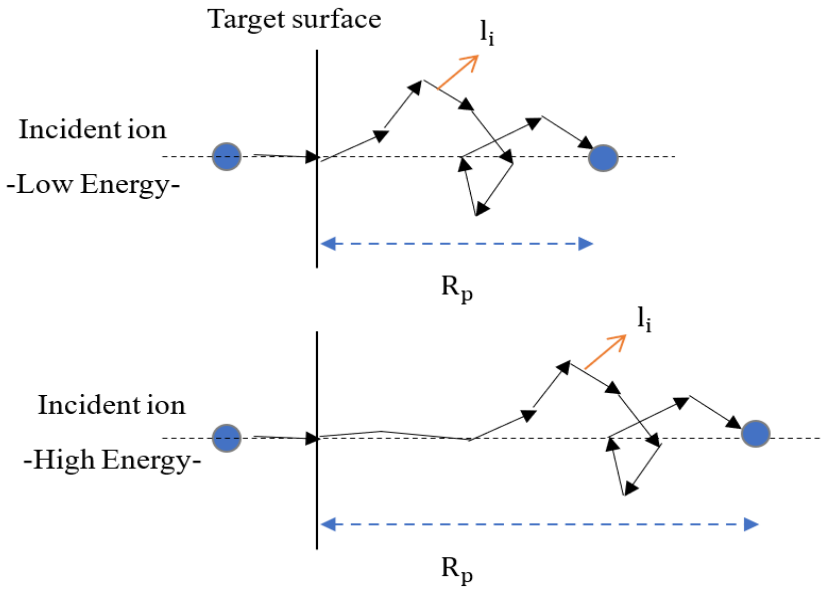

Figure.2.9: *Range concepts for incident ions with low (top figure) and high (bottom figure) energies in target material.*

The gradual increase of the ion beam diameter within a sample (as it passes into a sample), attributed to the multiple scattering of ions inside the sample, is termed as lateral spread. Simultaneously, the associated increasing distribution in the direction of the ions relative to the initial direction is known as the angular spread. These phenomena can be predicted using multiple scattering theories proposed by Sigmund and Winterbon, as well as Markwick and Sigmund [75, 76]. Both angular and lateral spreads contribute to increased path lengths and

consequently energy fluctuations, particularly when the path length deviates from normal incidence to the surface.

Ions with identical initial incident energies possess varying impact parameters concerning the atoms they encounter, leading them to follow different paths after interacting with the target atoms. This discrepancy influences the number of collisions experienced by the ion as well as the total range. The distribution of the final positions is typically assumed to follow a gaussian distribution, as it is shown in **Fig.2.10** where the projected range (R_p) is illustrated. From range straggling, the full width at half maximum (FWHM) can be calculated using the formula: $\mathrm{FWHM} = 2\sigma\sqrt{2\ln 2}$.

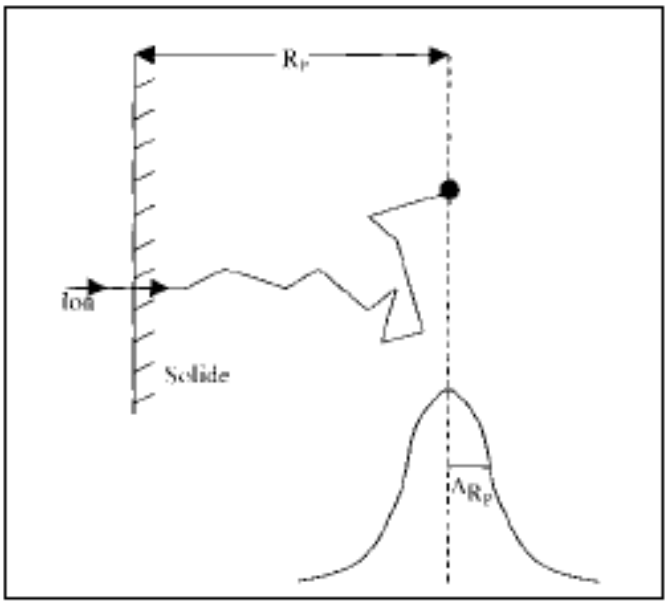

Figure.2.10*: Illustrates the distribution of final implanted ion positions as a function of distance within the material [99]*

III. Effects induced by ion impact

Among the processes resulting from the interaction of atomic ions with solid surfaces, we can mention:

III.1 Sputtering

The phenomenon of sputtering was first observed in the mid-nineteenth century during an electrical discharge in a gas [77]. The authors observed a metallic deposit on the walls of the

discharge tube. Fifty years later, E. Goldstein [78] demonstrated that the origin of this deposit comes from cathodic sputtering induced by the impact of positive ions on the cathode. However, it is only in the last forty years that the scientific community has become interested in understanding the phenomenon, especially the quantity of interest, which is the sputtering yield Y, defined as the number of particles ejected per incident particle.

$$Y = \frac{\text{number of atoms ejected}}{\text{number of incident particles}}$$

According to the transferred energy, target atoms can be ejected from the surface into the vacuum or undergo collisions that can set other atoms within the solid in motion, leading to cascades of collisions. Indeed, atoms resulting from the initial collision, called Primary Knock-On Atoms (PKA), can in turn collide with other atoms of the target, forming Secondary Knock-On Atoms (SKA). We can distinguish three collision regimes as shown in the **Fig.2.11**:

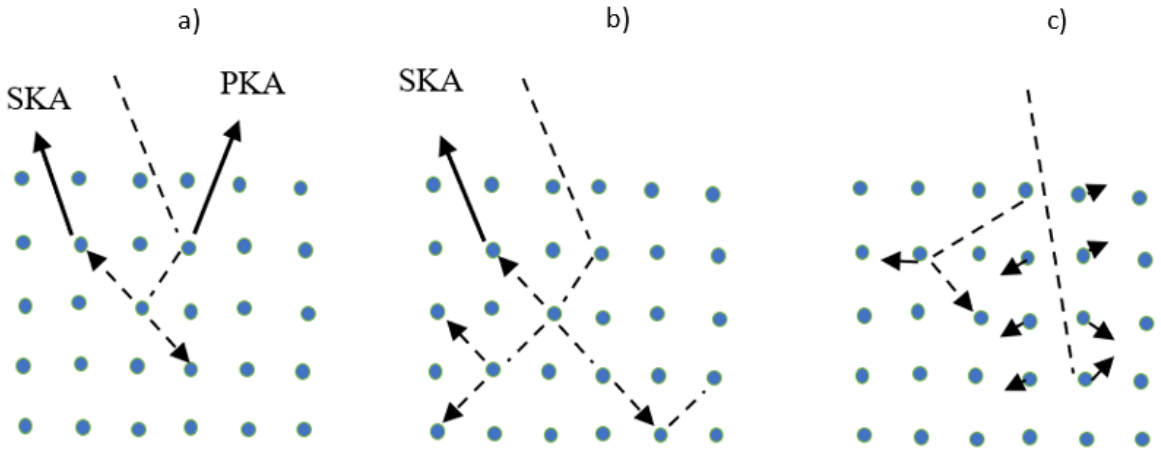

Figure.2.11*: Different sputtering regimes: a) Single collision regime, b) Linear cascade regime, and c) Spike regime [79].*

III.1.1 Single collision regime

The single collision regime is characterized by a low number of sputtered atoms originating from the first or second collision (PKA or SKA). This regime occurs when the projectiles are light, such as H and He [80-82], with energies on the order of a few keV. In this regime, sputtering is induced by very short sequences of collisions that can lead to ejection (see **Fig.2.12**).

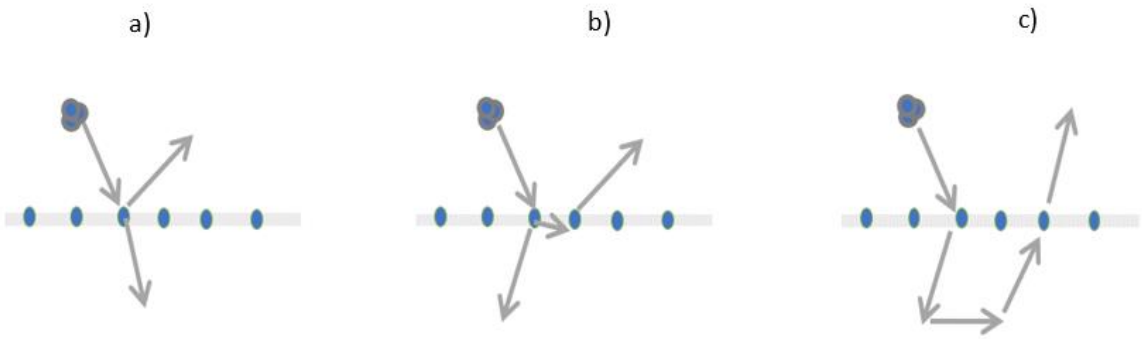

***Figure.2.12**: Single Collision Regime Ejection Mechanisms: a) A primary recoil atom produced during* the initial collision is directly ejected. b) A secondary recoil atom is ejected. c) The projectile undergoes multiple collisions before ejecting an atom from the surface.

Sputtering in this collision regime has been extensively studied through numerical simulations, particularly using codes like TRIM [83] and ACAT (Atomic Collisions in Amorphous Targets) by Y. Yamamura and colleagues [84].

III.1.2 Linear cascade regime

The cascade regime occurs when the energy transfer between the incident ion and the target atoms is sufficient to induce a series of higher-order collisions. These cascades are linear when the density of moving atoms is sufficiently low, and they do not collide with each other. P. Sigmund [85, 86] established and precisely described the theory of linear collision cascades. According to this theory, the (linear) sputtering yield is given by:

$$Y_{lin} = \frac{0.0484\ F_D}{N\lambda_0\ a^2 U} \quad \text{Avec} \begin{cases} a = 0.219\ A,\ \lambda_0 = 24 \\ F_D = \left(\frac{dE}{dx}\right)_n\ \alpha\left(\frac{M_2}{M_1}, \theta, E\right) \end{cases} \qquad 53$$

- F_D : represents the energy deposited per unit length at the surface.
- $\left(\frac{dE}{dx}\right)_n$: represents the nuclear stopping power (loss of nuclear energy).
- α is a dimensionless function of the ratio of the masses of the target atom and the projectile, the angle of incidence θ, and the energy E of the projectile.

According to the author, the mechanisms of sputtering can be divided into three processes:

1. Deceleration and dissipation of the ion's energy,
2. Formation of the collision cascade itself,

3. Transition of atoms from the collision cascade to the surface, where they become sputtered atoms.

III.1.3 Thermal spike regime

When the incident ion transfers high energy densities to the atoms of the medium, all particles within a small volume of the cascade, referred to as the spike, are set in motion. This leads to a local increase in temperature, known as thermal spike [87, 88]. This regime refers to a specific phase in which there is a rapid and localized increase in the density and temperature within a material due to the energy deposition from energetic particles resulting in nonlinear effects. However, is called as well nonlinear cascade regime. The experimental measurements of sputtering yields exhibit nonlinear behaviour for incident particles with energies of around 100 keV, and even higher for heavy ions. These nonlinear effects have been attributed to the thermal spike phenomenon.

III.2 Crater formation

The formation of craters has been demonstrated by several researchers both experimentally and theoretically through molecular dynamics simulations by bombarding with atomic and molecular ions. Indeed, experimentally, the major effect of ion irradiation, in addition to sputtering, is the creation of craters. Studies conducted by Merkle and Jager [89] utilizing Transmission Electron Microscopy (TEM) have highlighted the existence of craters on gold foils with thicknesses ranging from 60 to 80 nm following the impact of Bi and Bi^{2+} ions with energies ranging from 10 to 500 keV (see **Fig.2.13**).

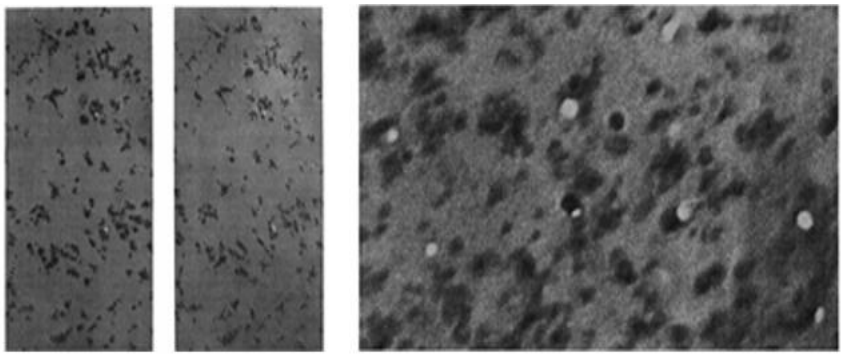

Figure.2.13*: Crater formation due to ion bombardment observed via TEM [89].*

One of the results found in this experiment is the increase in the number of observed craters as a function of the incident energy per atom. Additionally, these authors observed:

- A linear dependence of the number of craters formed with the incident energy in the case of bombardment by the atomic ion Bi^{+}.
- A non-linear dependence in the case of bombardment by the molecular ion Bi^{2+}. They noticed that the threshold for the formation of a visible crater lies near 50 keV for the Bi^{+} ion and 12 keV per atom for the Bi^{2+} molecular ion. This result clearly demonstrates the importance of polyatomic projectiles [101].

In their study of irradiating gold foils with Xenon ions ranging in energy from 50 keV to 400 keV, Donnelly and Birtcher [90, 91] observed the formation of craters on the surface of gold (**Fig.2.14**) like those reported in the case of gold bombarded by Bi and Bi_2 ions [89]. Additionally, these authors noted that approximately 2 to 5% of the Xe^{+} ions produced craters larger than 12 nm in size.

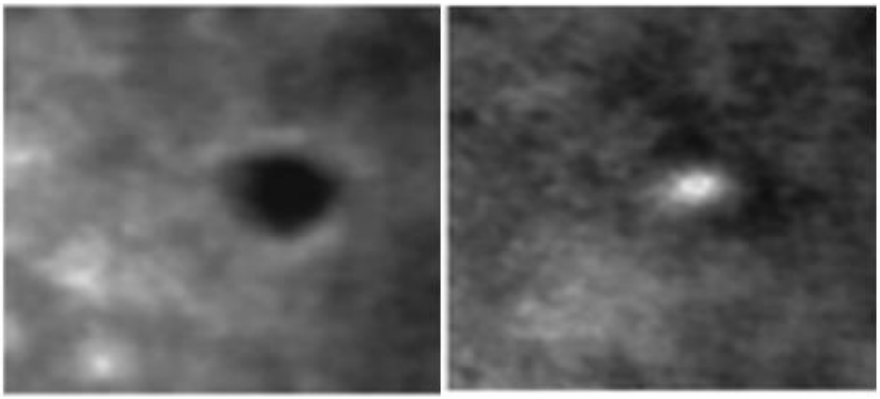

Figure.2.14: *Craters resulting from the impacts of a single Xe ion (left) 400 keV, (right) 50 keV [91].*

A few years later, several authors observed the formation of craters on solid surfaces under the impact of atomic ions using molecular dynamics simulation. Indeed, Thomas J. Colla et al [92] demonstrated the crater formation resulting from sputtering from gold (Au (111)) targets bombarded by gold ions with an energy of 16 keV (see **Fig.2.15**). Later on, Bringa et al. [93-95] investigated this phenomenon by considering the impacts of Xenon on gold with energies ranging from 0.4 to 100 keV. Nordlund et al. [96] observed too craters and they re-examined the relationship between crater size and the properties of both projectiles and target materials. According to these authors, the crater size is inversely proportional to the cohesive energy and the melting temperature of the material.

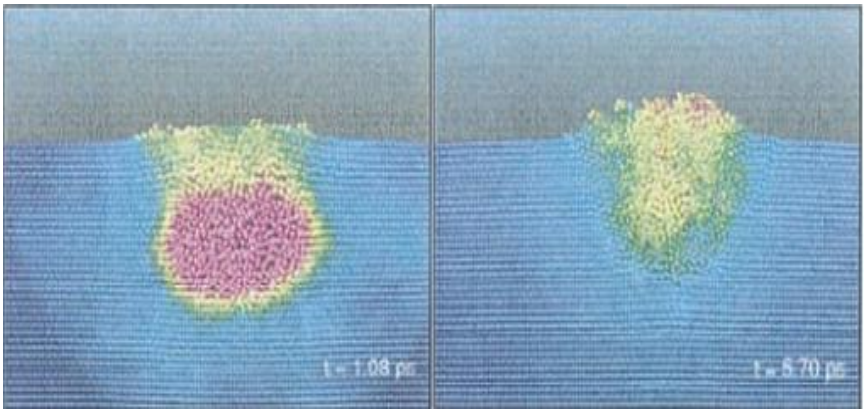

***Figure.2.15**: Crater formation evolution of the impact of gold Au (111) surface by 16 keV gold ions.*

III.3 Ion implantation

One of the collision effects of high-energy atomic ions (MeV) is ion implantation, invented towards the end of the 1950s by William Shockley [97]. Ion implantation is a widely used technique in several fields. It involves introducing ions into a target material to modify its properties. During implantation, various interactions between the implanted ions and the target material occur (**Fig.2.16**).

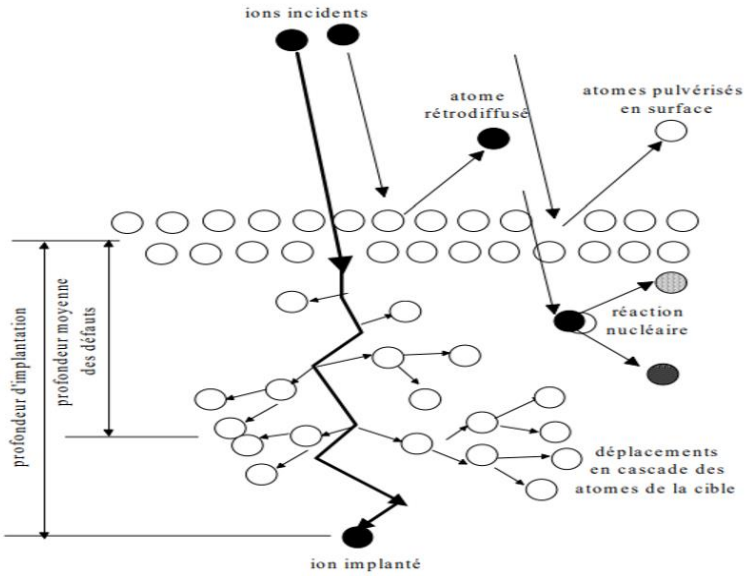

***Figure.2.16**: Different interactions in the target material during atomic ion implantation [98].*

At the beginning of their path in the target material, the implanted ions, due to their high kinetic energy, have an almost straight trajectory. They gradually lose energy by interacting with the electrons of the target material (referred to as inelastic collisions). The ions are implanted at the end of their paths.

Part 2: Ion Beam Analysis

I. Principal IBA techniques

In industries and research institutes, Ion Beam Analysis has been found crucial for elemental materials characterisation which started in the 50s and 60s as the result of the matter discovery and the huge number of available accelerators that time. They are mainly focused on semiconductor technology which is the base for the electronic technology used nowadays. In the beginning of the XXI century, new technological challenges (nanoelectronics devices, more storage, higher speed…) are imposed and new materials beyond classical semiconductors, are emerging (spin tuneable materials, topological insulators, organic semiconductors…). IBA needs to evolve to meet the challenges in analysing some of these new materials. The processes relevant for IBA, which have been outlined in the previous part and are summarized in **Fig.2.17**, are essential for this evolution.

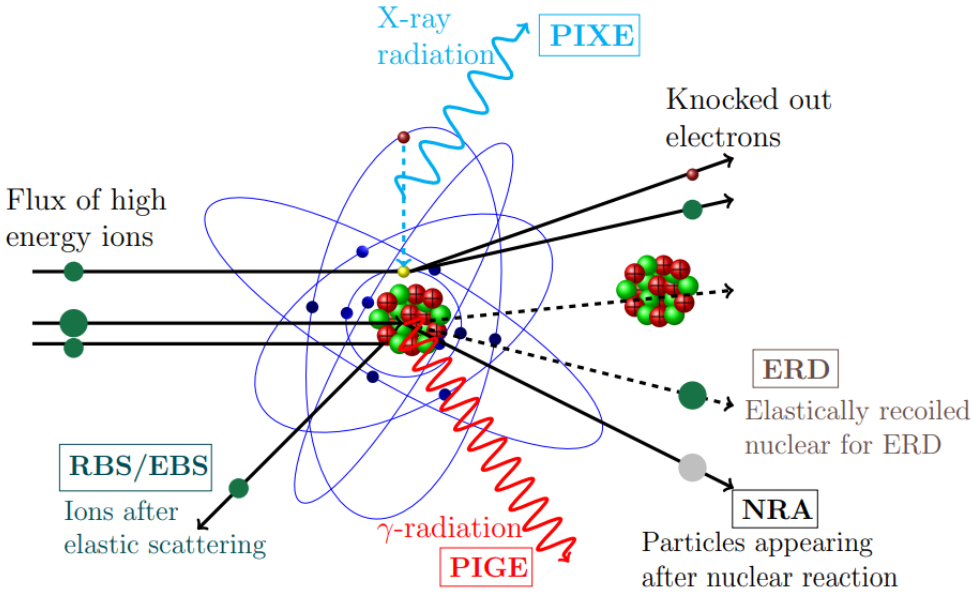

***Figure.2.17**: Schematic of different IBA techniques.*

Among all these IBA techniques that exist, in the present part, we will describe the most commonly used IBA technique starting from:

- Proton Induced Gamma-ray Emission (PIGE) which involves detection and measurement of prompt gamma-rays when energetic charged particles (p, d and α) of energy between (7-10 MeV) are bombarded on the target containing low Z elements from Li to S.

- Nuclear Reaction Analysis (NRA) in which the energetic charged particle beam on hitting the target, initiates nuclear reaction/phenomena with specific isotope of an element present in the sample as analyte,
- Proton Induced X-ray Emission (PIXE) which involves the detection and measurement of radiations (X-rays) induced by the bombardment of beam of energetic charged particles.
- Rutherford Backscattering Spectrometry (RBS) which measure the backscattered incident particles from the target using surface barrier detectors. It is used generally, for quantification as well as elemental depth profiling of heavy elements in a matrix of light elements.

And also, RBS related techniques such as:

- Elastic (non-Rutherford) resonance scattering (EBS) happen when the energetic incident projectile penetrates the Coulomb barrier of the target composed of the formation of compound nucleus in the excited state. The excited compound nucleus can decay by either re-emission of the incident particle or emission of gamma-rays. If it decays by re-emission of incident particle then the phenomena are known as elastic resonance scattering.
- High Resolution (HRBS) which differs from the conventional RBS in that it can provide better energy resolution and depth resolution.
- Ion Channelling RBS
- Micro RBS
- Heavy elements RBS

I.1 Proton induced gamma-ray emission (PIGE)

In the 60s, Sippel and Glover [103] demonstrated for the first time that gamma-rays emitted by energetic protons (of MeV energy) could be utilized to determine the concentrations of Mg and F in geological samples. Later, the energetic deuteron beams were employed by Pierce et al. [104], to determine the carbon concentrations in steel samples. Subsequently, in 1967, 4 MeV proton beam was used by Pierce et his collaborator [105] to quantify Si in various types of steels. The introduction of Germanium-based detectors in the 1970s revolutionized gamma-ray spectrometry. These detectors, such as Ge(Li) and HPGe, offer significantly improved energy

resolution compared to NaI(Tl), enabling PIGE to simultaneously quantify multiple elements in a sample with greater precision. This advancement led to extensive research in the field, exploring applications of both light (e.g., protons and deuterons) and heavy (e.g., tritium, alpha particles, and helium-3) energetic particle beams [106-109] with a focus on enhancing analytical capabilities and expanding the range of detectable elements. Despite its unique applications for low Z elements, the technique PIGE is not fully exploited compared to other IBA techniques, namely RBS and PIXE. PIGE offers distinct advantages over PIXE, particularly in its ability to analyse low Z elements that are challenging to assess using PIXE and other analytical methods. Additionally, PIGE benefits from gamma-ray lines of two neighboring elements or isotopes of the same element being entirely distinct, which eliminates the gamma ray interference or peak overlapping. However, despite these advantages, PIGE remains underutilized in comparison to other IBA techniques.

PIGE Principle

PIGE is known as a nuclear analytical technique that is specific to isotopes and used for determining low Z elements (typically $3 \leq Z \leq 16$) in various types of solid materials using low to medium energy charge particles. it's based on the nuclear reactions occur between an energetic beam particle $(P, d \text{ and } \alpha)$ and sample's nucleus [110]. However, when these reactions occur, the Compound Nucleus (CN) is formed in an excited state and can decay through the emission of particles such as protons and alpha charged particles, neutrons, or gamma-rays [111] (see **Fig.2.18**). These reactions are characterized by the presence of Prompt gamma rays that comes from inelastic scattering $(p, p'\gamma)$ or from nuclear reactions like $(p, \alpha\gamma)$, $(p, n\gamma)$, (p, γ) , $(d, p\gamma)$, $(d, n\gamma)$ and $(\alpha, n\gamma)$. This γ radiation has an energy proportional to the energy difference of the levels between which the transition takes place (see **Fig.2.18**)

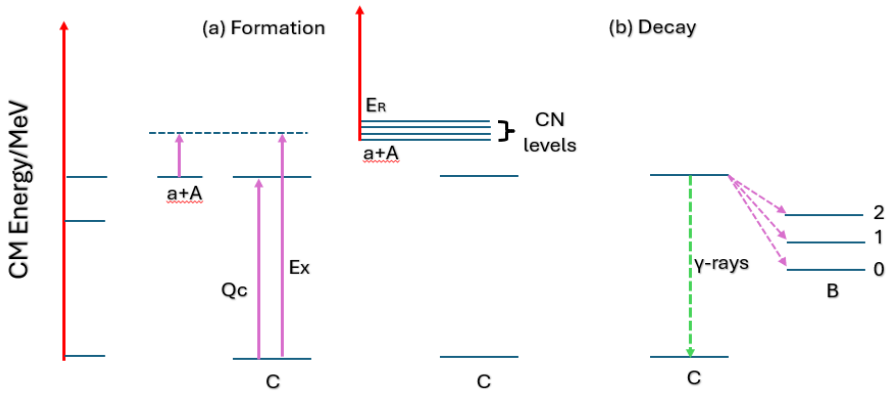

***Figure.2.18**: a) Formation of CN in an excited state, b) CN decay by particle emission from the reaction product (for more details see [110]).*

However, to produce this reaction, the incident particles require an energy greater than must the Coulomb barrier energy (E_c) which is calculated trough the formula below:

$$E_c = \frac{Z_p\, Z_t}{m_p^{\frac{1}{3}} + m_t^{\frac{1}{3}}} \qquad 54$$

where the indices p and t, refer to the projectile and the target.

As an example, a typical PIGE spectrum of soda-lime glass is presented in the **Fig.2.19**

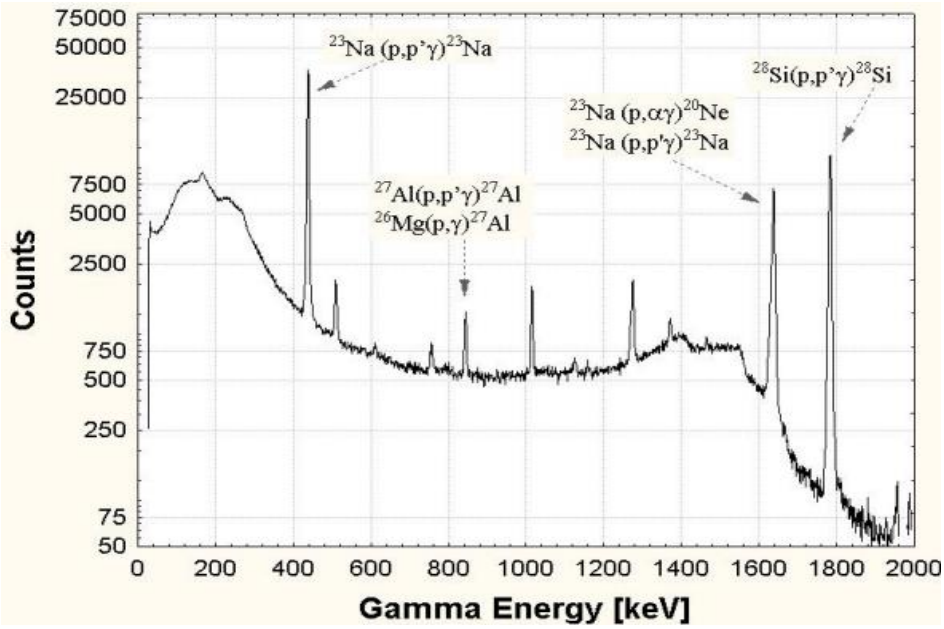

***Figure.2.19**: a typical PIGE spectrum of soda lime glass.*

I.2 Nuclear reaction analysis

The Nuclear Reaction Analysis (NRA) technique focuses on determining the elemental composition of materials by quantifying the reaction products resulting from ion beam-induced reactions. The incident ions must possess sufficient energy to overcome the Coulomb barrier of the target nuclei and interact within the energy range of the attractive nuclear force [112]. As mentioned in the paragraph above the useful estimate of the Coulomb barrier height is provided in [113].

Nuclear reactions principles

Nuclear reactions occur when two particles or nuclei, a_p and A_t, interact to produce b and B. where a_p is the projectile or energetic ion (originating from an accelerator, reactor, or radioactive source),

A_t is a stationary target nucleus, b is the ejected particle (which can be a light nucleus or radiation), and B is the recoil nucleus, typically a heavy nucleus that stops within the bulk target [114].

$$a_p + A_t \rightarrow B + b \qquad 55$$

Analysing the b product provides information about the A_t nuclei in the target, at the same time, it can be quite diverse, since there is a large variety of mechanisms that create different b. One mechanism is a capture reaction, in which the target nucleus captures the incident beam to form a compound nucleus that subsequently decays through γ-emission, for example ^{7}Li(p, γ) ^{8}Be. The second mechanism is when the compound nuclei breaks down in different fragments that can be particles or lighter nuclei, for example ^{7}Li(p, α) ^{4}He. The third mechanism takes place when the target nuclei is excited by absorbing part of the kinetic energy of the impinging particle which is inelastically scattered; the target nuclei de-excites emitting γ-rays, e.g. ^{7}Li(p, p_0) ^{7}Li. The NRA with γ-ray detection is known as particle-induced γ-emission (PIGE) (**Fig.2.17**).

I.3 Proton induced X-ray emission (PIXE)

The PIXE method, is based on the ionization of the inner layers of an atom in the sample during interaction with a beam of charged particles (proton or alpha particle), and the secondary emission of characteristic X-ray radiation from the ionized atom. According to the nature of the beam used, we identify: PIXE, which we will refer to as "conventional" [116], macro-PIXE [117], microprobe PIXE [118], and high-energy PIXE or HE PIXE [119]. As their names indicate, the first is done with a low-energy beam (between 1 and 5 MeV), the second with a millimetre-sized beam ranging from 0.5 to 5 mm, the third with a focused microbeam that can reach the size of a few micrometres and scans the sample to be analysed, and the last with a high-energy beam, of the order of several tens of MeV.

Principle of PIXE

When atoms are bombarded by high-energy particles, an electron from an electronic inner shell is removed leaving a vacancy, another electron from an outer shell fills this vacancy and the quantum of energy, equal to the energy difference between the two shells, is released at the same time either as an x-ray or as an Auger electron. The process continues until the atom has returned to the ground state. X-ray emission analysis is therefore a two-step process of ionisation and emission. X-rays are categorized based on the level from which the original

vacancy arises. For instance, X-rays resulting from transitions from the L, M, N, ... levels to the K level are termed as K_a, K_b, , ... etc (see **Fig.2.20**).

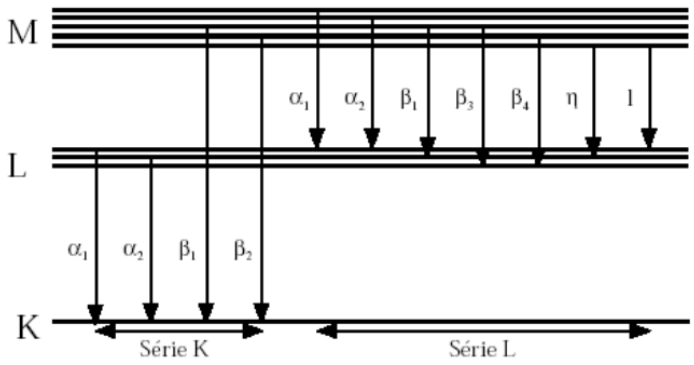

***Figure.2.20**: Transition energy diagram.*

Fig.2.21 illustrates a standard PIXE spectrum obtained from a soil standard sample at the VDG, Ruder Boskovic institute, highlighting the technique's capability to detect multiple elements. The X-ray spectrum exhibits peaks overlaid on a background resulting from various bremsstrahlung processes. Each peak's area corresponds to the concentration of the respective element in the sample. Analysing PIXE spectra is facilitated by the using of software such as GeoPIXE [120] and GUPIX [121]), which provide rapid analysis times on the order of seconds. PIXE demonstrates high sensitivity, achieving maximum sensitivity (-ppm) within two regions of the periodic table ($20 < Z < 35$, $75 < Z < 85$) [122]. Utilizing Si(Li) detectors, PIXE enables multi-elemental analysis to depths of several tens of microns. Microprobes can analyse small samples, referred to as micro-PIXE.

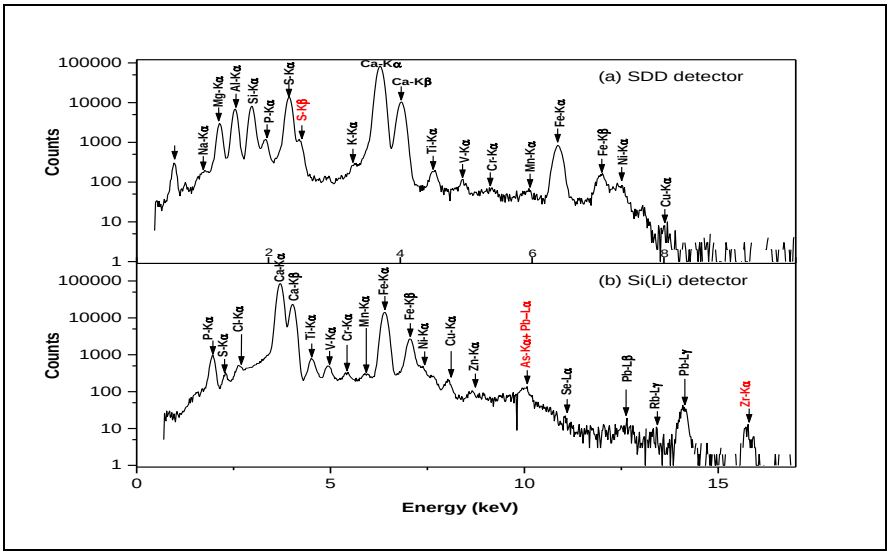

***Figure.2.21:** PIXE spectra of the soil sample taken with (a) SDD and (b) Si(Li) detector induced with 2 MeV protons at Ruder Boskovic Institute.*

I.4 Ion beam induction charge (IBIC)

Contrary to the aforementioned IBA techniques, IBIC measurements do not rely on detecting outgoing reaction products following sample interaction. The ion beam induced charge (IBIC) is considered as a technique of scanning microscopy method that utilizes the charge generated within the sample by the ion beam, and the electronic signal that is created in the output. This method does not rely on detecting of outgoing reaction products after the sample interaction. However, it employs a focused MeV ion beams to achieve low beam currents (~fA) in precisely targeted zones within the sample as probes to measure and image the transport properties of semiconductor materials and devices. Its success is attributed to three main factors: first, the technical availability of laboratories and expertise worldwide that can provide scanning MeV ion beams focused down to submicrometric spots; second, the unique interaction of MeV ions with matter, which allows them to penetrate tens of micrometers with minimal scattering and to excite a high number of free carriers, generating a measurable charge pulse from each incident ion; and third, the existence of a theoretical model that can extract all parameters from the measurements for an exhaustive characterization of the semiconductor. Additionally, the beam can be scanned to generate X-Y maps of the IBIC signals.

IBIC Principle

The principle of IBIC involves the interaction of high-energy ion beams with semiconductor materials. When MeV ions penetrate a semiconductor, they primarily lose energy through ionization processes, generating electron-hole pairs along their paths. This interaction can be divided into several key steps:

a) **Ion penetration and ionization**

As MeV ions enter the semiconductor material, they lose energy through Coulombic interactions with the electrons in the material. This energy loss results in the creation of electron-hole pairs. The number of pairs generated is proportional to the ion's energy.

b) **Charge carrier collection**

The semiconductor device under investigation is typically biased with an electric field. This field separates the electron-hole pairs generated by the ionizing radiation. Electrons are drawn towards the positive electrode, while holes migrate towards the negative electrode. This movement of charge carriers generates a current pulse.

c) **Signal detection**

The current pulse generated by the separated charge carriers is detected by a sensitive charge-sensitive amplifier connected to the electrodes of the semiconductor device. This pulse is then processed to produce a voltage signal proportional to the energy deposited by the ionizing radiation.

d) Data acquisition and analysis

The voltage signal is digitized using an analog-to-digital converter (ADC) within a multi-channel analyzer (MCA). The MCA collects and stores data, typically representing it as a spectrum of counts versus channel number. This spectrum can be analysed to determine the spatial distribution of charge collection efficiency and other properties.

II. Rutherford backscattering spectrometry (RBS)

In the early 20th century, around 1911, Ernest Rutherford proposed the atomic model where dense nuclei were surrounded by electrons. This hypothesis found confirmation through another experiment conducted by two of his students, Geiger and Marsden, in 1913. The measurements from their experiment marked the birth of backscattering spectrometry.

Rutherford backscattering spectrometry (RBS) is a well-established analytical technique which makes use of the accelerators and has becomes the predominant method in the field of ion beam techniques in materials science [123-127]. Its strength lies in its rapid analysis, providing a fully quantitative and non-destructive approach. Beyond determining the composition and thickness of thin films, RBS is also capable of measuring the mass and depth of the target sample, demonstrating excellent resolution for low-mass elements [125,126].

RBS is highly complementary to other surface analysis techniques, such as Auger electron spectroscopy (AES), X-ray fluorescence spectroscopy (XRF), X-ray photoelectron spectroscopy (XPS), secondary ion mass spectrometry (SIMS) [128, 129], and specially Proton induced x-ray emission (PIXE).

RBS relies on the interaction between the ion and target atoms described previously in the 1st part of the current chapter. This technique employs a high-energy ion to investigate the properties of a solid through ion backscattering. The advantages of ion beam analytical methods include their ease of use, non-destructive nature, and the ability to quantitatively interpret

experimental results. RBS finds application across various scientific disciplines, including geology, Industry, mineralogy, biology, and medicine [125].

II.1 Principle

The physical principle underlying Rutherford backscattering spectrometry is relatively straightforward: a monoenergetic ion beam, usually Proton or Helium of typical energy of 0.5 to 2.5 MeV, is directed at a solid sample. However, the incident ions get backscattered into the detector after they interacted with the target`s atoms, i.e. the ion enters the sample, loses energy through inelastic collisions with electrons, scatters on atomic nuclei (losing energy through kinematics), and then travels back out in which the scattering angle may vary from $(0\ to\ 180°)$, losing additional energy through inelastic collisions with electrons, before being detected to show an energy distribution.

II.2 Collisions kinematics:

The interaction between the ion projectile and the target atom can be properly described by the Coulomb repulsion of two-body collisions (simple elastic collision of two isolated particles) when the following two conditions are fulfilled:

1- The projectile energy, denoted as E_0, must significantly exceed the binding energy of the atom in the target. The typical binding energy is on the order of electron volts (eV).
2- The presence of nuclear reactions and resonances must be absent. Nuclear effects using a proton beam may manifest even at energies below 1 MeV, while with Helium beam, these effects start to become noticeable at relatively higher energies (2 to 3 MeV).

Based on the aforementioned assumptions, the collision between the projectile, with a mass of m_p and possesses an incident energy E_0, and the target, having a mass of m_t, is initially at rest, is well described in the 1st part. However, after the elastic collision, there is a transfer of energy from the projectile to the target nucleus. The quantities that play a significant role in determining mass properties and required to analyse the RBS spectra are the kinematics factor K, which is the ratio of the backscattered energy to that of the incident energy, the scattering cross-section, which gives an indication of how the incident particle loses energy as it moves through the target. Thus, the kinematic factor is given by the relation:

$$K = \frac{E_1}{E_0} = \left(\frac{\sqrt{{m_t}^2 - {m_p}^2 \ \sin^2\theta} + M_1 \cos\theta}{m_p + m_t} \right)^2 \quad 56$$

Where the scattering angle θ, is the angle formed between the direction of the incident projectile and the direction in which the scattered particles move.

We noticed that the kinematic factor depends only on the ratio of the projectile to the target masses and on the scattering angle.

According to equation (56), the energy spectra of scattered ions can be interpreted as mass spectra, allowing us to determine the composition of the sample. Therefore, this equation explains how, by measuring the energy E_1 of particles scattered at a known angle θ by the target and knowing the characteristics m_p and E_0 of the incident beam, one can identify the mass (m_t) of the atoms composing the target, i.e. the nature of the target. It is good to note that, for any combination of projectile and target mass, the value K consistently attains its minimum value at 180°. For which the value of the kinematic factor at $\theta = 180°$ $\left[K(\theta = 180°) = \left(\frac{(A-1)}{(1+A)}\right)^2\right]$ is the square of its value at $\theta = 90°$ $\left[K(\theta = 90°) = \frac{(A-1)}{(1+A)}\right]$.

II.3 Cross section

II.3.1 Rutherford scattering

To accurately interpret an RBS spectrum, it's essential to determine how often an elastic collision (scattering event) occurs when incident ions with energy E interact with target atoms in a thin film. This involves determining the number of atoms in the sample by assessing the probability of these interactions. The differential scattering cross-section, $d\sigma/d\Omega$, is a key concept that addresses this probability (see the 1st part). In every RBS experiment, a detector is positioned at a specific angle θ to count each particle scattered into the solid angle covered by the detector. This solid angle is typically very small in RBS setups (less than 10 msr) and can ideally be considered a differential solid angle. More details are presented in the figure below, which schematically represents the differential cross-section concept. If Q is the total number of particles striking the target (fluence) and dQ is the number of particles detected by the small detector, then the differential cross-section is defined as:

$$\frac{\mathrm{d}\sigma}{\mathrm{d}\Omega} = \frac{1}{Nt}\frac{dQ}{Q}\frac{1}{\mathrm{d}\Omega} \qquad 57$$

Where, N present the density volume of target atoms and t its thickness. Therefore, Nt is the areal density in atoms per area.

For Eq(57) to hold, several conditions must be met:

1. The solid angle $d\Omega$ must be small enough to ensure that the scattering angle θ is well defined.
2. The target's thickness t must be sufficiently small so that the energy loss of particles passing through the target is negligible, ensuring that the particle energy remains constant.
3. The fluence Q should be large enough to give a well-defined value for the ratio dQ.

By using the conservation laws, the differential cross-section $d\sigma/_{d\Omega}$ for an elastic collision is given as Rutherford's formula:

$$\frac{\mathrm{d}\sigma}{\mathrm{d}\Omega} = \left(\frac{\mathrm{Z_1 Z_2\, e^2}}{4\,E_{\mathrm{CM}}}\right)^2 \frac{1}{\sin^4\left(\frac{\theta}{2}\right)} \qquad 58$$

This formula is valid for the center of mass reference frame or for an infinitely heavy target in the laboratory frame. The dependence of this formula on the kinetic energy and angle (**Fig.2.22**) gives us valuable information in nuclear physics experiments.

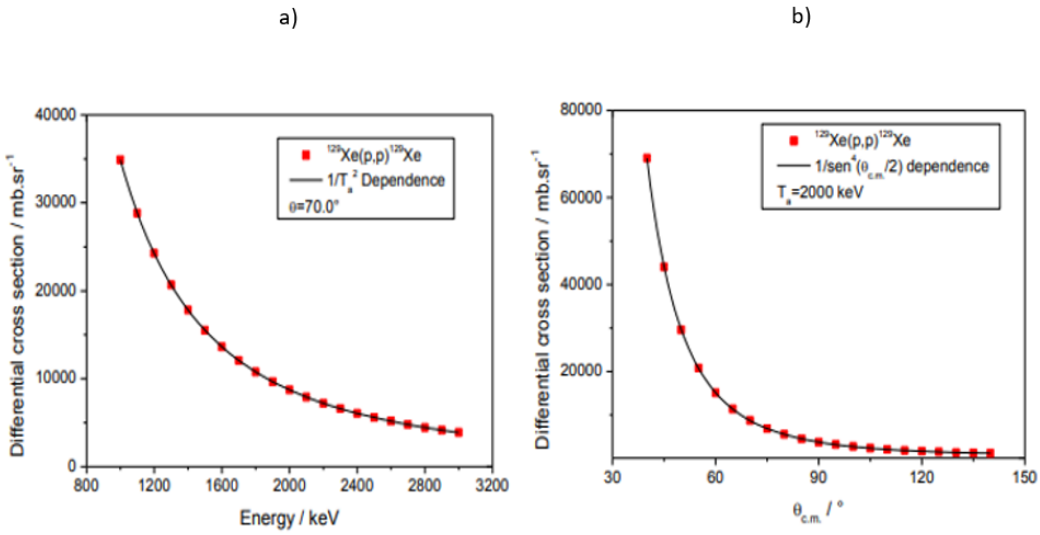

***Figure.2.22**: Rutherford cross section for ^{129}Xe(p,p)^{129}Xe versus a) Energy, b) scattering angle.*

II.3.2 Non-Rutherford scattering (Elastic backscattering spectrometry)

Elastic scattering can be defined as a collision process in which the internal degrees of freedom of the interacting entities play no significant role, and the total kinetic energy of the system remains conserved throughout the interaction. An exemplary instance of elastic scattering is demonstrated by Rutherford scattering, where the Coulombic field of the nucleus governs the interaction. When the distance between the nuclei becomes too small, the nuclear potential starts also to contribute to the collision and shifts from a pure Coulombian process necessarily occur. Consequently, in here, the cross-sections are no longer Rutherford although the interaction may remain elastic, the description of interactions among nucleons involved in nuclear reactions necessitates the application of quantum mechanics by using an optical model. This approach enables a comprehensive understanding of elastic scattering processes and their implications in nuclear physics. Proton backscattering exhibits non-Rutherford behaviour for elements with atomic numbers Z less than or equal to 15 at energies below 2 MeV. Conversely, the cross-sections form ^{4}He remain consistent with the Rutherford model for elements with atomic numbers Z greater than or equal to 6 up to energies of 2 MeV. While High-energy non-Rutherford cross-sections cannot be accurately calculated at present, they must be measured.

Tesmer and Nastasi [130] compiled a series of non-Rutherford cross-section graphs detailing the scattering of protons and ^{4}He by target elements with $Z_2 \leq 20$. However, discrepancies in some of the previous findings were noted by Cheng et al's measurements [131]. Employing a ^{4}He beam with a beam spread of 1.28 keV, Cheng et al. observed that beyond 2.60, 3.20, 3.60, 3.80, and 4.50 MeV, cross-sections deviated from the Rutherford model for F, Mg, Al, Si, and Cl, respectively. Notably, cross-sections for F, Al, and Cl exhibited continuous resonance distributions over the mentioned energy values, whereas Si displayed a single strong narrow isolated resonance at 4.370 MeV ±10 keV (resonance width of 20 keV, σ/σ_R=2.90), and a significantly stronger one at 5.375 MeV ±10 keV (resonance width of 10 keV, σ/σ_R=9.50) [30]. Elastic resonances can substantially enhance cross-sections beyond Rutherford values. Analysts leverage these elastic-scattering resonances, employing the EBS technique, to heighten sensitivity to low-Z elements and enhance accuracy in determining stoichiometric ratios.

II.4 Important parameters of RBS

II.4.1 Multiple and plural scattering

The term plural scattering is normally used to describe trajectories where the ion suffered several (a few) large angle scattering events before being detected. A particular case corresponds to two large angle scattering events called double scattering, while multiple scattering refers to the succession of very many small angle scattering events that each ion undergoes (see **Fig.2.23**).

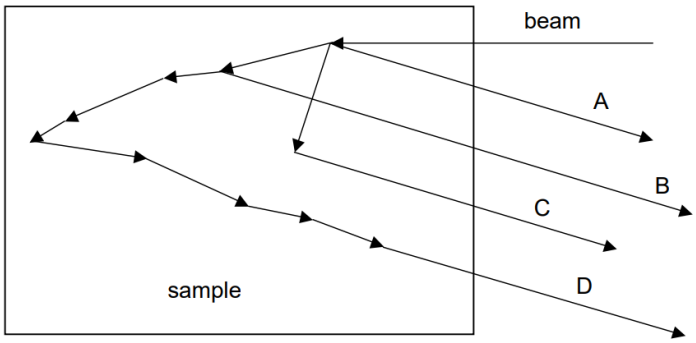

***Figure.2.23**: Schematic representation of ion scattering. (A: Single scattering, B and C: Double scattering, D: Multiple scattering events).*

The differentiation between plural and multiple scattering holds a degree of arbitrariness, as it relies on the definition of "large angle" and "small angle" scattering. However, despite this ambiguity, the distinct effects on experimental spectra are notable, warranting separate theoretical treatments. Plural scattering tends to increase the yield at lower energies and introduces a background signal at these energy levels. Conversely, multiple scattering primarily contributes to energy straggling, adding fluctuations to the energy distribution of particles traversing through a medium. These contrasting effects underscore the importance of discerning between plural and multiple scattering phenomena in both experimental analysis and theoretical modelling.

Recent efforts have been undertaken to discern plural scattering contributions in RBS energy distributions, particularly focusing on the interaction of 0.5 to 1.0 MeV ^{4}He particles with a 100 nm Au layer on Si substrate [1333]. In this study, the SIMNRA code [134] was employed to simulate spectra incorporating double scattering, which were then compared with those generated by a full Monte Carlo simulation. The findings revealed that trajectories involving more than nine scattering events (each with an angle θ>2°) contributed significantly to the spectrum. However, most of these scattering events resulted in minor deflections, each below

10°. The computational time for these simulations averaged approximately ten minutes, rendering them feasible for practical applications. While TRIM offers higher accuracy by considering all collisions, the computational times associated with this method are prohibitively long for routine spectrum analysis. As an example, the **Fig.2.24** shows the importance of the double scattering.

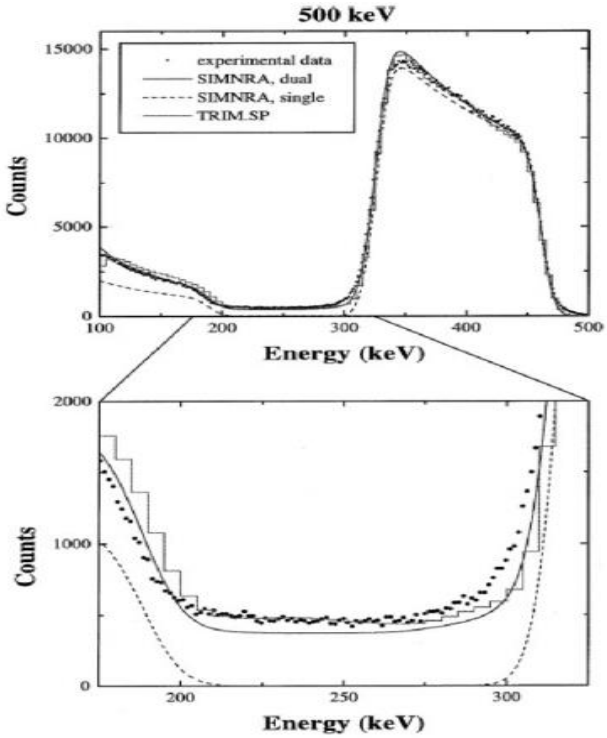

***Fig.2.24**: Double scattering effects in RBS Spectrum of Au on Si at a polar emission angle of 15° for 0.5 MeV 4 He.*

II.4.2 Mass resolution

Another important parameter for this technique is the mass resolution which refers to the ability to distinguish between atoms of different masses. However, using the Eq (55) and (56), the mass resolution can be expressed by the following formula:

$$\frac{\mathrm{m_t}}{\Delta \mathrm{m_t}} = \frac{\mathrm{E}}{\Delta E} \frac{\mathrm{A} + \sin^2\theta - \cos\theta\sqrt{A^2 - \sin^2\theta}}{\mathrm{A}^2 - \sin^2\theta + \cos\theta\sqrt{A^2 - \sin^2\theta}}. \qquad 59$$

Here, ΔE represents the energy separation, which primarily includes contributions from detector resolution, straggling, beam energy spread, and various geometric effects [135]. By

assuming that a constant relative energy resolution of the detector equal to $E/\Delta E = 100$, the mass resolution presented in **Fig.2.25**, shows that it is optimal at large scattering angles.

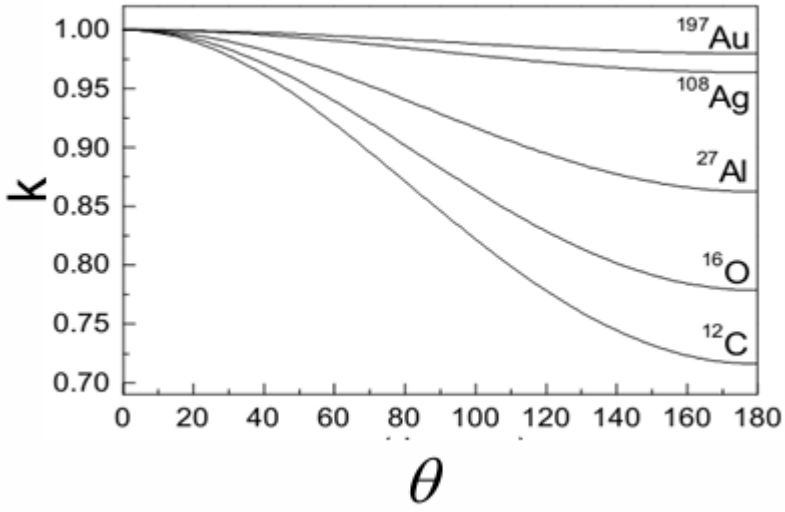

***Figure.2.25**: Mass resolution illustration as function of the scattering angles θ.*

II.4.3 Depth resolution

Depth resolution in Rutherford Backscattering Spectrometry (RBS) is primarily determined by the energy resolution of the system. This resolution is influenced by several factors. Firstly, it is strongly correlated with the stopping power, which measures the energy loss per unit thickness of the material being penetrated. Higher energy loss allows for better discrimination between different material slabs in an RBS energy spectrum. In the energy range of 0.5-1.0 MeV for helium, where the stopping power peaks, depth resolution tends to be optimal. Moreover, heavier materials, characterized by higher atomic numbers (Z), typically exhibit larger stopping powers, leading to enhanced depth resolution.

However, in practical terms, the energy resolution of the system is predominantly dictated by the detector resolution, which typically stands at around 12 keV. This limitation results in depth resolutions typically ranging from 10 to 30 nanometres. While it is possible to improve depth resolution by employing high-resolution detectors, this comes at an increased cost. Alternatively, depth resolution can also be enhanced by utilizing grazing angles during measurement. This approach increases the energy loss experienced by particles as they traverse the material, thereby improving discrimination of slab thicknesses in the final RBS spectrum.

However, it's important to note that employing grazing angles reduces the total depth that can be analysed.

II.4.4 Pile-up

RBS pile-up refers to a phenomenon encountered in Rutherford Backscattering Spectrometry (RBS) where multiple events of backscattering occur within the detection system, leading to overlapping signals in the energy spectrum. This overlap can distort the interpretation of the spectrum, making it challenging to accurately resolve the contributions from individual elements or layers within the sample. RBS pile-up commonly occurs when the count rate of backscattered ions becomes too high, overwhelming the capabilities of the detection system to distinguish between individual events. Strategies to mitigate RBS pile-up include reducing the incident beam intensity, optimizing detector settings, and employing deconvolution algorithms during data analysis. Addressing RBS pile-up is fundamental for ensuring the reliability and accuracy of RBS measurements, particularly in applications requiring precise characterization of materials' elemental composition and depth profiles.

III. RBS related techniques

III.1 High resolution RBS

High-Resolution Rutherford Backscattering Spectrometry (HR-RBS) is an advanced analytical technique used to investigate the compositional and structural properties of materials at the near-surface level with high precision. It differs from the conventional Rutherford Backscattering Spectrometry (RBS), in which it employs enhanced equipment and methodologies to:

- **Energy resolution improvement**: HR-RBS utilizes high-resolution detectors, often silicon-based, capable of detecting small changes in the energy of backscattered particles. This allows for precise measurement of energy loss as particles penetrate the material, leading to improved depth profiling.
- **Grazing incidence and detection angles**: By employing shallow angles of incidence and detection, HR-RBS increases the effective path length of particles within the sample. This results in greater energy loss per unit depth, enhancing the discrimination between closely spaced layers.

- **Enhanced stopping power analysis:** The technique takes advantage of the peak stopping power range of the incident ions, typically helium (He) ions in the energy range of 0.5-1.0 MeV. This maximizes the energy loss per unit thickness, further refining depth resolution.
- **Sensitive detection of low-Z elements:** HR-RBS is particularly effective for detecting and profiling light elements (low-Z elements) in the presence of heavier substrates, due to its high sensitivity and precision.
- **Quantitative and qualitative analysis:** The method provides both qualitative and quantitative information about elemental composition, layer thickness, and interface quality. By analysing the energy spectra of backscattered particles, researchers can determine the concentration and distribution of elements within the sample.
- **Applications in thin films and nanostructures:** HR-RBS is widely used in the characterization of thin films, nanostructures, and semiconductor devices. It is essential for applications requiring detailed depth profiles, such as the analysis of doping profiles in semiconductors or the investigation of diffusion processes in layered materials.

As all IBA techniques, HR-RBS provides comprehensive quantitative and qualitative information about elemental composition, layer thickness, and interface quality, facilitating in-depth understanding of material properties. Moreover, its non-destructive nature allows for sample analysis without significant alteration, preserving sample integrity for further examination. However, HR-RBS is not without limitations. The high cost of equipment, including high-resolution detectors and precise instrumentation, can limit its accessibility to well-funded research facilities. Additionally, the complex data generated by HR-RBS require sophisticated analysis techniques and software, posing challenges for data interpretation and processing. Despite these limitations, the advantages of HR-RBS make it an indispensable tool for researchers seeking to unravel the complexities of surface structures in nanotechnology and surface science.

III.2 Ion channelling RBS

The next IBA RBS configuration is Channelling, which refers to the passage of a particle beam (particles travelling in parallel) through open spaces in materials (i.e. crystal planar and axial channels or possibly nanotubes). Conventionally, this process is studied in single crystals where a variety of channels, both with similar and very different geometric and electronic structures,

are available. Ion channelling and a related technique such as channelling contrast microscopy (CCM), are used to study crystalline material surfaces, lattice order and non-ionising ion damage and specially to measure depth and lateral distribution of defects in crystals. In here, the sample holder is installed on a goniometer in order to align the ion beam with an axis or plane of a monocrystalline material (see **Fig.2.26**).

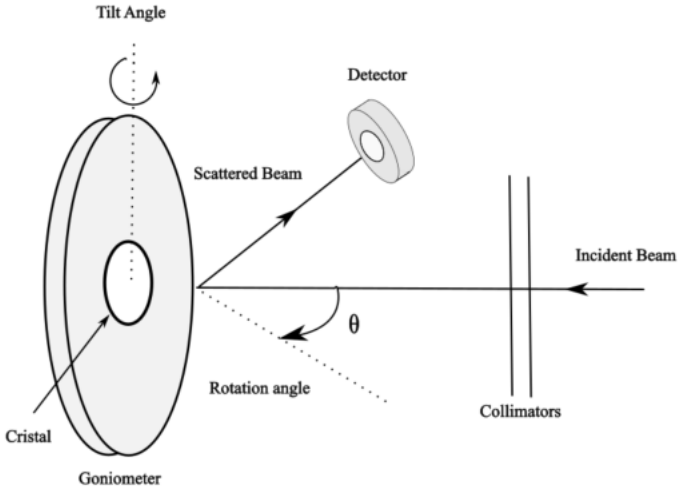

***Figure.2.26**: Channelling geometry.*

The backscattering yield from the atoms in a disordered or damaged region will give rise to a damage feature in the channelling spectrum [136, 137], see **Fig.2.27**.

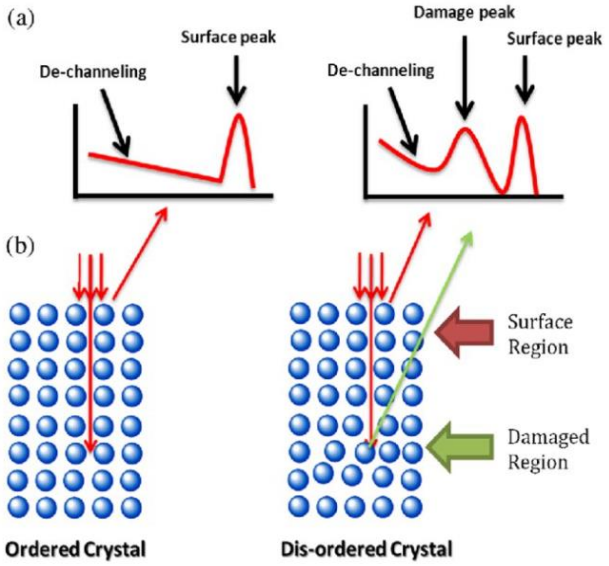

***Figure.2.27**: Schematic representation of RBS spectra of channelling scattering mechanisms in ordered and disordered single crystals.*

As an example, the backscattering yield [138], of channelling and random for 1000 coulomb sample are presented below (**Fig.2.28**).

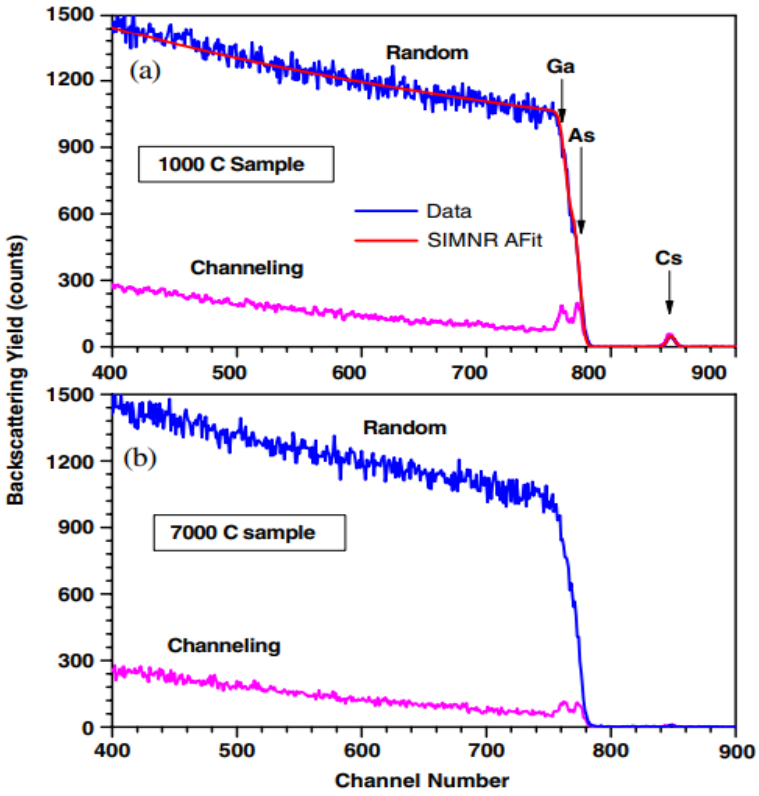

***Figure.2.28**: Comparison of channelling and random RBS spectra.*

III.3 Heavy ion beam RBS

Heavy element Rutherford Backscattering Spectrometry (RBS) provides numerous benefits for material analysis, particularly in the detection of heavy elements within substrates. One significant advantage is its high sensitivity, especially in measuring trace heavy elements within lighter substrate matrices. This sensitivity is critical for various applications, such as semiconductor research and thin film analysis, where precise identification of heavy dopants like platinum or gold in silicon is vital for enhancing device performance. As shown in **Fig. 2.29**, the Rutherford backscattering cross section varies for different probing beams (H, He, Li, C, O, Si). Interestingly, the cross section can increase by up to three orders of magnitude when using a silicon beam instead of a helium beam.

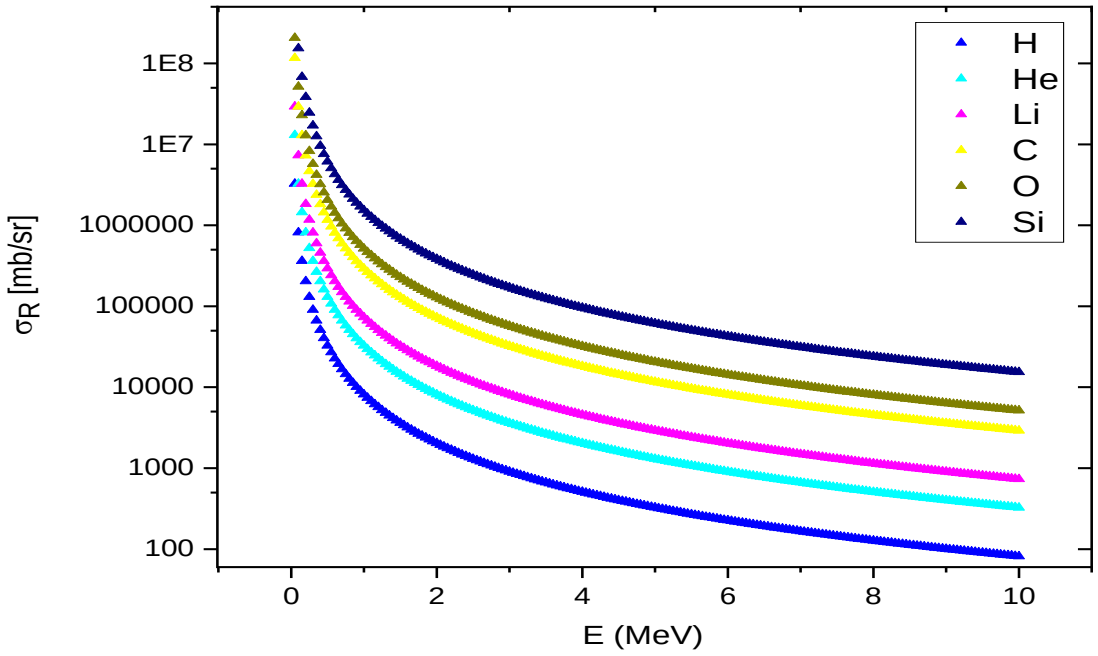

***Figure.2.29**. Rutherford backscattering cross-section for different probing beam on Pt in function of the energy.*

III.4 Micro RBS

Micro Rutherford Backscattering Spectrometry (μRBS) is a specialized form RBS that uses focused ion beams to achieve high spatial resolution. Unlike traditional RBS, which offers a millimeter-scale resolution, μRBS can analyze areas on the micron scale, making it an invaluable tool for materials science, particularly in the study of heterogeneous and microstructured materials.

μRBS is a refinement of the standard RBS technique. It involves focusing the ion beam to a micron-sized spot, allowing for high-resolution mapping of elemental distributions. μRBS is particularly effective in characterizing materials with complex microstructures, such as layered semiconductors, nanomaterials, and microelectronic devices. The focused microbeam enables the analysis of specific areas within a heterogeneous sample, providing detailed information on composition and thickness at the micron scale.

III.4.1 Microbeam spatial resolution

Microbeam spatial resolution refers to the smallest feature size that can be resolved or distinguished in a sample using a focused ion beam in μRBS. It is a measure of the technique's ability to analyze and characterize materials at a fine spatial scale. High spatial resolution is critical for applications requiring detailed analysis of micro-structured materials, such as thin films, microelectronics, nanomaterials, and biological tissues. Regular calibration using known standards is necessary to optimize the spatial resolution. The use of test samples with known microstructures can help in adjusting the beam focusing and detector setup to achieve the best possible resolution. The spatial resolution can be affected by several factors:

1. **Beam focusing:**

The resolution in μRBS is directly influenced by how finely the ion beam can be focused. The use of advanced microbeam optics, such as magnetic quadrupole lenses or electrostatic lenses, helps in narrowing down the beam to a spot size as small as a few micrometers or even sub-micrometer levels.

2. **Ion source characteristics:**

The type of ion source and its properties, such as the initial beam divergence and energy spread, play a pivotal role. An ion source that produces a highly collimated and monoenergetic beam is ideal for achieving better spatial resolution.

3. **Beam stability and alignment:**

Precise control over the beam's alignment and stability is crucial to maintaining high spatial resolution. Any drift or instability in the beam can lead to a blurred or smeared analysis area, reducing the effectiveness of spatial resolution.

4. **Detector configuration and positioning:**

The choice and positioning of detectors relative to the sample and beam path affect the spatial resolution. Detectors need to be placed optimally to ensure accurate detection of backscattered ions from the focused beam area.

III.4.2 Beam brightness

Beam brightness in the context of μRBS refers to the density of ions in the beam per unit area per unit solid angle. It is a measure of how concentrated and intense the ion beam is, which directly impacts the technique's sensitivity and resolution. The brightness can be expressed as following[141]:

$$B = \frac{I}{A_o \left(\frac{A_a}{D^2}\right) E} \qquad 60$$

Where B is the brightness (pA/(μm^{2}mrad^2 MeV)), A_o is the area of the object slit (μm^2), A_a is the area of aperture slit, defining the beam divergence (mm^2), I is the current on the specimen located in the microprobe chamber (pA), D is the distance from the object to the aperture slits (m) and E is the beam energy (MeV).

A beam with a high brightness is the basic requirement for running an ion microprobe with μm beam focus in order to fill the small transversal phase space volume that is accepted by a usual ion microprobe (acceptance) with enough ion current I for the desired application[142].

A brighter beam improves the Signal-to-Noise Ratio, which is necessary for detecting low concentrations of elements and achieving precise quantitative analysis. Higher brightness results in more backscattered ions being detected, providing clearer and more distinct signals. Also, increased beam brightness contributes to enhanced spatial resolution and sensitivity in μRBS. It allows for more accurate depth profiling and elemental analysis, especially in samples with complex or layered structures.

IV. RBS experimental setup

The backscattered alpha particles are detected by a silicon surface barrier detector operating with a bias of 40 to 60 V. The detector generates a charge signal proportional to the energy of the backscattered particles, which is then sent to a pre-amplifier. In the pre-amplifier, this charge signal is converted into a voltage signal proportional to the energy of the backscattered particles. This voltage signal is then amplified and digitized by an analog-to-digital converter (ADC) within the multi-channel analyser (MCA). The digitized data, representing a spectrum of counts versus channel number, is stored on a computer connected to the MCA (see **Fig.2.30**).

Using the computer, alongside the RBS and RBS-C spectrum, the counts of backscattered ions as a function of channel number are monitored in real-time and saved. The sample's position is fixed, but in the case of Channelling, the sample orientation can be adjusted using a goniometer.

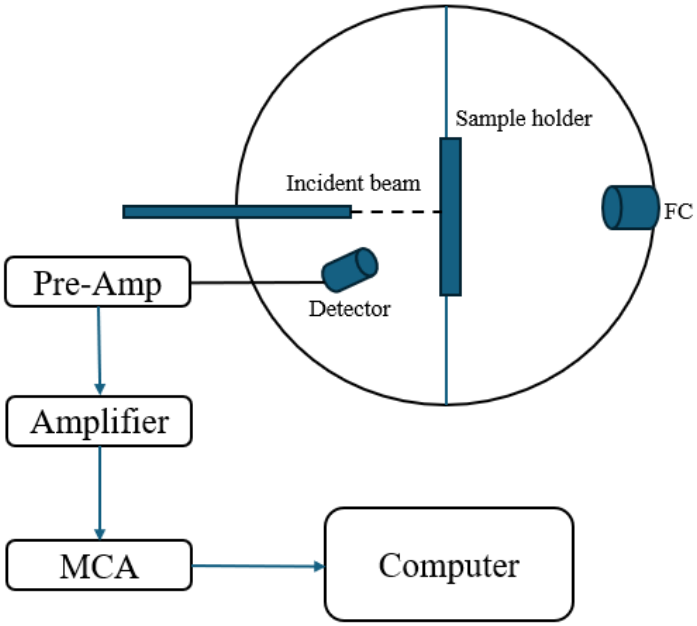

***Figure.2.30**: Side view of scattering chamber and detection system.*

Chapter 3

Measurement of Pt Depth Profile with very Low Concentration in Silicon

Introduction

In this chapter, we outline the strategy for accomplishing the primary objective of the thesis project. It begins with an introduction of the laboratory, then a detailed description of the achievable detection limits within existing laboratory setting. Following this, we conducted an analysis of the probing beam properties to enhance measurement precision, references standards employed to assess the accuracy of the measurement system. Finally, the measurements of the Pt depth profile are provided and compared with simulation profile.

I. Instrumentation and Experimental Facility Overview

The thesis work was carried out at ion beam interaction laboratory at Ruder Boskovic Institute (RBI) in Croatia, the largest multidisciplinary research center, excelling in fundamental sciences, applied research, and advanced education.

The ion beam interaction laboratory at RBI houses two electrostatic accelerators: a 6 MV Tandem Van de Graaff accelerator and a 1 MV Tandetron accelerator **Fig.3.1** shows a real picture of both accelerators.

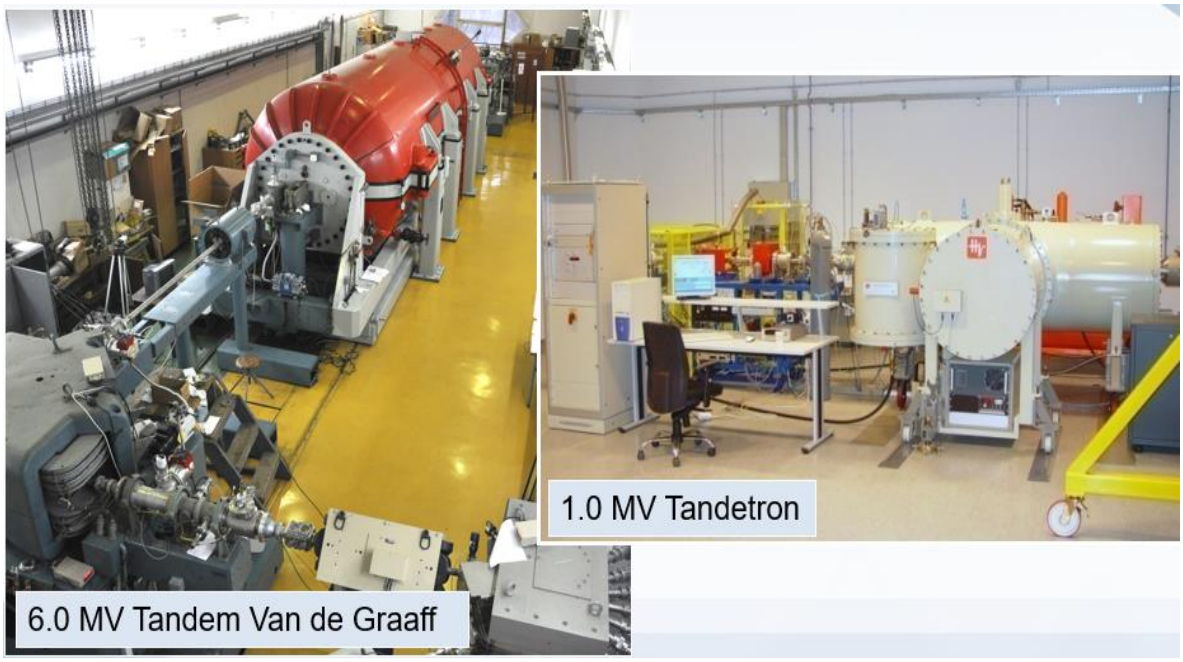

Figure.3.1: *6 MV VdG Tandem and 1 MV Tandetron accelerators at ion beam interaction Laboratory.*

The primary distinction between Tandem and Tandetron accelerators lies in their high voltage generation methods. The Van de Graaff (VdG) Tandem operates by mechanically transporting electrical charges from a power supply to the terminal voltage through a rotating belt, whereas

the Tandetron utilizes a Cockcroft-Walton generator. This gives the Tandetron an edge in stability and reduces terminal ripples.

The foundation of this facility dates back to 1987 when the 6.0 MV EN Tandem Van de Graaff accelerator was installed. Initially focusing on protons and light ions, the facility achieved terminal voltages of up to 3MV. Its main applications were centred on two ion beam analysis (IBA) techniques: proton-induced X-ray emission (PIXE) and Rutherford backscattering spectrometry (RBS). In 1991, the facility marked a significant advancement with the introduction of the first ion microprobe, featuring a magnetic quadrupole doublet from Oxford Microbeams Ltd. During this period, the laboratory also led developments in micro-PIXE (μ-PIXE) and micro-RBS (μ-RBS). Importantly, the facility played a pivotal role in the early development of ion beam-induced charge (IBIC), a technique now widely used to image charge transport properties in radiation detectors and various electronic devices.

Both accelerators are equipped with dual ion sources: one designed to produce ions of nearly all elements, while the other is specialized for helium beams. The 1 MV Tandetron is equipped with a Duoplasmatron ion source from the High Voltage Engineering Corporation, along with a single cathode sputtering source. However, the 6 MV Van de Graaff accelerator features an Alphatross source for alpha particles and a multi-cathode SNICS source for all other elements.

I.1 Beam lines and end stations

The accelerator facility at RBI comprises nine beam lines, depicted in the **Fig.3.2**. Of these, eight are only designated for investigating ion beam physics and its diverse applications. The ninth beam line is exclusively dedicated to low-energy nuclear physics experiments. This distribution of end station highlights how each beam line is specialized and caters to a wide range of research areas covered by the laboratories they belong to.

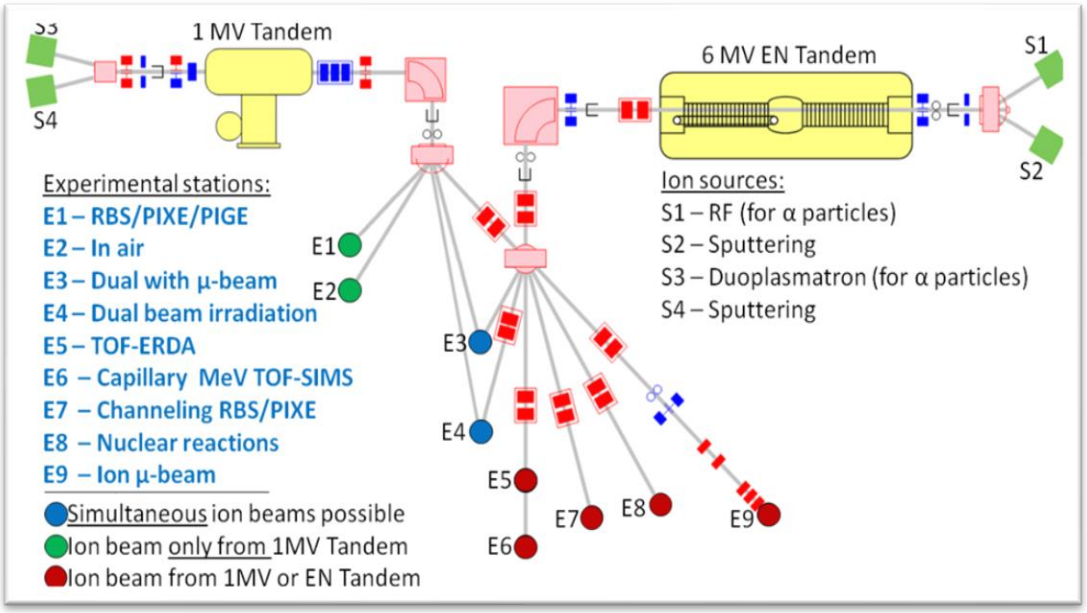

Figure.3.2: *Ion beam interaction laboratory layout at RBI.*

The beam emitted by the Tandetron accelerator can reach all end stations, whereas the beam from the VdG accelerator cannot access end stations E1 and E2. However, at end stations E3 and E4, beams from both accelerators can be simultaneously delivered. Most of thesis work took place at three principal end stations: the Ion Micro-beam End Station (E9), the PIXE and RBS Station (E1), and the Dual Ion Beam Station (E4).

I.1.1 PIXE and RBS station E1

The E1 station shown in **Fig.3.3** serves as a versatile scattering home chamber, acquired as part of the IAEA TC project. Positioned along the 45° line of the Tandetron accelerator (refer to **Fig.3.2**), it houses two PIXE detectors. One Silicon Drift Detector (SDD) designed for analysing light elements from sodium onwards, and one Silicon Lithium detector (Si (Li)) covers a broad solid angle fitted with a carefully optimized Mylar filter, enhancing its accuracy in detecting heavy elements like Potassium and Calcium.

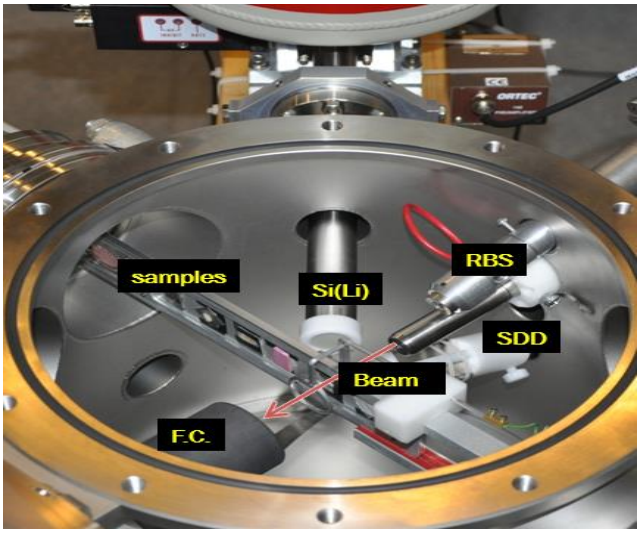

Figure.4.3: *PIXE/RBS end station.*

The chamber incorporates a sample holder capable of accommodating up to 16 samples, with sizes varying from 10 to 25 mm. These samples typically undergo exposure to a 2 MeV proton beam, which adopts a circular shape of either 3, 5, or 8 mm. The beam currents utilized during analysis range between 1 and 10 nano Amperes.

Simultaneously, this facility integrates other Ion Beam Analysis (IBA) techniques as Rutherford Backscattering Spectroscopy (RBS). Additionally, Elastic Recoil Detection Analysis (ERDA) or Proton Elastic Scattering Analysis (PESA) for hydrogen analysis.

I.1.2 Dual ion beam (DiFu) station E4

Originally intended for dual-beam irradiation of fusion materials, the chamber exhibits versatility, allowing for the irradiation of diverse sample types using a wide range of ion beams. The Dual-ion beam chamber for fusion materials is used for irradiating nuclear materials samples. In dual-beam mode, heavy ions induce damage concurrently with H and He implantation. **Fig.3.4** illustrate the DiFu chamber and some of its features.

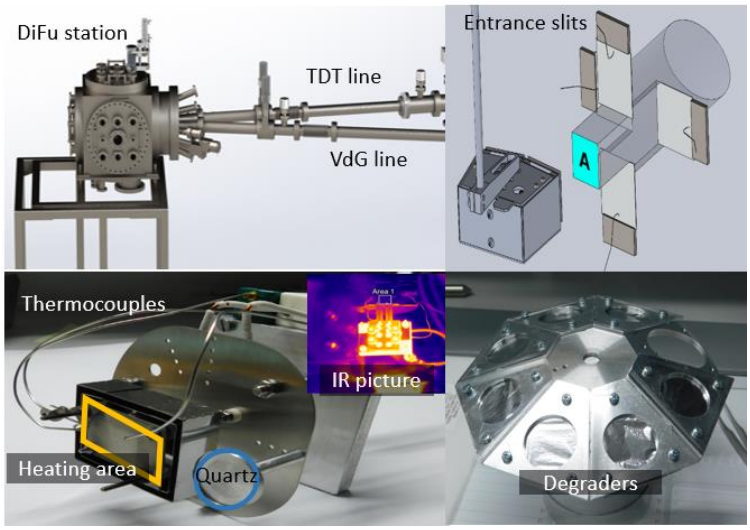

Figure.3.4: *Dual beam irradiation station for Fusion materials (DiFu).*

Ion beams with a spot size of a few millimetres enter the chamber at a 17-degree angle from two accelerators. Beams are scanned across the sample surface by electrostatic deflectors, covering an area of up to 30 x 30 mm². Sample temperature control allows for irradiation at temperatures of up to 800°C. The chamber, measuring 40 cm on each side, accommodates materials and samples of various geometries and purposes. For uniform irradiation across larger sample depths, each ion beam can traverse a rotating beam degrader to adjust the energy. Automatic retractable Faraday cups monitor beam current stability and fluence upon insertion. Pico-Amperemeters connected to slits at the chamber entrance monitor beam position and stability during irradiation.

I.1.3 Ion Micro-beam station E9

The heavy-ion microprobe station E9 is fully equipped to facilitate a wide range of Ion Beam Analysis (IBA) techniques at RBI. These techniques include PIXE, RBS, ERDA, Nuclear Reaction Analysis (NRA), Ion Beam Induced Charge (IBIC), Scanning Transmission Ion Microscopy (STIM), MeV Secondary Ion Mass Spectrometry (SIMS), Ion Luminescence (IL), and High-Resolution PIXE (HR–PIXE). The available ion beams span from protons (ranging from 0.4 to 8 MeV) to various heavier ions, with a maximum mE/q2 ratio of 18. Depending on the specific application and ion magnetic rigidity, a doublet or triplet of quadrupole focusing lenses is employed. In high current mode, crucial for IBA, PIXE, and/or RBS, operations typically involve protons or helium ions. All these techniques can be utilized for imaging

purposes, such as elemental distributions, or for conducting quantitative analysis at specific points or regions. **Fig.3.5** illustrates the microprobe station.

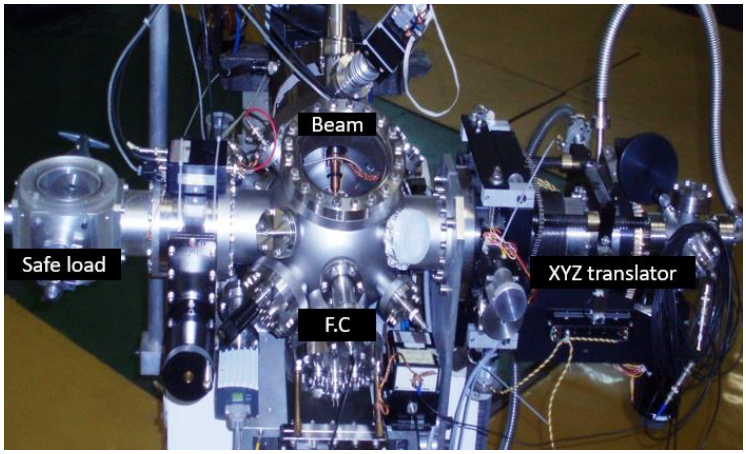

Figure.3.5: *Heavy ion Micro-Beam station.*

I.2 Data acquisition software

Data acquisition was conducted using a modular acquisition system consisting of a pre-amplifier, amplifier, ADC (analog-to-digital converter), and MCA (multi-channel analyzer). Under normal operating circumstances, ADCs are controlled through the SPECTOR data acquisition software. SPECTOR (**Fig.3.6**) is designed to oversee every aspect of the experiment, generate histograms and maps, and offer fundamental spectrum analysis tools during data acquisition to furnish sufficient data for real-time adjustment of the experiment to attain the desired results.

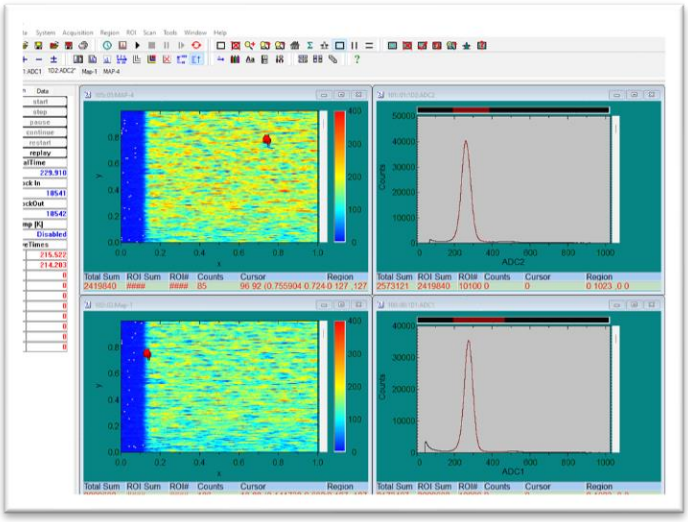

Figure.3.6: *Data acquisition software SPECTOR.*

II. Detection limit of routine RBS system at Ruđer Bošković institute RBI

Enhancing the sensitivity of Rutherford Backscattering Spectrometry (RBS) measurements for detecting heavy elements within a silicon matrix necessitates an initial understanding of the existing detection limits at our laboratory. To ascertain this limit, we conducted an analysis using silicon substrate samples implanted with varying doses of gold.

Gold was selected for this investigation due to its similar mass to the target element of interest witch is platinum (Pt). Additionally, gold is easily producible using a sputter ion source and can be accelerated by Tandem accelerator. This choice ensures practical and comparable calibration for our RBS system. Through this systematic evaluation of gold-dosed silicon samples, we aim to establish the baseline detection limit and subsequently implement strategies to enhance the sensitivity of our RBS measurements for heavy element detection within the silicon matrix.

II.1 Implantation of Au on Si

The standard RBS system at the Ruđer Bošković Institute (RBI) is typically employed for analyzing samples with concentrations exceeding 10^{16} at/cm². Consequently, the maximum gold implantation dose should not surpass this threshold as we already know that is measurable. Four samples were subjected to implantation with varying doses of Gold (Au), ranging from 5 x 10^{14} at/cm² to 10^{16} at/cm².

The implantation process took place at the low-energy side of the 6 MV Tandem accelerator after the injector magnet. Gold ions were generated using the multi-cathode sputtering source MC SNICS 40. The final ion energy at the target was achieved by combining the extraction energy (20 keV) with pre-acceleration (18 keV), resulting in a total energy of 38 keV.

This energy was selected to ensure a surface implantation. The beam current of the gold ions, measured with a faraday cup was around 100 nA. The beam's profile was visualized using a quartz to ensure precision and accuracy during the implantation process.

II.2 RBS Measurement of implanted samples

The analysis of samples was carried out using 2 MeV alpha particles, which were delivered by a 1 MV Tandetron accelerator. The measurements took place at PIXE and RBS station E1

(Chapter 03), and the alpha particle beam was generated using duoplasmatron ion source. The cumulative charge for all samples, including a silicon standard with an implantation of 1 x 10^{15} Cs/cm^2, amounted to 6 µC.

A surface barrier detector with a total solid angle of 1,3 msr was used to detect the backscattered particles. The alpha particle beam had a measured current of 10 nA and a spot size of 3 mm. Data were collected using SPECTOR software, and subsequent analysis was performed using SIMNRA. **Fig.3.7** illustrates the normalized spectra for all the implanted samples.

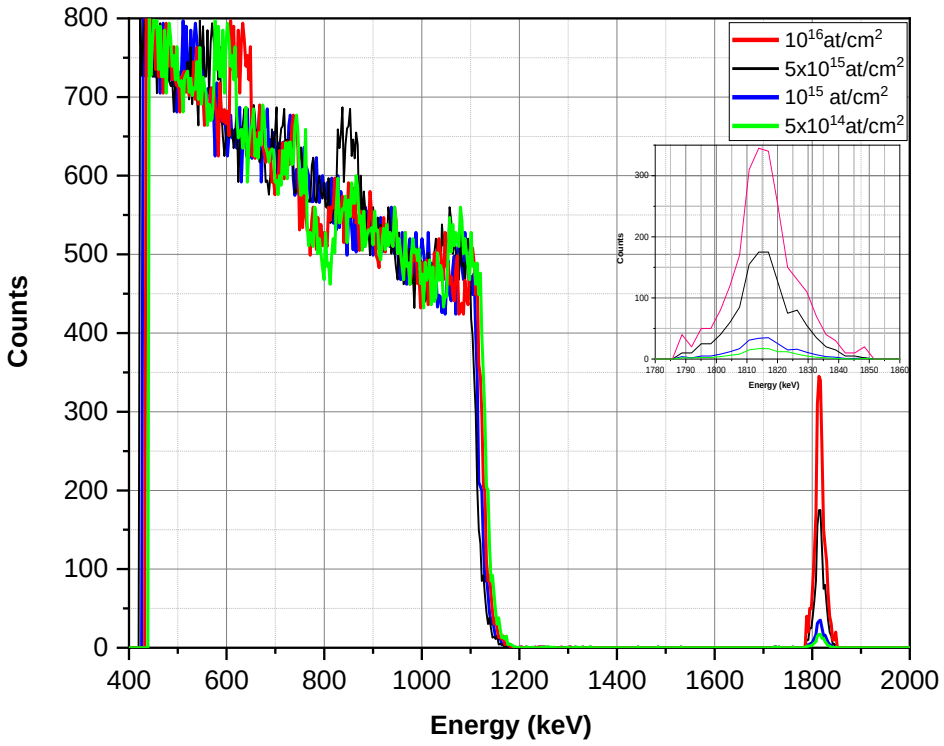

***Figure.3.7**: Normalized RBS spectra of implanted Au in silicon.*

Quantifying a concentration of 5 x 10^{14} at/cm² is challenging and susceptible to inaccuracies, whereas a concentration of 10^{15} at/cm² could be measured with a statistical error of 11%. Based on the outcomes of this experiment, it can be assumed that the detection limit of our RBS system is approximately 10^{15} at/cm².

III. New setup to improve RBS sensitivity

The developed setup is based on optimizing the irradiation parameters, including probing ion beam characteristics, measurement parameters such as detection geometry, and the data analysis method.

III.1 Probing ion beam

The selection of the appropriate ion microbeam, in terms of ion mass and their respective energy, was the first step in this investigation. In order to avoid pile-up effects in backscattering spectra (from the substrate), the ion beam used has to be equal or heavier than the main constituent of the sample, which is silicon in this case. Also, the RBS setup should be capable to analyse wide range of heavy elements and therefore the heaviest ions (used as a beam) that may offer the highest cross section, should be avoided. In these circumstances, while considering that at most of the tandem accelerators heavy ions are primarily supplied by sputtering ion sources, the highest beam currents could be expected either for Cl or Si ions. In our case the Si ion beam has been selected.

Unlike the numerous studies in the literature that use broad beams of heavy ions for RBS, this work aims to utilize a microbeam with significantly smaller currents (~1nA). The RBS technique using Si ions can be fully described by classical scattering, which takes into account the Coulomb potential and Rutherford backscattering cross-section (Part2 of Chapter2). Reducing the energy of Si ions can increase the cross-section; however, the energy resolution of Si particle detectors, which ranges from 180-250 keV, imposes limitations on further reductions of ion beam energy. Additionally, focusing lower energy ions to a micrometer-sized beam is challenging, particularly due to the presence of a beam halo. In high-sensitivity analysis, it is crucial to maintain and focus the beam on the target to minimize scattering from residual gases along the beam line and in the vacuum chamber, an issue that worsens as ion energy decreases. Considering these factors, a 2.4 MeV Si^{2+} beam was selected as the optimal probing beam for this experiment, balancing beam quality (spatial resolution), detector energy resolution, and a high Rutherford backscattering cross-section.

III.1.1 Measurement of 2.4 MeV Si^{2+} beam brightness

Accelerated ion beams have long been employed in nuclear microprobes, serving as a fundamental tool for conducting elemental microanalysis of trace impurities within Silicon. RBS elemental maps are utilized to visualize the spatial distribution of these trace impurities, achieving a lateral resolution on the order of a few micrometers, even at minimal concentration levels. The primary limitations in resolution comes from certain inherent system properties, such as low-quality ion sources and bad beam optics, leading to a low brightness probing beam.

The brightness of the beam is a critical factor affecting its quality, determining the proportion of the total emitted ion beam that can accurately reach the designated sample position. Consequently, due to the diminished brightness, only a fraction of the emitted ion beam can be effectively directed to the precise location on the sample. The brightness of the beam serves as a key metric for assessing its quality, and this can be quantified using the equation 60 (refer to Part2 of Chapter 2). **Fig.3.8** shows the microprobe setup of the RBI facility.

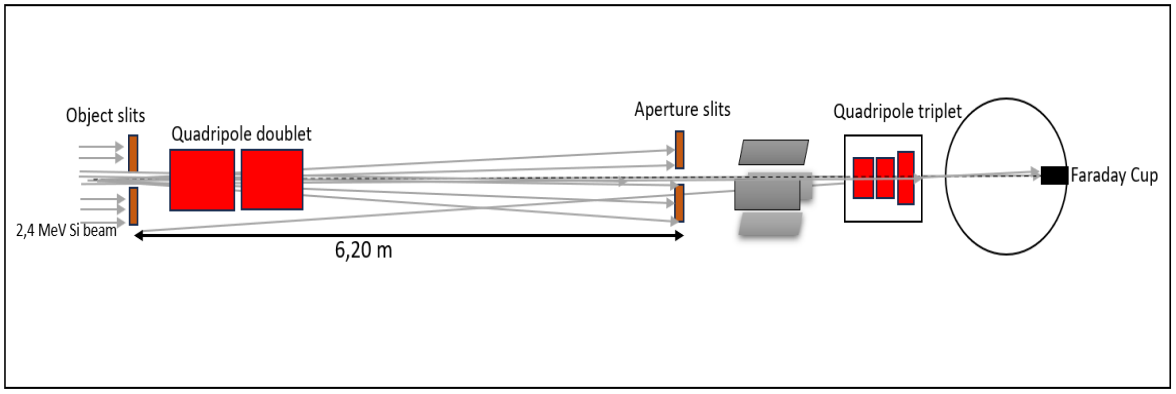

Figure.3.8: *Microprobe setup at RBI.*

To quantify the brightness of the probing beam (2.4 MeV Si^{2+}), a matrix that captures the relationship between beam current measurements and the diameters of both aperture and object slits was created. The adjustable range for object slits diameter spans from 75 to 150 µm, while the aperture slits can be varied within the range of 0.25 to 5 mm. The separation distance between the aperture and object slits is approximately 6.20 m. To acquire current measurements for various combinations of object-aperture diameters, a Faraday cup was employed.

The Tab.1 contain the beam current matrix, expressed in nanoamperes (nA). This matrix serves as a dataset for evaluating and defining the brightness of the probing beam under different aperture and object slit configurations.

	Object diameter (µm)			
Aperture diameter(mm)	150	125	100	75
5	0,810	0,620	0,350	0,190
4	0,570	0,380	0,250	0,130
3	0,400	0,250	0,150	0,090
2	0,200	0,140	0,080	0,050
1,5	0,130	0,100	0,060	0,035
1	0,057	0,045	0,027	0,016
0,75	0,035	0,025	0,016	0,009
0,5	0,015	0,011	0,007	0,005
0,25	0,004	0,004	0,003	0,002

Table 1. Current matrix (nA) for 2.4 MeV Si^{2+} probing beam.

The brightness of 2.4 MeV Si^{2+} ion beam produced by MC SNICS source and accelerated by 6 MV VdG Tandem accelerator operating with a mixture of CO_2 and N_2 as striper gas is presented by **Fig.3.9**.

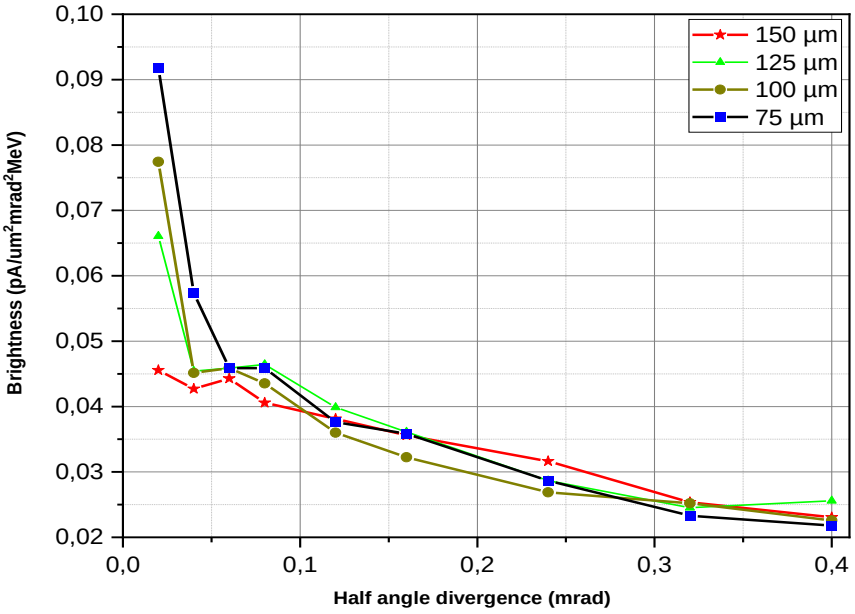

Figure.3.9: *Brightness distribution as function of half angle divergence.*

The beam brightness experiences a decline as the apertures of both the object and aperture slits widen; nevertheless, this decrease is accompanied by an increase in beam current. Given the system's intended application for sensitive analysis, there is a preference for a higher current to minimize measurement time, and concurrently, a heightened brightness is essential for enhanced precision.

To strike a balance between precision and efficiency, a compromise has been reached by opting for a 1.5 mm diameter for the aperture slits and a 150 µm diameter for the object slits. This configuration is considered to meet the dual objectives of maximizing current for sensitive analysis while ensuring sufficient brightness for enhanced precision in the measurements.

III.1.2 Beam halo determination

The vacuum in the chamber, the beam energy and the masse of particles are different parameters that can increase the beam halo. An increased beam halo can flood the spectra and drone different elements in precise position. An IBIC measurement was carried out to determine the angular spread of 2.4 MeV Si^{2+} beam. **Fig.3.10** shows the setup of the measurement; the beam was scanned in X and Y direction through 100 µm hole placed in front of the detector. The scan size was about 1x1 mm.

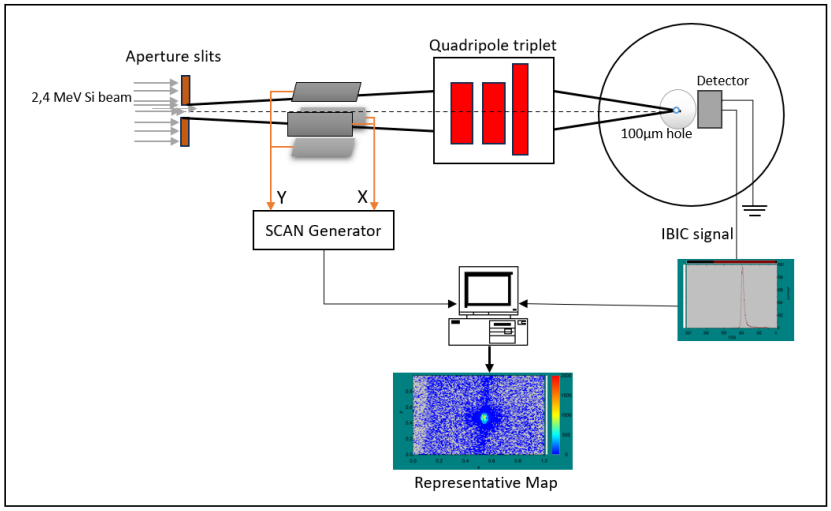

Figure.3.10: *Representative setup of the IBIC measurement for beam halo determination.*

The IBIC signal was processed to produce a map of collected charge distribution as a function of the position. Later, the beam shape was derived from the map distribution as shown by Fig.**3.11**.

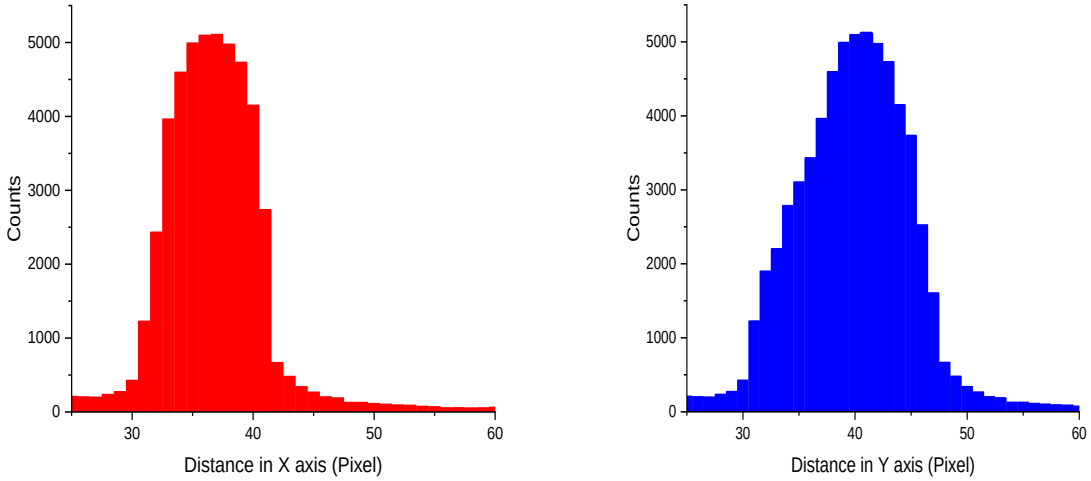

Figure.3.11: Beam shape in X and Y axis after scanning over 100 µm holes.

The beam halo is significant along both the X and Y axes; however, it is notably more important along the Y axis because the beam was intentionally focused more tightly on the X direction. To enhance measurement precision, minimizing the beam halo is crucial. In this context, strategies to reduce the halo will be discussed, with a particular focus on the use of a collimator, whose implementation and effects will be presented in detail later in this manuscript.

III.1.3 Spatial resolution of the probing beam

The ion beam was focused on the target using an Oxford quadrupole triplet, and its visualization was achieved with a quartz screen. To measure the beam size, a copper grid with 60 µm gaps was employed. The beam was scanned over a 400x400 µm area on the copper grid, and the backscattered ions were collected for analysis. **Fig.3.12** illustrates the grid used for estimating the beam size: (a) presents a microscope image of the grid, while (b) shows the corresponding RBS intensity map. This method allowed for precise determination of the beam's dimensions and ensured accurate focusing on the target.

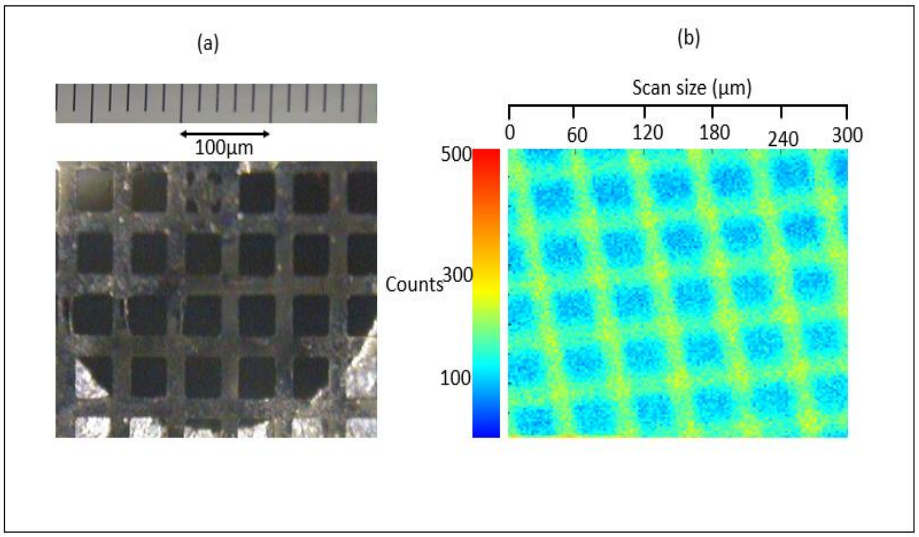

Figure.3.12: *Probing beam resolution estimation using Cu gride; (a) Microscopic image of the grid and (b) is the RBS map.*

The microbeam spot size for these experimental conditions was estimated to be approximately 10 µm. Higher spatial resolution has been obtained for the horizontal plane.

The counts recorded in the open area of the grid are a result of the beam halo generated by a high-current microbeam (approximately 1nA). This setup requires using the maximum achievable beam current to effectively measure the depth profile of Pt within a reasonable timeframe. To enhance the accuracy of the measurement, it is imperative to subtract this background when conducting any quantitative analysis within this configuration.

III.2 Detection system

III.2.1 Detectors

To enhance the counting statistics within an acceptable measurement time, high detection solid angle is essential. This can be achieved by utilizing a large sensitive area detector or multiple detectors. However, using a large number of detectors may result in an excessive distance between the sample and detector, leading to an absence of small scattering angles. Also, the data acquisition system has to accept a large number of detectors. In this study, only two Si pin photodiodes (Hamamatsu S3590-09) of 10mm x 10mm sensitive area shown in **Fig.3.13** were used as detectors, mounted above and under the microbeam axis.

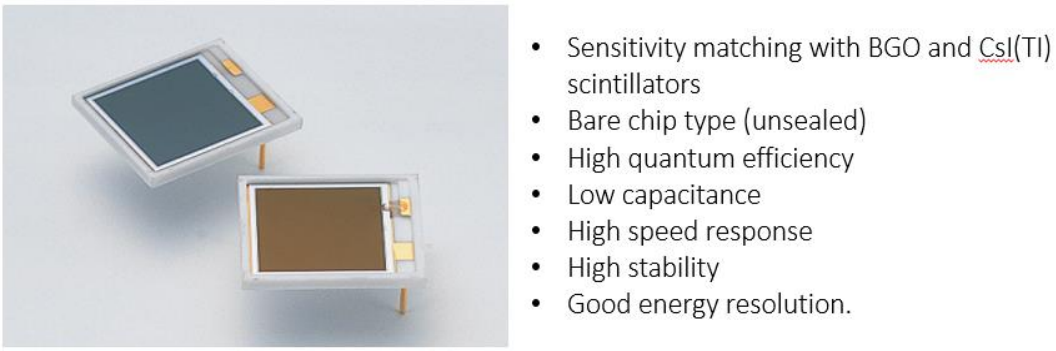

Figure.3.13: *PIN photodiode used as detectors.*

III.2.2 Detection geometry

In order to reduce the measurement time to practical values, we have to enhance the detection solid angle. The main challenge in this situation pertains to the kinematic spread resulting from a wide detection angle range. Because the Rutherford backscattering cross section varies with the scattering angle, a large solid angle will encompass a broad range of scattering angles. As such, the absolute quantitative analysis of depth profiles, spectra must be partitioned into numerous smaller scattering angles.

The pin photodiodes were mounted on a holder, as illustrated in **Fig.3.14**, with an optimized geometry to maximize the detection solid angle. In this configuration each detector is covering solid angle of about 0,52 sr. The sample to detector distance at its nearest point is minimized to only 1 mm.

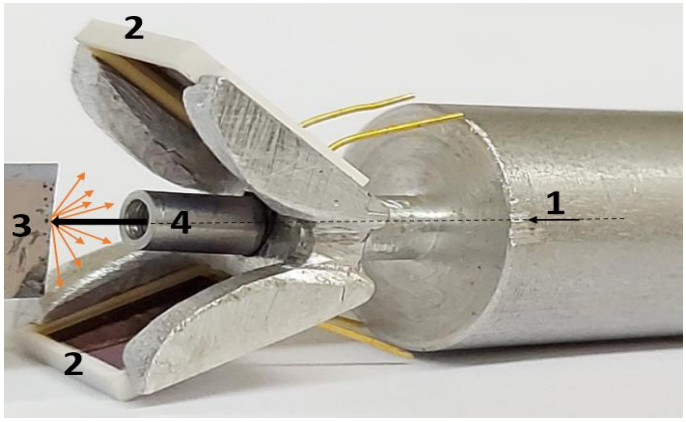

Figure.3.14: *RBS detection geometry (1. Probing beam direction, 2. PIN diodes, 3. Sample, 4. Collimator).*

The position of the PIN diodes mounted Up and Down was adjusted to maintain symmetry during the scanning process and also to enable sample viewing from the left side where the long working distance microscope is positioned.

In the first version of the setup, a significant increase of the background has been observed. It was associated with a scattering of the beam halo ions from sample regions outside of the scanning area and from other parts of the sample and detector holders. In order to reduce these events, an upgraded detector holder that included extended collimator of a 2 mm diameter exit nozzle was used to shield the diodes from the events caused by the beam halo. In **Fig.3.15** the comparison of spectra obtained with and without this collimator is shown.

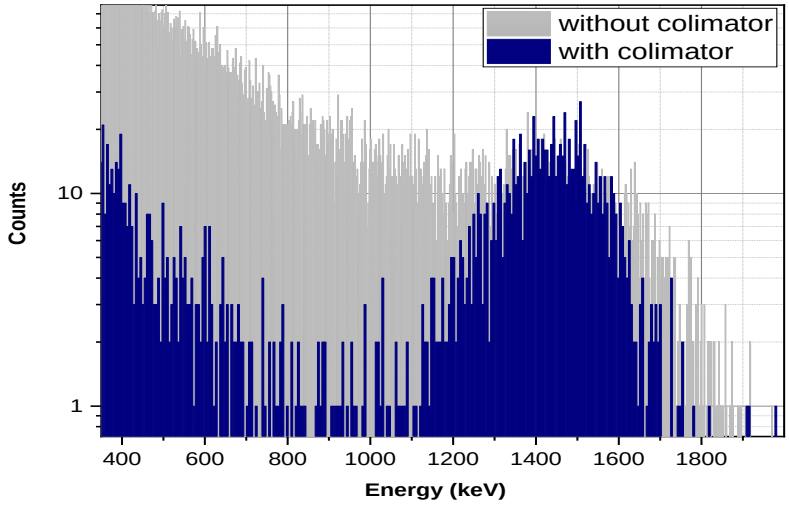

Figure.3.15: *Comparison of RBS spectra of low Pt concentration implanted on silicon obtained with and without collimator.*

The collimator plays a crucial role in the setup. It effectively removes a significant portion of the background noise that affects the spectrumwithout the need to close the object slits' aperture, thereby preserving a high microbeam current for fast measurement.

III.2.3 Energy resolution measurements

To do any quantitative or qualitative analysis of RBS spectra using SIMNRA, the energy resolution of the PIN diodes in detecting heavy ions must be determined. Based on the geometry adopted for the setup, backscattered ions traverse the detectors at varying entering angles, resulting in a longer path through the detector's dead layer. To assess the impact of

straggle as a function of the entrance angle on detector resolution, we conducted IBIC measurements using 2.4 MeV Si^{2+} ions. During these measurements, the detector was systematically rotated from 90° to 69° in 3° increments. Consequently, the detector's resolution exhibited variations ranging from 220 to 250 keV.

Entrance angle (°)	90	87	84	81	78	75	72	69
Detector resolution (keV)	220	230	236	238	240	245	247	250

IV. Data analysis

IV.1 Calibration

For the RBS quantitative analysis, it is essential to know the detector solid angle (Ω) as well as the number of impinging beam particles (Q) during each measurement. The latter, in the corresponding analysis, contributes as a product (QΩ), which must be determined.

Since the direct measurement of the current from the sample is not reliable and practical for the determination of the impinging particle, indirect measurement was used. This was done using a chopper positioned in a separate miniature scattering chamber after the collimating slits and before the focusing quadrupoles as shown in **Fig.3.16**. It consists of a gold coated rotating vane and a surface barrier detector that detects backscattered ions. The chopper was programmed to interrupt the beam for 1 second every 10 seconds during the measurement. The minimum measurement duration was 500 seconds for most of the measurements, meaning that the beam was cut 50 ± 1 times with 2% of error. The count numbers recorded by the SB detector were utilized to calibrate the QΩ of unknown samples by means of calibrating the chopper counts with the use of certified calibration standards.

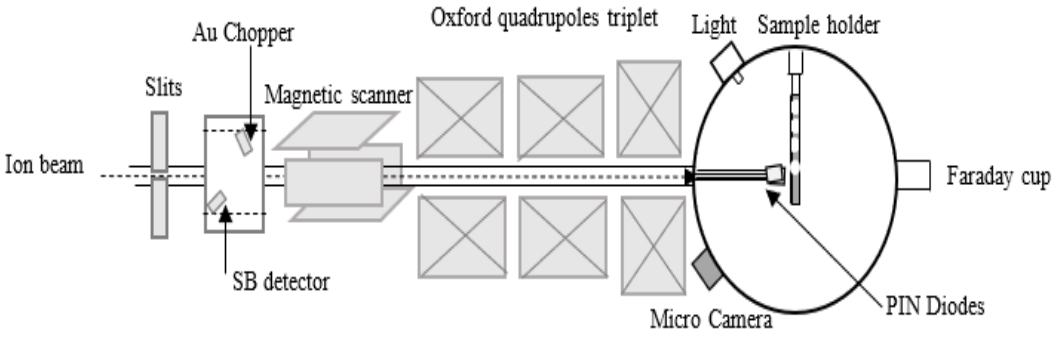

Figure.3.16: *Microprobe end station setup at Ruđer Bošković Institute.*

The accurate description of the setup geometry is essential for the reliable interpretation of the measured spectra. In our setup, the detectors span the region where ions are backscattered at angles ranging from 100° to 170°, calculating the contribution of each scattering angle in the range of the detectors solid angle on the accumulated spectrum is important. As it is shown in **Fig.3.17**, we have divided these contributions to seven different scattering angles: 105°, 115°, 125°, 135°, 145°, 155°, and 165°. With 10° step, the most significant difference in backscattering energy observed was 36% of the detector's energy resolution. Notably, this difference remains below the 50%, indicating that an angular rang of 10° effectively mitigates the effects of kinematic dispersion arising from the utilization of a large detection solid angle. The number of total counts was calculated using the equation:

$$N = \sum_{i=105°}^{165°} \frac{Q\Omega_i}{Q\Omega} N_i \tag{61}$$

Where Ω is the total solid angle, Ωi are the partial solid angles corresponding to the scattering angles 105°-165° illustrated on the **Fig.3.17**, and Q is the total number of beam particles on the target during measurement time.

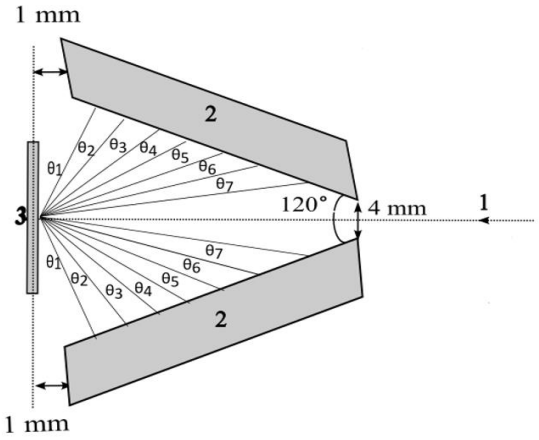

Figure.3.17: *Backscattering angles covered by the PIN photodiodes in the new setup.*

Considering the geometry of **Fig.3.17,** the contribution of each scattering angle to the final simulated spectrum is displayed by **Fig.3.18**. The calibration equation (eq61) was derived using 5.8x10^{16} at/cm^2 Au standard and the QΩ for each scattering angle was determined by fitting the experimental spectrum using SIMNRA, resulting in:

$$N= 0{,}049N_{105}+ 0{,}126N_{115}+ 0{,}345N_{125}+ 0{,}565N_{135}+ 0{,}513N_{145}+ 0{,}420\ N_{155}+ 0{,}356\ N_{165}.$$

The variation in the coefficient within the equation is directly proportional to the variation in the factor$\Omega_i\sigma_i$; where σ_i is the Rutherford backscattering cross section and Ω_i are the detection solid angle for each backscattering angle i.

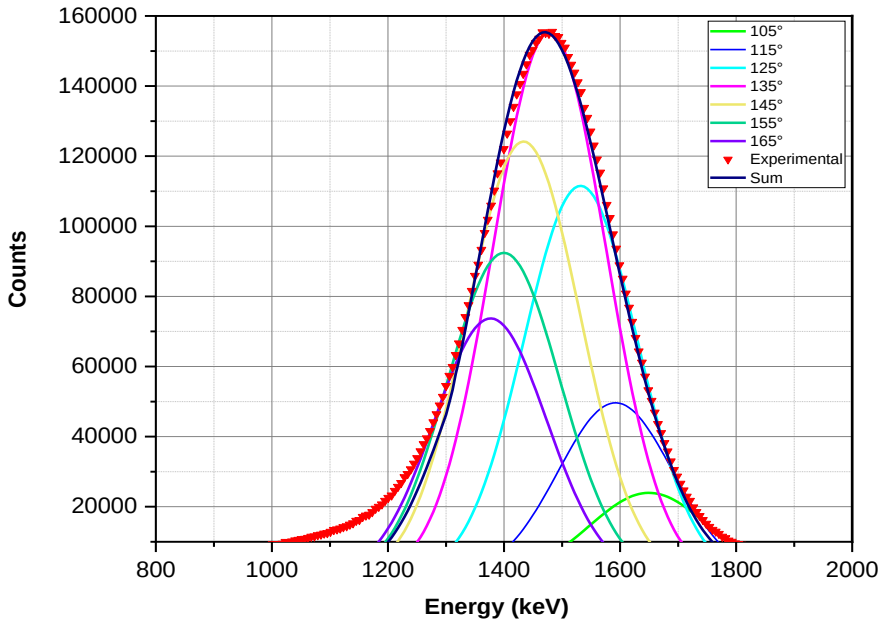

Figure.3.18: *Experimental and simulations RBS spectra of Au standard.*

IV.2 Reference standard measurement

Two reference standards were measured to verify the calibration; the first was 4.647x10^{15} at/cm^2 As and 3.075x10^{15} at/cm^2 Ar implanted in Si which were previously used in a quality insurance round robin organized by Surrey University[140]. The second reference standard was 1.01x10^{15} at/cm^2 of Cs implanted in Si. **Fig.3.19** illustrates the obtained spectra (a) As and Ar on Si, where the Ar contribution cannot be seen due to its small mass difference with the probing beam, and (b) shows Cs on Si spectrum.

The measured value of As and Cs were 4.74±0.09x10^{15}at/cm^2 and 1.08±0.03x10^{15} at/cm^2 respectively.

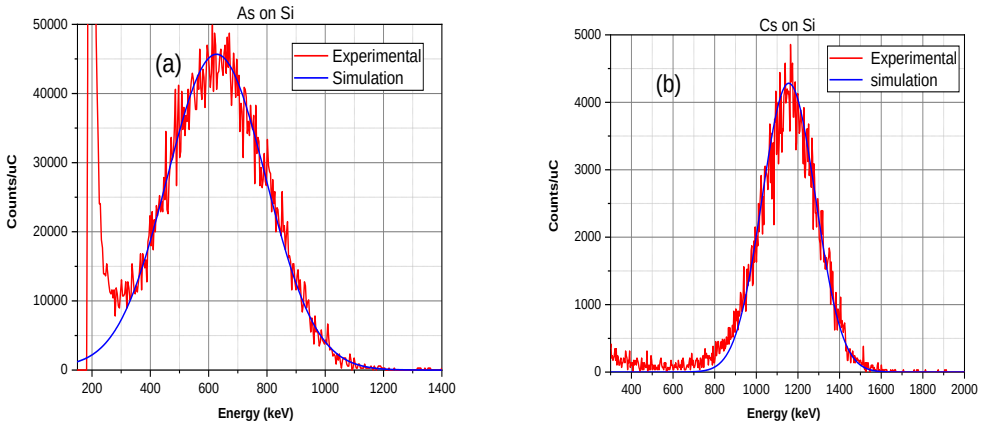

Figure.3.19: *Reference standard spectra obtained by RBS, (a) As and Ar implanted in Si, (b) Cs implanted in Si.*

Compared to certified value, the attained results demonstrated an uncertainty level of approximately 2.2% for As and 6.9% for Cs standard. The difference in measurement uncertainty between As and Cs standards can be attributed to the significant difference in concentration. This implies that the Pt samples require an extended measurement duration to reduce the statistical uncertainty and to amplify the instances of beam interruption by the chopper, thereby minimizing calibration error and elevating result precision and accuracy

V. Detection limit of the new setup

The determination of the detection limit will adhere to the procedure outlined in section 1, which involves the implantation of heavy elements in Silicon at various doses, followed by RBS measurements.

V.1 Implantation of 10 MeV Au on Silicon

Before going to measure samples of interest, knowing what the system limitation to measure trace element implanted in Silicon would be of great interest. In order to determine the detection limit of the new setup, 10 MeV Au ions were implanted in Si with very low concentration at DiFu end station (chapter 3). The gold ions energy was chosen to have the same range in silicon as the probing beam.

Implantation of very low doses needs a strict control of beam current and implantation time, to do so a slit control installed in the entrance of the chamber to measure the stability of the beam

current during irradiation time. The beam current was set to be around 0,1-0,5 nA. The beam shape and the implantation profile were visualized via a quartz. 4 samples were implanted with dose range from 10^9 at/cm^2 to 5x10^{10} at/cm^2. The implantation error is expected to range from 1% to 20%, depending on the irradiation duration.

V.2 RBS measurement of implanted gold

The implanted gold samples were measured using a 2.4 MeV Si^{2+} microbeam. The microbeam current was measured by Faraday cup at the microbeam chamber and measures around 1 nA. **Fig.3.20** shows the obtained spectra for all different doses after 1 hour of measurement for each sample.

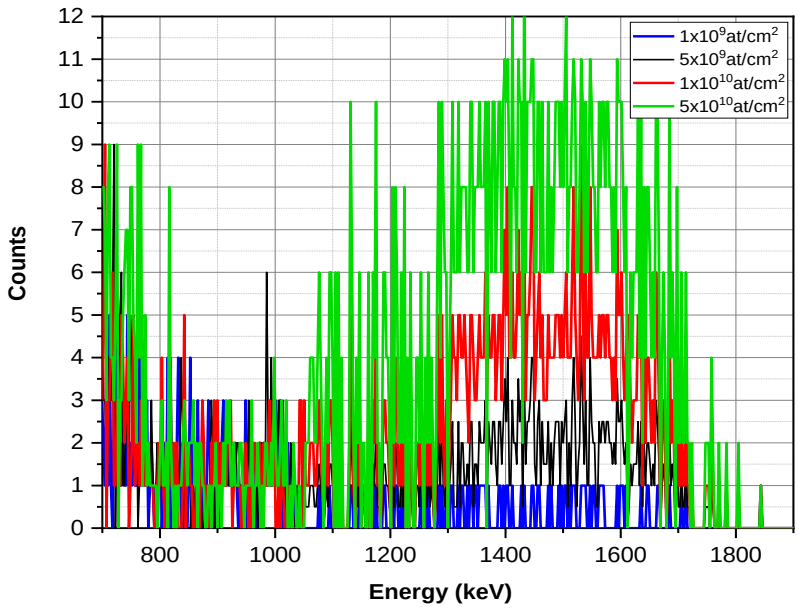

Figure.3.20: *RBS spectra of Au on Si obtained for various implantation doses.*

Same calibration method was applied in order to do quantitative analysis. The measured values are presented as following:

Implanted (at/cm^2)	5.0±0.05 x10^{10}	1,0± 0.06x10^{10}	5.0±0.5 x10^9	1.0±0.2 x10^9
Measured (at/cm^2)	4,97±0.21 x10^{10}	1,3±0.9 x10^{10}	6.1±0.61 x10^9	/

The implanted sample with 10^9 at/cm^2 was impossible to measure with the new setup, therefore we assume that the lowest possible dose that can be measured with this setup was $5x10^9$ at/cm^2 with an uncertainty of 10%.

VI. Determination of low Pt concentration depth profile in Silicon

The goal of this work is to determine the depth profile of implanted Pt in Si with very low concentration using the new setup. After calibration and test by reference standard measurement, the setup is ready for the measurement of samples of interest.

VI.1 Samples

The experiments described in the present work were performed using Pt implanted on 375±15µm thick silicon wafers following the steps described in the first chapter of this manuscript. A platinum silicide layer was formed at one side then the wafers were annealed at 810° C and 850°C to promote the diffusion of platinum to the other side, the samples (**Fig.3.321**) were prepared at Università degli Studi di Torino.

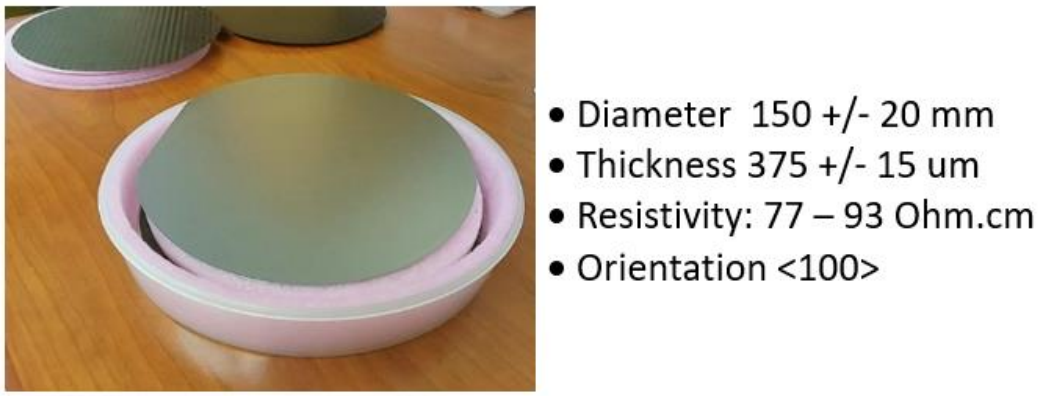

Figure.3.21: *Silicon wafers after Pt implantation.*

Simulation models of platinum diffusion in silicon (Chapter 01) predict that the depth profile of Pt implanted in Si through all implantation process followed by annealing at high temperature has a U-shape. **Fig.3.22** depicts the simulated Pt profile after 2 hours of annealing at 830°C using the model of Pt diffusion from Pt-silicide proposed by A. Johnsson et al[19].

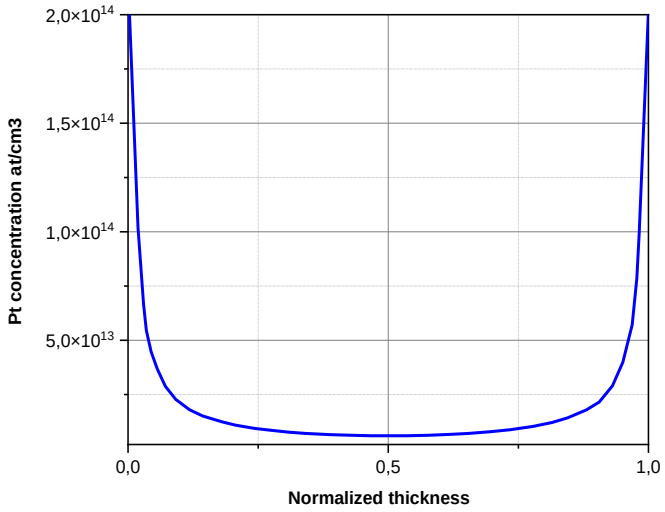

Figure.3.22: *Simulated Pt depth profile after 2 hours of annealing at 830°C using the model proposed by A. Johnsson et all [19].*

The simulated profile will be utilized to be compared with the measured profile based on RBS technique using the new setup.

These samples were selected for their significance in the study and potential impact on the advancement of high-power silicon-based devices. Also, measuring the depth profile of very low concentrations of Pt in silicon using a microbeam with a lateral scan presents a challenge. The objective of the experiment is to investigate the capability of the new RBS setup in the determination of the depth profile of platinum with low concentration. Eight samples in total, four from each silicon wafer, annealed at 850°C and 810°C, were measured, including the front and back sides and two lateral scans. **Fig.3.23** illustrates the position of the samples during measurement.

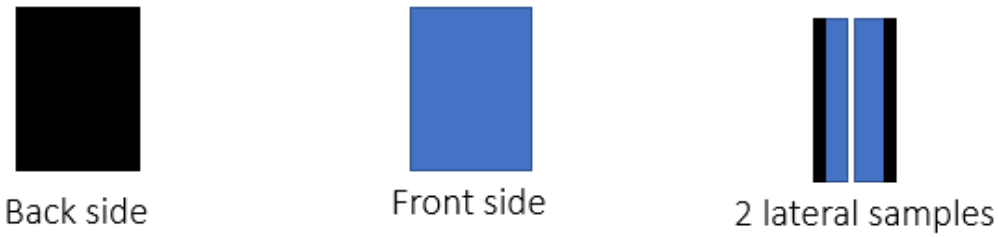

Figure.3.23: *Position of the samples during measurement.*

VI.2 Front and Back measurement

The output signals from the PIN diodes were gain-matched and combined into a single spectrum, which was subsequently analyzed by SIMNRA. The measurement was performed using a 1nA current microbeam, and both sides of both silicon wafer were measured in a reasonable amount of time (approximately 2hours for all). The backsides of the wafers contain a Pt layer with a thickness of approximately 1.728 ± 0.028 x10^{16} at/cm^2 and 1.072 ± 0.030 x10^{16} at/cm^2 for 810°C and 850°C respectively, this layer was a residual from the initial deposition of Pt silicide after annealing. The front side had a very low concentration of Pt, with levels of 3.58 ± 0.15 x10^{11}at/cm^2, and 4.22 ± 0.15 x10^{11}at/cm^2 for 810°C and 850°C samples respectively. **Fig.3.24** shows an example of the obtained spectra.

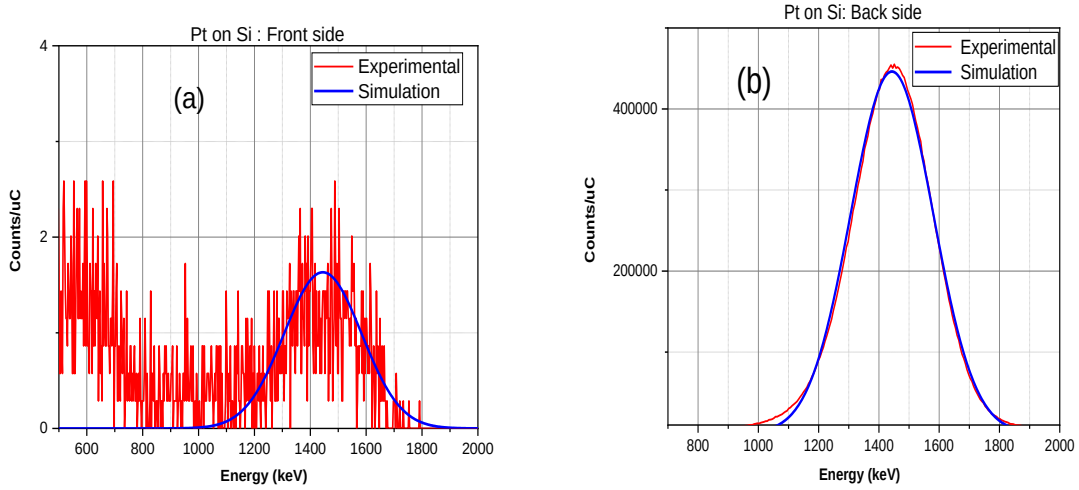

Figure.3.24: *RBS spectra of Pt implanted in silicone by Pt diffusion from pt-Silicide layer process annealed at 850°C; (a) is the front side and (b) back side of the silicon wafer.*

VI.3 Lateral scan for depth profile determination

A lateral scan of 800 µm of Si wafer thickness have been done in order to determine the depth profile of Pt in Si. **Fig.3.25** shows the representative map of Pt distribution after one-hour of continuous scan.

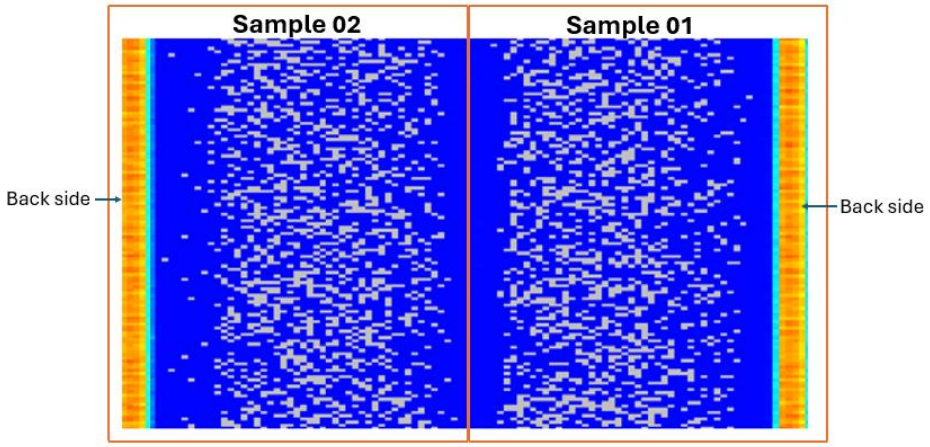

Figure.3.25: *Pt distribution on two samples obtained through lateral scan lateral scan.*

The back sides of the samples contain a layer of Pt residual of the initial deposited Pt-Si layer, this layer is outside of the interest region because in the power devise industry it must be polished. The depth profile for one sample after removing the residual Pt-Si layer is presented by **Fig.3.26**.

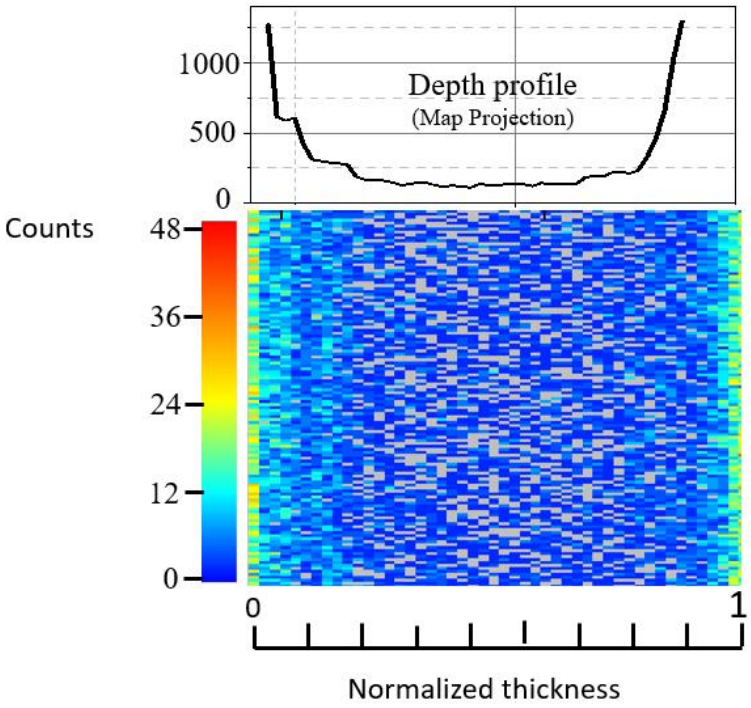

Figure.3.26: *Representative map of Pt distribution by lateral scan on Si wafer thickness*.

The relative areal densities were extracted from the map and absolute concentrations were obtained using the front and back sides concentration. For the direct comparison of the obtained results with the profiles predicted by the simulation model, the areal densities (at/cm^2) are

converted to atomic concentration(at/cm^3). **Fig.3.27** displays the Pt concentration distribution as a function of thickness for the annealed samples at 850°C and 810°C compared to the simulated depth profile of the same samples annealed at 830°C. The obtained Pt concentrations are well within the expected values.

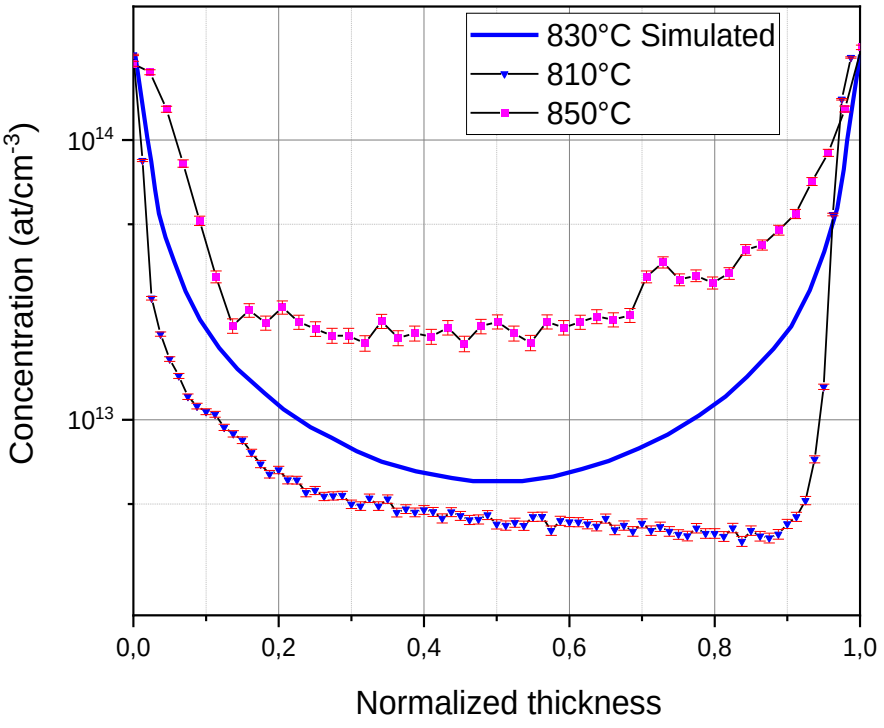

Figure.3.27: *The depth profile of Pt in Silicon defined by RBS technique for 810 °C and 850°C annealing temperatures compared to simulated profile at 830°C by A. Johnsson et all[19].*

General Conclusion

This thesis presents a novel setup for high-sensitivity depth profiling of heavy elements using the Rutherford Backscattering Spectrometry (RBS) technique. The approach focuses on optimizing irradiation and measurement parameters, including the characteristics of the probing beam (such as ion beam mass, energy, and current) and geometrical parameters (like maximizing the detection solid angle and targeting the small backscattering angle where the cross section is at its peak). These optimizations were conducted carefully to avoid complications in data analysis. For example, using a low-energy heavy element could result in significant scattering from residual gases in the reaction chamber, leading to high background noise in the spectrum. Additionally, maximizing the detection solid angle with a multi-detector assembly complicates data acquisition and analysis due to kinematic spread issues. Thus, a balanced approach was taken to define the final setup based on individual parameter studies.

The performance of the developed setup was evaluated using samples of platinum (Pt) on silicon (Si). The depth profile of Pt obtained was consistent with the U-shaped profile predicted by simulation models of Pt diffusion from a silicide source. These promising results suggest that the optimized RBS technique is effective for studying Pt implantation in Si, providing precise data that could improve Pt dosage and thermal treatment processes in the production of high-power electronic devices.

Using a probing beam equal or heavier than the substrate elements is crucial for trace element analysis to eliminate pile-up and allow for higher beam currents. The setup has successfully measured elements with atomic masses greater than arsenic (As), although it struggles with elements lighter than argon (Ar). Depending on the substrate composition, alternative probing beams with masses greater than all substrate elements could be used to eliminate backscattering from all elements except the element of interest, such as analysing heavy elements in diamond using a carbon beam.

Future work aims to enhance the setup’s capabilities for multi-element analysis. This is challenging due to the low energy resolution of the detectors. When there is a significant difference in element concentration, it becomes difficult to measure low-concentration elements with acceptable accuracy.

References

1. S. M. Sze, K. K. Ng, *Physics of Semiconductor Devices*, Wiley-Interscience, 2007.
2. R. F. Pierret, *Semiconductor Device Fundamentals*, Addison-Wesley, 1996.
3. D. K. Schroder, *Semiconductor Material and Device Characterization*, Wiley, 2006.
4. S. Tiwari, *Compound Semiconductor Device Physics*, Academic Press, 1992.
5. J. J. Liou, H. R. Jiann, *Advanced Semiconductor Device Physics and Modeling*, Artech House, 2001.
6. E. Golla, *Crystal Growth and Evaluation of Silicon for VLSI and ULSI*, CRC Press, 2014, pp. 253–, ISBN 978-1-4822-3282-0.
7. J. Guldberg, *Neutron-Transmutation-Doped Silicon*, Springer Science & Business Media, 2013, pp. 437–, ISBN 978-1-4613-3261-9.
8. P. M. Christopher, C. S. William, *Bismuth-Doped Silicon: An Extrinsic Detector For Long-Wavelength Infrared (LWIR) Applications*, Mosaic Focal Plane Methodologies I, Vol. 0244, 1981, pp. 2–8, doi:10.1117/12.959299, S2CID 136572510.
9. H. S. Rauschenbach, *Solar Cell Array Design Handbook: The Principles and Technology of Photovoltaic Energy Conversion*, Springer Science & Business Media, 2012, pp. 157–, ISBN 978-94-011-7915-7.
10. I. Weinberg, H. W. Jr Brandhorst, *Lithium counter doped silicon solar cell*, US patent 4608452.
11. A. Blicher, *Field-Effect and Bipolar Power Transistor Physics*, Elsevier, 2012, pp. 93–, ISBN 978-0-323-15540-3.
12. A. Johnsson, *Ph.D. Thesis*, University of Erlangen-Nuremberg, 2019.
13. N. Mohan, T. Undeland, W. P. Robbins, *Power Electronics: Converters, Applications, and Design*, 2nd ed., John Wiley and Sons Inc., 1995.
14. J. Lutz, H. Schlangenotto, U. Scheuermann, R. de Doncker, *Semiconductor Power Devices*, 2nd ed., Springer Verlag, Berlin Heidelberg, 2018.
15. H. Ruthing, F. Hille, F. J. Niedernostheide, H. J. Schulze, B. Brunner, *Proc. Of the 19th Inter. Symp. on Power Semiconductor Devices & IC's*, IEEE, Piscataway, 2007, pp. 89–92.

16. B. J. Baliga, E. Sun, *IEEE Trans. Electron Devices*, 1977, 24, 685.

17. J. Yang, Y. Che, L. Ran, H. Jiang, *IEEE Access*, 2020, 8, 104074.

18. M. Hauf, C. Sandow, F.-J. Niedernostheide, G. Schmidt, *2018 IEEE 30th Inter. Symp. on Power Semiconductor Devices and ICs (ISPSD)*, IEEE, Piscataway, 2018, pp. 120–123.

19. A. Johnsson, G. Schmidt, M. Hauf, P. Pichler, *A review of platinum diffusion in silicon and its application for lifetime engineering in power devices*, *Phys. Status Solidi (A) Appl. Mater. Sci.*, 219 (2), 2022.

20. K. P. Lisiak, A. G. Milnes, *Solid-State Electron.*, 1975, 18, 533.

21. J. Hauber, W. Frank, N. A. Stolwijk, *Defects in Semiconductors 15* (Ed: G. Ferenczi), Vol. 38–41 of Mater. Sci. Forum, Trans Tech Publ, Switzerland, 1989, pp. 707–712.

22. H. Zimmermann, *Ph.D. Thesis*, University of Erlangen-Nuremberg, 1991.

23. H. Zimmermann, H. Ryssel, *J. Electrochem. Soc.*, 1992, 139, 256.

24. H. Zimmermann, H. Ryssel, *Appl. Phys. A*, 1992, 55, 121.

25. W. Lerch, N. A. Stolwijk, H. Mehrer, C. Poisson, *Semicond. Sci. Technol.*, 1995, 10, 1257.

26. M. Jacob, *Ph.D. Thesis*, University of Erlangen-Nuremberg, 1996.

27. E. Badr, P. Pichler, G. Schmidt, *J. Appl. Phys.*, 2014, 116, 133508.

28. F. C. Frank, D. Turnbull, *Phys. Rev.*, 1956, 104, 617.

29. U. Gösele, W. Frank, A. Seeger, *Appl. Phys.*, 1980, 23, 361.

30. T. R. Waite, *J. Chem. Phys.*, 1958, 28, 103.

31. F. Quast, *Ph.D. Thesis*, University of Erlangen-Nuremberg, 2001.

32. P. Pichler, *Intrinsic Point Defects, Impurities and their Diffusion in Silicon*, Springer-Verlag, Wien-New York, 2004.

33. M. D. Giles, *J. Electrochem. Soc.*, 1991, 138, 1160.

34. E. Badr, P. Pichler, G. Schmidt, in *Gettering and Defect Engineering in Semiconductor Technology XVI* (Ed: P. Pichler), Vol. 242 of Solid-State Phenom., Trans Tech Publ, Switzerland, 2016, pp. 258–263.

35. M. Hauf, G. Schmidt, F.-J. Niedernostheide, A. Johnsson, P. Pichler, *2018 22nd Inter. Conf. on Ion Implantation Technology* (Ed: H. R. V. Häublein), IEEE, Piscataway, 2018, pp. 267–270.

36. C. Zechner, N. Zographos, D. Matveev, A. Erlebach, in *Materials Science and Device Issues For Future Technologies* (Eds: L. Pelaz, R. Duffy), Vol. 124–125 of Mater. Sci. Eng., B., Elsevier, Amsterdam, Netherlands, 2005, pp. 401–403.

37. S. T. Dunham, *J. Electrochem. Soc.*, 1995, 142, 2823.

38. P. Pichler, in *2016 Int. Conf. on Simulation of Semiconductor Processes and Devices (SISPAD 2016)* (Eds: E. Bär, J. Lorenz, P. Pichler), IEEE, Piscataway, 2016, pp. 39–42.

39. E. Badr, *Ph.D. Thesis*, University of Erlangen-Nuremberg, 2017.

40. R. Falster, *Appl. Phys. Lett.*, 1985, 46, 737.

41. M. Seibt, A. Döller, V. Kveder, A. Sattler, A. Zozime, *Phys. Status Solidi B*, 2000, 222, 327.

42. P. Pichler, W. Jüngling, S. Selberherr, E. Guerrero, H. W. Pötzl, *IEEE Trans. Comput.-Aided Des.*, 1985, CAD-4, 4, 384, PROMIS.

43. G. Schmidt, J. Bauer, US Patent 2008/0296612 A1, 2008.

44. H. J. Schulze, *Influence of D-defects in FZ material used for power devices and their impact on lifetime and leakage current*, in Proceedings of the Fourth International Symposium on High Purity Silicon, The Electrochemical Society, vol. 96–13, 1996, pp. 289–304.

45. J. R. Taylor, *Classical Mechanics*, University Science Books, US, 2004, ISBN 978-1-891389-22-1.

46. W. Eckstein, *Computer Simulation of Ion-Solid Interactions*, Springer Berlin Heidelberg, Berlin, Heidelberg, 1991, ISBN 978-3-642-73513-4, doi:10.1007/978-3-642-73513-4.

47. K. Oura, V. Lifshits, A. A. Saranin, A. Zotov, M. Katayama, *Surface Science: An Introduction*, Springer Berlin Heidelberg, Berlin, Heidelberg, 2003, ISBN 978-3-662-05179-5, doi:10.1007/978-3-662-05179-5.

48. Caiciss.co.uk, *Kinematic factor derivation*. [Online]. Available: http://www.caiciss.co.uk/kinematic.pdf (visited on Jun. 16, 2020).

49. W. Eckstein, *Computer Simulation of Ion-Solid Interactions*, Springer Berlin Heidelberg, Berlin, Heidelberg, 1991, ISBN 978-3-642-73513-4, doi:10.1007/978-3-642-73513-4.

50. M. J. Deuzeman, "Generation and interactions of energetic tin ions", PhD thesis, University of Groningen, 2019, ISBN 978-94-034-1619-9.

51. J. Lindhard, N. Scharff, H.E. Schiott, "Mat. Phys. Medd. Dan. Vid. Velk 33, 14 (1963)."

52. E. Balanzat, S. Bouffard, *Materials under irradiation*, edited by A. Dunlop, R. Rullier-Albenque, C. Jaouen, C. Templier, J. Davenas, Trans. Tech. Publications, 7-74 (1992).

53. J. Lindhard, V. Nielsen, M. Scharff, P.V. Thomsen, "Mat. Fys. Medd. Dan. Vid. Selsk. 3, 10 (1963)."

54. J. Lindhard, V. Nielsen, M. Scharff, P.V. Thomsen, "Mat. Fys. Medd. Dan. Vid. Selsk. 3, 14 (1963)."

55. G. Dearnaley, J. H. Freeman, R. S. Nelson, J. Stephen, *Ion Implantation*, North-Holland Publishing Company, Amsterdam, 1973.

56. C. Lehman, *Interaction of Radiation with Solids and Elementary Defects Production*, North-Holland, Amsterdam, 1977.

57. Y. Pauleau, *Materials Surface Processing by Directed Energy Techniques*, Elsevier Ltd., UK, 2006.

58. G. Hassan, "Study of silicon thin films implanted with antimony or arsenic", Magister Thesis, University of Constantine 1, 2014.

59. M. Nastasi, J. W. Mayer, *Ion Implantation and Synthesis of Materials*, Springer-Verlag, Berlin, Heidelberg, New York, 2006.

60. J. F. Ziegler, J. P. Biersack, U. Littmark, *The Stopping and Range of Ions in Solids*, Pergamon Press, New York, 1985.

61. J. H. Warner, *Displacement Damage-induced Electrical and Structural Effects in GaAs*, ProQuest Information and Learning Company, USA, 2008.

62. Z. L. Wang, Y. Liu, Z. Zhang, *Handbook of Nano-phase and Nano-structured Materials*, Kluwer Academic/Plenum Publishers, New York, 2003.

63. J. F. Ziegler, *Ion Implantation Science and Technology*, Academic Press, USA, 1984.

64. J. F. Ziegler, J. M. Manoyan, "Nucl. Inst. and Meth. B35 (1988) 215."

65. H. M. Urbassek, *Handbook of Surface Science*, Vol. 3, North-Holland, 2008, p. 881.

66. B. Window, N. Savvides, "Charged particle fluxes from planar magnetron sputtering sources", *Journal of Vacuum Science & Technology A*, 4, 196 (1986).

67. P. Sigmund, *Stopping of Heavy Ions: A Theoretical Approach*, Springer Tracts in Modern Physics, Vol. 204, Springer, Berlin, 2004.

68. P. Sigmund, *Particle Penetration and Radiation Effects: General Aspects and Stopping of Swift Point Charges*, Springer Series in Solid-State Sciences, Vol. 151, Springer, Berlin, 2006.

69. N. Bohr, "Phil. Mag., 25 (1913) 10."

70. H. Bethe, "Ann. Phys. (Leipzig) 5 (1930) 324."

71. F. Bloch, "Ann. Phys. (Leipzig) 16 (1933) 285."

72. H. H. Andersen, J. F. Ziegler, *Hydrogen Stopping Power and Ranges in All Elements*, Vol. 3, Pergamon Press, New York, 1977.

73. W. H. Bragg, R. Kleeman, "Phil. Mag. 10 (1905) 318."

74. J. Lindhard, M. Scharff, "K. Dan. Vidensk. Selsk. Mat. Fys. Medd. 33 (1953) No. 15."

75. P. Sigmund, K. B. Winterbon, "Nucl. Instr. and Meth. 119 (1974) 541."

76. A. D. Marwick, P. Sigmund, "Nucl. Instr. and Meth. 126 (1975) 317."

77. W. R. Grove, "Philos. Mag. 5, 203 (1853)."

78. E. Goldstein, "Verh. Dtsch. Phys. Ges., 4, 228, 237 (1902)."

79. "Doctoral thesis, Ion-Surface Interaction: Simulation of Plasma-Wall Interaction (ITER), 2013."

80. Y. Yamamura, H. Tawara, "At. Data. Nucl. Data Tab., 62, 149 (1996)."

81. G. Falcone, "Surf. Sci., 187, 212 (1987)."

82. F. Gullo, "Phys. Lett. A125, 432 (1987)."

83. J. P. Biersack, W. Eckstein, "Appl. Phys. A 34, 73 (1984)."

84. Y. Yamamura, Y. Kitazoe, "Rad. Eff. 39, 251 (1978)."

85. Sigmund 1969.

86. P. Sigmund, "Stopping of Heavy Ions", in *Topics in Applied Physics,* edited by R. Behrisch, Springer Berlin, Vol. 47, p. 9 (1981).

87. D. A. Thompson, "Radiation Effects", 56(3-4):105–150, (1981).

88. R. Kelly, "Surf. Sci., 90, 280 (1979)."

89. K. L. Merkle, W. Jager, "Phil. Mag. A 44, 741 (1981)."

90. R. C. Birtcher, S. E. Donnelly, "Phys. Rev. Lett. 77, 4374 (1996)."

91. S. E. Donnelly, R. C. Birtcher, "Heavy ion cratering of gold", *Phys. Rev. B* 56, 13599 (1997).

92. T. J. Colla, R. Aderjan, R. Kissel, H. M. Urbassek, "Sputtering of Au (111) induced by 16-keV Au cluster bombardment: Spikes, craters, late emission, and fluctuations", *Phys. Rev. B* 62, 8487 (2000).

93. E. M. Bringa, K. Nordlund, J. Keinonen, "Phys. Rev. B 64, 235426 (2001), 210, 211."

94. E. M. Bringa, R. E. Johnson, R. Papaleo, "Phys. Rev. B 65, 094113 (2002), 211."

95. E. M. Bringa, E. Hall, R. E. Johnson, R. Papaleo, "Nucl. Instrum. Methods B 193, 734 (2002), 211."

96. K. Nordlund, K. O. E. Henriksson, J. Keinonen, "Appl. Phys. Lett. 79, 3624 (2001), 211."

97. L. A. Larson, J. M. Williams, M. I. Current, "Reviews of Accelerator Science and Technology, pp. 11-40 (2012)."

98. Mihai Bogdan Lazar, "Étude du dopage par implantation ionique", Thèse de doctorat, 2002.

99. Rivière J.P., Structure and properties of hard coatings produced by dynamic ion mixing, Journal de physique IV 10 (P6) (2000) 53-58.

100. F. Haranger, "Doctoral thesis", 2003.

101. S. Gouasmia, "Cluster-Matter Interaction", Doctoral thesis, 2022

102. N. Bohr, Mat.-Fys. Medd. Kgl. Dan. Vid. Selsk. **18** (1948) 8.

103. R.F. Sippel, E.D. Glover, 1960, Nucl. Instrum. Methods, 9, pp. 37–48.
104. T.B. Pierce, P.F. Peck, W.M. Henry, 1965, Analyst, 90, pp. 339–345.
105. T.B. Pierce, P.F. Peck, D.R.A. Cuff, 1965, Anal. Chim. Acta, 39, pp. 433–436.
106. G. Deconninck, 1972, J. Radioanal. Chem., 12, pp. 157–169.
107. R.B. Boulton, G.T. Ewan, 1977, Anal. Chem., 49, pp. 1297–1304.
108. B. Borderie, J.N. Barrandon, 1978, Nucl. Instrum. Methods, 156, pp. 483–492.
109. R. Curtis Bird, J.S. Williams, Ion Beam for Material Analysis, 1990.
110. G. Deconninck, 1978, Introduction to Radioanalytical Physics, Akademia Kiado, Budapest.
111. N. Karmaker & al, GSC Advanced Research and Reviews, 2021, 07(01), 064–072 M.
112. Natasi, et al., Ion Beam Materials Analysis: Fundamentals and Applications, CRC Press, Boca Raton, FL, 2015.
113. F. Watt et al., Principles and Applications of High-Energy Ion Microbeams, Adam Hilger, Bristol, 1987.
114. K. Krane, Introductory Nuclear Physics, John Wiley & Sons, USA, 1988.
115. Sven A.E. Johansson, John L. Campbell, Klas G. Malmqvist, Particle-Induced X-ray Emission Spectrometry, Vol. 133, Wiley Interscience, 1995.
116. J.L. Campbell, K.G. Malmqvist, S.A.E. Johansson, Particle Induced X-ray Emission Spectrometry (PIXE), John Wiley & Sons, New York, 1995.
117. P. Zhang, X. Wang, J. Liu, Y. Huang, G. Li, Y. Sha, "Analysis of candidate microreference materials of lichen and algae by SRXRF and PIXE," Nuclear Instruments and Methods in Physics Research B, Vol. 189, pp. 107–112, 2002.
118. L. Beck, P. Moretto, "Emission X induite par particules chargées (PIXE): applications," Techniques de l'ingénieur, p. 2558, 2004.
119. M.C. Blaich, A. Denker, "PIXE analysis of Middle Age objects using 68 MeV protons," Nuclear Instruments and Methods in Physics Research B, Vol. 189, pp. 315–319, 2002.
120. C.G. Ryan, and D.R. Cousens, GeoPIXE: PIXE Microanalysis Software System, Users Guide, 1992.
121. J.A. Maxwell, J.L. Campbell, and W.J. Teesdale, The Guelph Software Package. Nucl. Instr. Meth. B **43.** 218-,1989.
122. S.A.E. Johansson,. and J.L. Campbell, PIXE: A Novel Technique for Elemental Analysis. Wiley, 1988.
123. E. Rutherford, 1911, Phil. Mag., 21, 669.

124. W.K. Chu, J.W. Mayer, M.A. Nicolet, Backscattering Spectrometry, Academic Press, 1978.
125. M.R. Nakles, Experimental and Modeling Studies of Low Energy Ion Sputtering for Ion Thrusters, Master's Thesis, Virginia Polytechnic Institute, July 2004.
126. P. Jalkanen, Properties of SiGe Alloys Studied by Ion Beam and Suppression of Al Film Superconductivity by Implantation, Ph.D. Thesis, University of Jyvaskyla, March 9, 2007.
127. J.W. Martin, J. Yuan, S.A. Hoedi, B.W. Filippone, D. Fong, T.M. Ito, E. Lin, B. Tipton, A.R. Yang, "Phys. Rev. C", 68, 055503, 2003.
128. M. Dobeli, Cas. web. cem. ch / cas / pruhonice / PDF / Doebli. pdf.
129. M. Mayer, 2003, Users. ictp. it / ~ pub – off / lectures / inso2z / Mayer – 1.
130. J.R. Tesmer, M. Nastasi (Eds.), Handbook of Modern Ion Beam Materials Analysis, Materials Research Society, Pittsburgh, 1995.
131. Huan-sheng Cheng, Hao Shen, Fujia Yang, Jiayong Tang, "Cross sections for non-Rutherford backscattering of 4He from five light elements," Nucl. Instr. and Meth. B, Vol. 85, pp. 47–50, 1994.
132. Ghislain Boudreault, Doctoral Thesis, 2002.
133. W. Eckstein, M. Mayer, "Rutherford Backscattering from Layered Structures Beyond the Single Scattering Model," Nucl. Instr. and Meth. B, Vol. 153, pp. 337–344, 1999.
134. M. Mayer, SIMNRA Users Guide, Technical Report IPP 9/113, Max-Planck-Institut für Plasmaphysik, Garching, Germany, 1997.
135. D.J. O'Connor, T. Chunyu, "Application of heavy ions to high depth resolution RBS," Nucl. Instr. and Meth. B, Vol. 36, pp. 178–188, 1989.
136. L.C. Feldman, J.W. Mayer, Fundamentals of Surface and Thin Film Analysis, North-Holland, New York, 1986.
137. V. Shutthanandan, A.A. Saleh, R.J. Smith, "Surf. Sci.", Vol. 450, pp. 204, 2000.
138. Vaithiyalingam Shutthanandan et al., "Physical Review Special Topics – Accelerators and Beams", 15, 063501, 2012.
139. Víctor Alarcón Díez, Doctoral Thesis, 2016.
140. J.L. Colaux, C. Jeynes, High accuracy traceable Rutherford backscattering spectrometry of ion implanted samples, Anal. Methods 6 (1) (2014) 120–129,
141. B. Rout, R. Greco, N. Pastore, A. D. Dymnikov, and G. A. Glass, Upgrading a Duoplasmatron ion source to produce high brightness beam for nuclear microprobe

applications with a tandem accelerator, Nucl. Instr. and Meth. B , vol. 241, no. 1–4, pp. 382–386, 2005.

142. M. Moser *et al.*, “Transport of a high brightness proton beam through the Munich tandem accelerator, Nucl. Instr. and Meth. B , vol. 348, pp. 34–42, 2015.